Stormonth-Darling, John Moir (2013) *Fabrication of difficult nanostructures by injection moulding.* PhD thesis.

http://theses.gla.ac.uk/4456/

Fabrication of difficult nanostructures by injection moulding

By
John Moir Stormonth-Darling

Submitted in fulfilment of the requirements for the degree of Doctor of Philosophy.

July 2013.

School of Engineering

College of Science and Engineering

University of Glasgow

Abstract

There is an increasing demand for nanostructured polymeric surfaces for many scientific and commercial applications including the fields of cell and tissue engineering, where the study of the ways that cells interact with their environment holds great potential for the future of regenerative medicine. Current replication based fabrication techniques, such as hot embossing, which are used to produce nanostructured surfaces for this type of research are not fast enough to keep up with the growing demand for them. Injection moulding offers a high throughput alternative to these processes and can upscale the production of nanopatterned samples by several orders of magnitude. However, the nickel moulds traditionally used to injection mould micro- and nanostructures are limited to producing recessed features due to the rate at which the injected polymer cools upon contact with it. In order to replicate raised features (e.g. pillars) the polymer needs enough time to fill the nanoscale cavities of the mould before freezing.

A solution to this limitation of nickel tooling is devised and implemented, using a thermally insulating tooling material that facilitates the formation of nanopillars by injection moulding. This tooling material can be patterned by a range of fabrication techniques including photolithography and nanoimprint lithography. The tooling can be used to replicate nanopatterns over underlying micron and millimetre scale topographies. This flexible solution enables the large volume production of samples containing raised poly(carbonate) nanopillars without significantly compromising cycle time.

Following this, the technique is adapted in an attempt to replicate high aspect ratio nanostructures. In this section a range of non-adhesive surface coatings are tested for their abilities to enhance the replication process through the systematic analysis of their durability and the replication fidelity that they enable. Nanopillars with aspect ratios of greater than 10:1 are successfully produced and are used to fabricate surfaces for cell engineering research. This success is also demonstrative of the technique's potential to mass produce nanostructures for other applications such as non-reflective and dry adhesive surfaces.

Finally, a study is undertaken to replicate microstructures with an elastomeric polymer. The tooling solution is used to assess the minimum feature size that can be replicated with this polymer and how processing parameters and non-adhesive coatings can improve this.

This thesis documents the development of a range of enabling techniques which add to the existing toolbox of nanofabrication technologies. They address a growing demand for nanostructured polymeric surfaces in cell and tissue engineering research, whilst remaining open and adaptable to any application that requires the high throughput production of nanopatterned polymeric samples.

Table of contents

List of figures

List of tables

Publications arising from this thesis

Paul Michael Reynolds, Rasmus Haugstrup Pedersen, <u>John Moir Stormonth-Darling</u>, Matthew Dalby, Mathis O Riehle, Nikolaj Gadegaard, Label free segmentation of co-cultured cells on a nanotopographical gradient, Nano Letters 13 (2), Dec 2012.

<u>John M. Stormonth-Darling</u> and Nikolaj Gadegaard, Injection Moulding Difficult Nanopatterns with Hybrid Polymer Inlays, Macromolecular Materials and Engineering 297 (11), Nov 2012.

+ two more in preparation resulting from the work described in chapters 4 and 5 of this thesis.

Conference presentations arising from this thesis

<u>J.M. Stormonth-Darling</u> and N. Gadegaard, *Production of remarkably high aspect ratio nanostructures by injection moulding*, (oral presentation) 10th International Workshop on High Aspect Ratio Micro and Nano System Technology, Berlin, April 2013.

<u>J.M. Stormonth-Darling</u> and N. Gadegaard, *Using coated hybrid tooling to reproduce nanostructures with 10:1 aspect ratio by injection moulding*, (oral presentation) 38th International Conference in Micro and Nano Engineering, Toulouse, September 2012.

<u>J.M. Stormonth-Darling</u> and N. Gadegaard (presenter in my absence), *Hybrid inlays for injection moulding*, 37th International Conference in Micro and Nano Engineering, Berlin 2011.

Acknowledgement

Author's declaration

I declare that all the work presented in this thesis has been carried out by me unless otherwise acknowledged or referred to.

John Moir Stormonth-Darling

July 2013

Chapter 1 Introduction

1.1 Nanostructured surfaces

The small scale structure of surfaces has long been known to dictate properties independent to those of the bulk material. In ancient times metals and precious stones would be polished to make them shine just as they are today, albeit with more sophisticated methods an applications beyond the cosmetic.[1] Many different animal and plant species have evolved specialised surfaces to improve their chances of survival such as the non-reflective eyes of moths[2] and the dry adhesive footpads of some reptiles.[3] The interiors of all multicellular organisms contain surface motifs and mechanical cues across length scales from the molecular to that of whole tissues,[4] which have a vast range of consequences that researchers are only beginning to understand.[5] In recent years our ability to manipulate and understand the microscopic physical characteristics of surfaces has transformed our daily lives and continues to drive us through the new demands born of this understanding and the inquisitive spirit which gave rise it in the first place.

The need for nanostructured surfaces is vast and varied, from the individual layers of integrated circuits to cutting edge research into the manipulation of light at the photonic level.[6] This section introduces some of the applications of nanostructured surfaces that were motivational to the work conducted in this project.

1.1.1 Biomimetic nanostructures

The work in thesis is particularly inspired by nanostructures found or used in biological systems. The compound eyes of many insects such as moths and butterflies exhibit nanoscale surface structures that interact with incident light such that they both decrease the amount reflected and increase how much is absorbed.[2] As well as making them harder for predators to see, this adaptation improves the moth's vision and offers inspiration for the designers of devices such as solar panels,[7, 8] smart windows[9] and other optical applications where the maximisation of light absorption is advantageous or a non-reflective surface is required.[10, 11] These functionalities are provided by a subwavelength nanostructure, such as those shown in Figure 1.1, which cannot be resolved by light at wavelengths longer than twice than the feature size or periodicity. The functional principal of the nanostructure is a gradual transition of refractive index making it difficult for light to escape.[12]
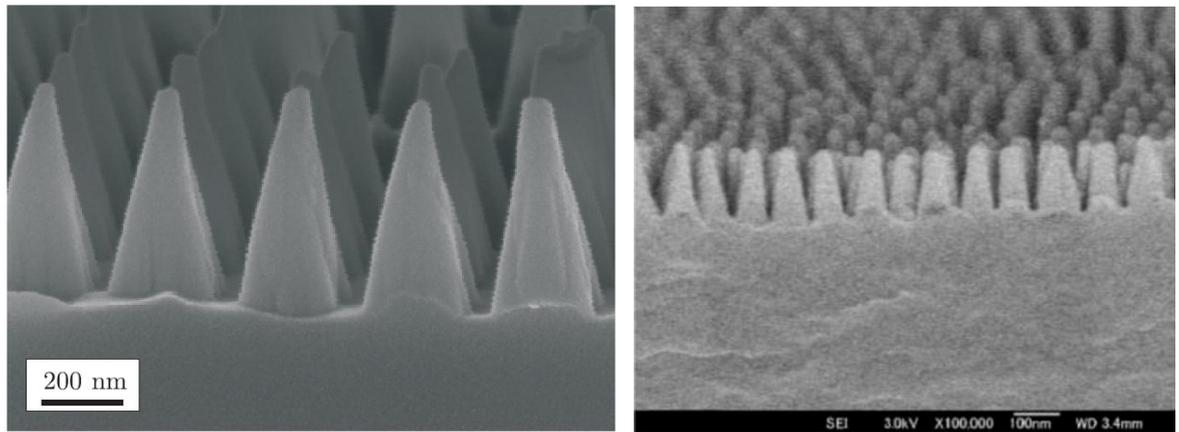
Figure 1.1 - SEM images of examples of synthetic anti-reflective moth eye structures made of quartz (left)[11] and acrylic resin(right).[8] Images taken from references as indicated.

An adaptation common to many plant species (perhaps most famously the Lotus – see Figure 1.2) involves the presence of water repellent micro- and nanostructures on the surfaces of their leaves which cause water droplets to roll of and pick up dirt along the way in a system of effortless self-cleaning.[13, 14] Similar structures also lend hydrophobic properties to the wings of flying insects and the legs of water-walking insects.[15]
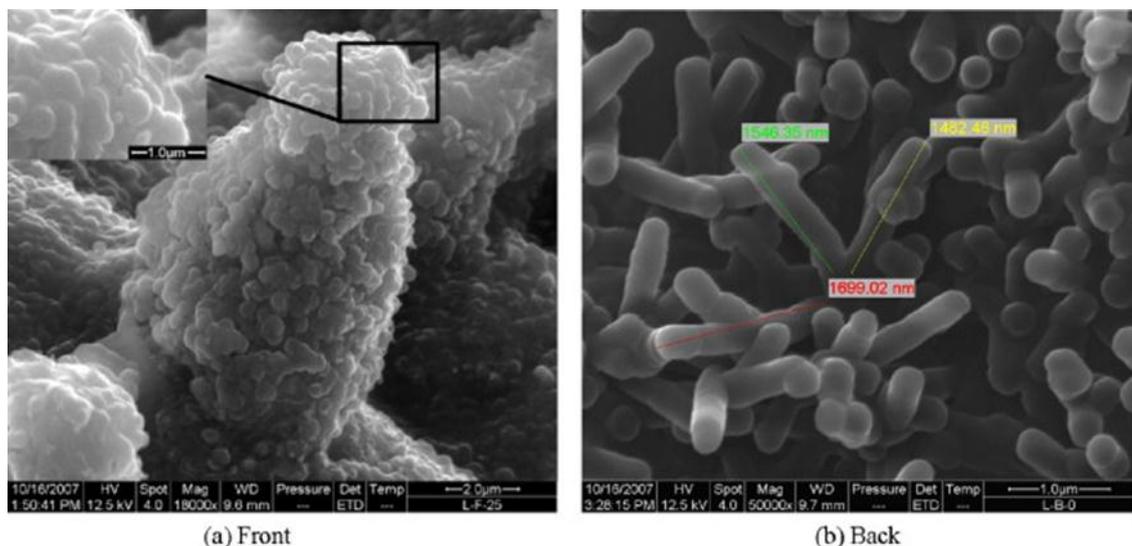
Figure 1.2 - SEM images showing micro- and nanoscale surface structure of a lotus leaf. Image taken from reference [14].

This hydrophobic nature is a well understood phenomenon which can be characterised by the angle formed between a water droplet and the surface (detailed in methods, Chapter 2, section 2.5.4). In the Cassie-Baxter (heterogeneous) wetting state[16] a surface exhibits increasingly hydrophobic properties, and increasing contact angle, as its physical contact area with a water droplet decreases as a result of the surface's micro- and nanotopography. This superhydrophobicity may also be concomitant with non-adhesive properties such as those seen on the skin of sharks (Figure 1.3)

which not only repel water to reduce drag, but also exhibit anti fouling properties which prevent the build-up of potentially harmful microbial species.[17, 18]

(a) A real shark skin   **(b) PDMS negative replica**   **(c) Shark-skin replica**
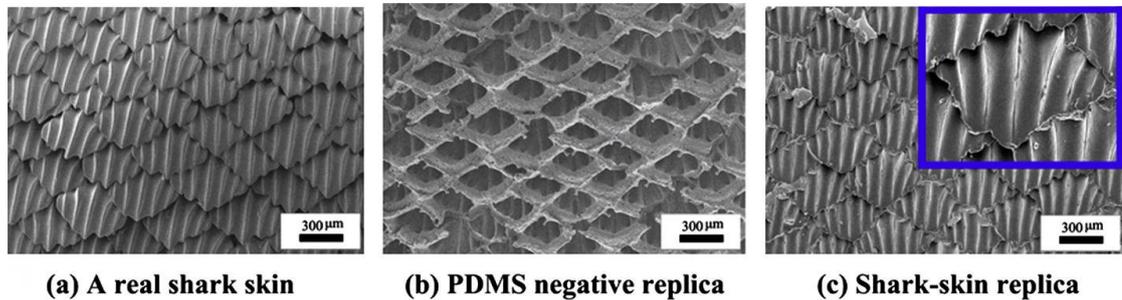
Figure 1.3 - SEM images of shark skin and synthetic replica. Image taken from reference [18].

In contrast to the hydrophobic leaf, nanostructures can also have adhesion promoting properties. By exploiting capillary forces and van der Waals interactions through their complicated hierarchically micro/nanostructured toe pads, gecko lizards make easy work of ascending almost any surface and can even traverse ceilings without fear of becoming unstuck and falling to the ground.[3] Due to the complexity and inherit difficulty associated with making these structures and their huge scope for useful applications, the production of synthetic gecko foot technology (Figure 1.4) is still an active research area in both commercial and academic circles. [19, 20]
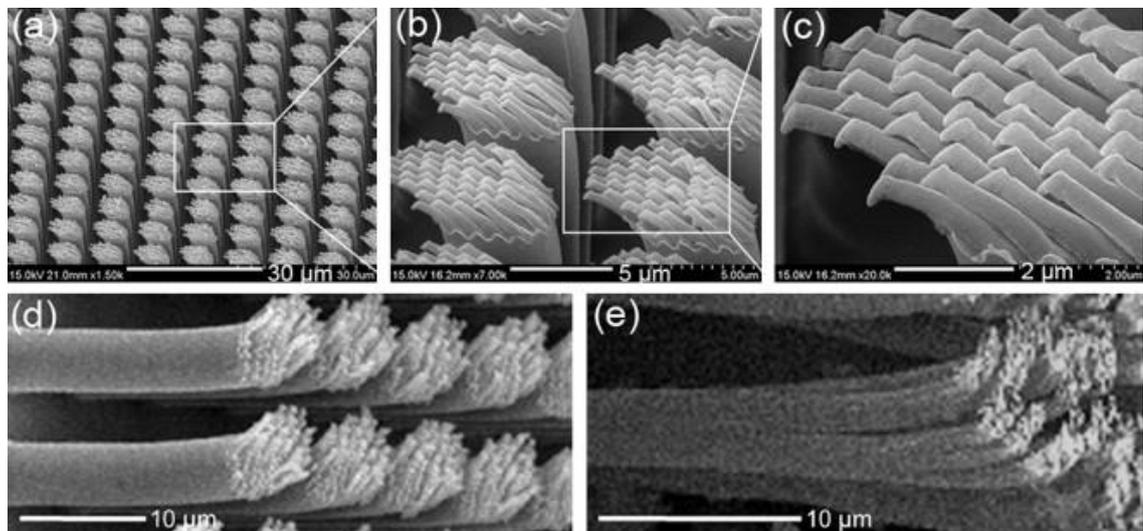
Figure 1.4 - SEM images of gecko foot inspired synthetic dry adhesive structures (a-d) and real gecko foot hairs (e). Image taken from reference [20].

1.1.2 Cell and tissue engineering

As well as the biomimetic research areas mentioned above, there exists an area of bioinspired surface design focused on the micro- and nanoscale environment of living cells. In a living organism every cell is constantly exposed to chemical and physical stimuli from its neighbouring cells and the extra-cellular matrix (ECM), a three-dimensional environment with a locally distinct physicality.[4] Traditional *in vitro* practice sees cells exposed to an environment very far removed from their natural *in vivo* landscape, especially physically. However, since it was first shown that physical interactions between cells and their substrates play an important role in many aspects of their behaviour,[21, 22] much work has been done to simulate the nature of this environment in both two and three dimensions,[23] and advances in nanofabrication and imaging technology have allowed researchers to explore it at an ever diminishing physical scale and increasing level of complexity.[24, 25] In addition to traditional biological interactions involving molecular signalling between cells and molecules present in the ECM, a range of physical factors have been shown to directly affect the behaviour of cells including: stiffness/elasticity,[26, 27] mechanical interactions,[28, 29] and micro- [30, 31] and nano- [32, 33] scale topography (Figure 1.5).[34, 35] Exploration of the ways these topographical cues direct cell behaviour forms the foundation of new healthcare technologies and treatments, particularly in the field of regenerative medicine, where, for example, the nanotopographical stimulation of mesenchymal stem cells to differentiate into bone forming tissue could improve the longevity of bone implants[36] and synthetic scaffolds can be constructed to aid in the repair of specific tissues and organs.[37]
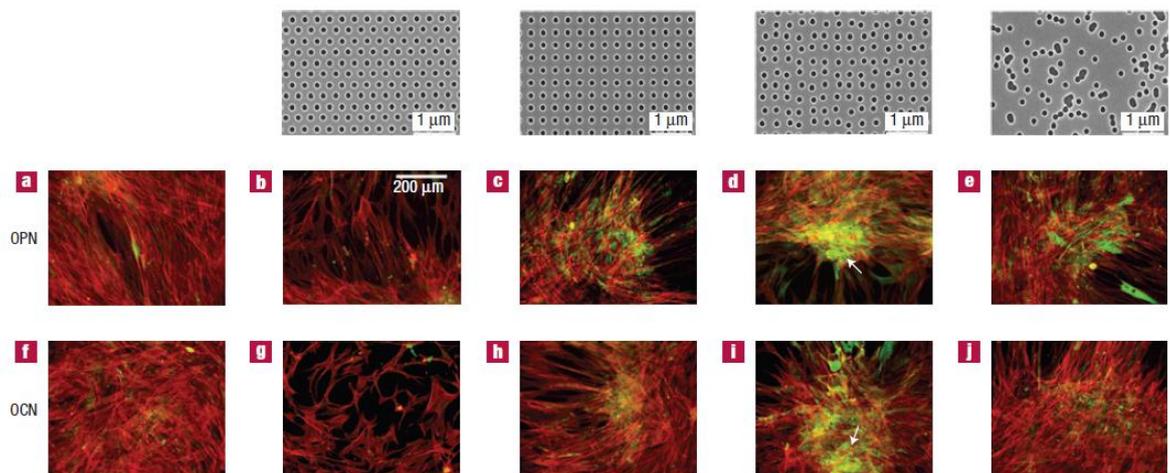
Figure 1.5 - Nanotopographically induced commitment of human osteoprogenitor cells to a bone-forming lineage. The green stain indicates the presence of bone forming cells whcih is maximised in (d) and (i) by the corresponding nanopattern. Bone nodule formation is indicated by arrows. Image taken from reference [36].

The role of engineers in this field is to supply biologists with the micro- and nanostructured surfaces they need to conduct this work which may often require the development of novel

fabrication techniques and use of materials not commonly seen in the sphere of micro- and nanofabrication.[38-40]

ventual outcomes cell and tissue engineering research will often require complex three dimensional devices, but fundamental laboratory research into cell-substrate interactions still takes place primarily in tissue culture dishes using flat substrates. Tissue culture labware is almost exclusively made from polystyrene (PS), an amorphous thermoplastic widely used to mass produce all kinds of plastic objects at low cost by techniques such as extrusion and injection moulding. Key to the preference for PS is its transparency, required for microscopy, and the fact that it is biocompatible, something that cannot be said for all polymers which may leach into or be degraded by the liquid media in which cells reside. In contrast to this, the experimental substrates have historically and continue to been made from a great range of materials including metals,[41] cast polymers,[42] thermoplastic polymers,[36] and hydrogels.[43] The range of material reflects the many types of interaction under scrutiny (i.e. mechanical stiffness or nanotopography), the potential applications (i.e. titanium implants)[44] as well as the type of structures desired and the continually evolving micro- and nanofabrication techniques that can realise them.

1.2 Fabricating nanostructured surfaces

1.2.1 Direct nanopatterning techniques

Exposure to almost any external environment will elicit changes in a material's surface properties, such as the native oxide which forms on the surfaces of many metals in the presence of air, and a great many techniques directly affect change in a surface's micro- and nanoscale structure. The uptake and extent to which different direct patterning techniques are used varies according to the physical size of dimensions required, quantity of production, equipment setup, operational and material costs and the nature of the final application. This is illustrated by the choice between electron beam lithography (EBL) or photolithography which is influenced heavily by setup costs and production scale. EBL is a serial process which can directly write nanometre scale patterns on to a receptive surface and is widely used in small scale production applications like research and prototyping. As a serial process the pattern is written on a continuous pixel by pixel basis across a sample, as opposed to a parallel process where the patterning occurs across the whole sample in the same moment. Photolithography (or optical lithography) is a parallel process that can achieve similar patterning, but is limited to micrometre length scales using equipment within the budget of most research institutions. In an industrial mass production setting however, time taken to pattern submicron structures by a serial process like EBL makes the process uneconomical and, as a result, the electronics industry has invested huge amounts of money into reducing the resolution limit of optical lithography in order to take advantage of the higher throughput offered by the parallel

nature of the process. These investments have allowed the industry to keep up with market demand, but the equipment required is far beyond the investment capabilities of all but the biggest commercial organisations.

On the level of a research institution, lithographic techniques such as EBL, ion beam lithography photolithography and laser lithography are ubiquitous, but require specialised equipment which may be beyond the budgets of some. If the intention is to apply a nanostructure to a surface without the need to specifically control each individual feature then a number of techniques exist that may negate the need for such specialised tools as those used in lithography. For example, the overall roughness of a surface may be a sufficient measure of nanostructure for the purposes some cell-substrate research,[45, 46] a parameter that can be altered by relatively simple techniques such as polishing or blasting with small particles. A cheaper alternative which provides a way of producing nanostructures of a particular size that is also not reliant upon specialised lithography tools is colloidal lithography.[47] Colloidal particles can be made to self-assemble in a predictable pattern on surfaces where they can act as a mask for metal deposition and/or etching to create a uniform nanopattern.[48, 49] With this type of technique it is possible to define a nanopattern of regularly sized features with a known density, but without the exquisite levels of order and control that only the likes of electron or ion beam lithography can deliver. Both photolithography and EBL were used in this project and are discussed in more detail in Chapter 2.

1.2.2 Replication based nanopatterning techniques

Direct nanopatterning of surfaces allows unique structures to be defined in methodical, step by step manner that delivers fantastically high quality results that cannot be obtained by any other means, but is generally unsuitable for mass production or requires massive financial investment to make it suitable as is the case with optical lithography in the microelectronics industry. A more economical route to creating large numbers of nanostructured devices lies in replication based technology where a single master may give birth to many clones of itself, eliminating the need to repeat an entire fabrication process. These methods are gaining increasing interest from industry where the resolution limit of optical lithography is making it harder to form the ever smaller structures that are desired.[50]

A large group of replication based techniques fall under the banner of nanoimprint lithography[51, 52] (NIL) which, in the case of thermal NIL (T-NIL), is similar to hot embossing although they differ somewhat on a practical and conceptual level, with the former as a lithography (pattern transfer for further processing) technique and the latter as a method of direct patterning. These processes are parallel by their nature and differ from lithographic processes in that the pattern transfer is mediated by a physical deformation rather than a purely chemical change requiring subsequent development. NIL was first developed by Chou *et al.* in 1995[53] and was quite remarkable in that from the outset it demonstrated successful replication of 25 nm structures, a

figure that was only limited by the patterns on the stamp. More recently feature sizes as low as 2 nm have been reported.[54] In a typical NIL process a master stamp, previously fabricated by other methods such as photolithography and etching, is brought into contact with the polymer which has been heated to above its glass transition temperature (T_g) (this is the case for amorphous polymers, crystalline polymers are characterised by their melting temperature). As pressure is applied, the polymer flows and adopts the physical form imposed by the stamp and after sufficient time the assembly may be cooled and separated, leaving the inverse pattern of the stamp embedded in the polymeric material. This embossed structure may be used as a functional component of further fabrication steps (e.g. as an etch mask) or may itself form a structural component of the final outcome. Several variations of NIL have been developed including UV-NIL in which the embossed material is photosensitive and cured by UV radiation whilst in contact with the stamp, with or without simultaneous heating depending on the material's properties. Specific NIL techniques used in this project are discussed in more detail in Chapter 2.

Other replication techniques that operate on a moulding basis include thermoforming and polymer casting. The former is a thermoplastic processing technique that is used in industrial high throughput manufacturing above the microscale and is capable of producing micro- and nanostructures over larger curved surfaces by patterning a thin film before heating and pulling it over a larger structure.[55, 56] Casting polymers, such as PDMS, are not thermoplastics and take their form in a curing process which can take several hours. It has somewhat customisable elastic properties and is a ubiquitous protoyping material for microstructured devices owing to its intrinsic ease of processing and finds particularly frequent use in the field of microfluidics.[57] In addition to these, soft lithography also deserves a mention, despite it being a family of techniques concerned with patterning *on* the surface rather than *in* it. Microcontact printing is a popular soft lithographic technique where a patterned solid stamp is coated in the printing material before being pressed against another sample to which the material, in the shape of the pattern, is transferred. It has found a great deal of use in patterning functional surfaces for studying cell-substrate interactions.[58, 59]

Replication based fabrication techniques are advantageous their simplicity, low cost and speed compared to direct patterning processes and that fact that they can be applied to many different materials makes them a highly applicable to patterning the large range of materials of interest to biologists in cell and tissue engineering research involving cell-substrate interactions.[60] Despite being faster than direct patterning, simple embossing with thermoplastic polymers is still slow enough (5 - 20 minutes cycle time) to limit the rate at which biology experiments can be conducted. The general variability inherent to the results of most biology experiments requires that multiple repetitions be conducted. To produce sufficient substrates for these by a simple embossing process is a long and laborious task which can consume many working hours which could otherwise be spent elsewhere if a higher throughput replication method was available.

One technique which has been developed to tackle the throughput issues of NIL is roll-to-roll (R2R) embossing. In a R2R system the polymer to be imprinted takes the form of a thin film wrapped around a barrel which, as it is unravelled, will pass beneath a patterned roller where the pattern is transferred simultaneously with any necessary heating or UV curing. The film may be coated in an imprintable material or be the subject of imprinting itself. There are countless variations of R2R systems, as well as similar techniques such as sheet-to-sheet and roll-to-plate.[61] These have demonstrated a great deal of success in the patterning of thin polymer films for emerging applications including lab-on-chip,[62] flexible electronics[63] and those requiring large area patterning such as solar photovoltaics.[64] The physical setup of R2R lends itself to a production line style installation analogous to newspaper printing where further process steps such as metal deposition might be incorporated into a continuous process chain.

Step-and-repeat and step-and-flash NIL (SR-NIL and SF-NIL) offers another alternative to increase the throughput of NIL requiring a somewhat less elaborate setup than R2R techniques. These processes use an automated imprint head to perform one imprint after another and, in the case of SF-NIL, uses a transparent stamp which allows the imprinted area to be illuminated with UV light to cure the resist before moving on to the next imprint location. In the case of imprinting a continuous pattern over an area larger than the stamp, the difficulty lies in minimising the distance between successive imprints to a level deemed acceptable for the application. These processes are, in theory, capable of producing replicas with the same quality as conventional thermal and UV-NIL. They have demonstrated the ability to pattern curved surfaces[65] and replace the role of photolithography in the fabrication of multilayer electronic components on thin films.[66]

Step and repeat imprinting is a good way to upscale a simple NIL process with relative ease, while R2R and other roller based processes are the most effective methods yet developed to pattern large areas and thin films with extremely high throughput. However, neither of these techniques offer the high throughput production levels of nanopatterned bulk parts (i.e. not thin film) readily attainable by the process of injection moulding.

1.3 Fabrication by injection moulding

1.3.1 Background

Injection moulding technology revolutionised manufacturing in the 2nd half of the 20th century by making it possible to replicate rapidly identical parts made from thermoplastic materials from a single machined mould. While the cost of the initial infrastructure, equipment and a precisely constructed mould might be very high, once production is up and running the economies of scale make mass production by injection moulding a solid foundation for an extremely efficient business

model. The technology is still widely used today and looks set to dominate industrial production for many years to come.

Injection moulding was put to good use by the music industry in the 1980s with the advent of compact discs, a form of media storage that required cheap, accurate replication of microscale features on a previously unseen scale More recently, Blu-Ray Discs have seen commercial injection moulding move to length scales below 150 nm.[67] It is, therefore, an industrially proven method of nanofabrication, but has yet to be widely utilised as such outwith the sphere of optical media. This is despite the fact that researchers have demonstrated successful replication of distinct structures as small as 50[68], 25[69] and 5 nm.[70] With so many other applications of polymeric nanostructures such as non-reflective, superhydrophobic and adhesive surfaces as well as substrates for biological research into regenerative medicine, there is great scope for injection moulding to play a much wider role in realising low cost mass production for these technologies.

1.3.2 The injection moulding process

During the injection moulding process, a thermoplastic polymer is heated to around 100°C above its glass transition temperature (T_g) before it is injected into the mould cavity which is kept 30-50°C below the polymer's T_g. Here the polymer rapidly cools and the moulded part is ejected before the process begins again to produce the next part in a fully automated and unsupervised process. It is this separation of heating and cooling cooling that makes injection moulding such a high throughput process compared to embossing where these processes occur in the same location; the industrial production of a single CD takes only around 4 s to complete.

More details of the practical side of the injection moulding process are discussed in the methods section of this thesis (Chapter 2), while the remainder of this chapter, aside from a brief introduction to some injection moulding terminology, comprises a review of the literature in the field of injection moulding micro- and nanostructures.

1.3.3 Tooling

The central component of an injection moulding machine is the mould, or tool. It is here where the mould cavity resides and where the part is formed. Mould tools used for the production of most plastic products, be they coat hangers or tooth brushes, are generally made by milling large pieces of steel and assembling them together into a single unit containing the cavities, vents and other specific features required for the production of a particular part or parts. The practice of tool making is a precise art where accuracies of tens of micrometres can be required as well as the capacity to fit in as part of an elaborate, multi stage, automated mass production process. If the intended product of a tool is to contain micro- or nanoscale features on its surface, certain adaptations must be made to the tool design as these length scales cannot be addressed by metalworking techniques.

The accepted way to nanopattern a single surface of a moulded part (invented to facilitate the production of optical media) is to use an inlay-frame configuration as shown in Figure 1.6 (and Figure 2.5).
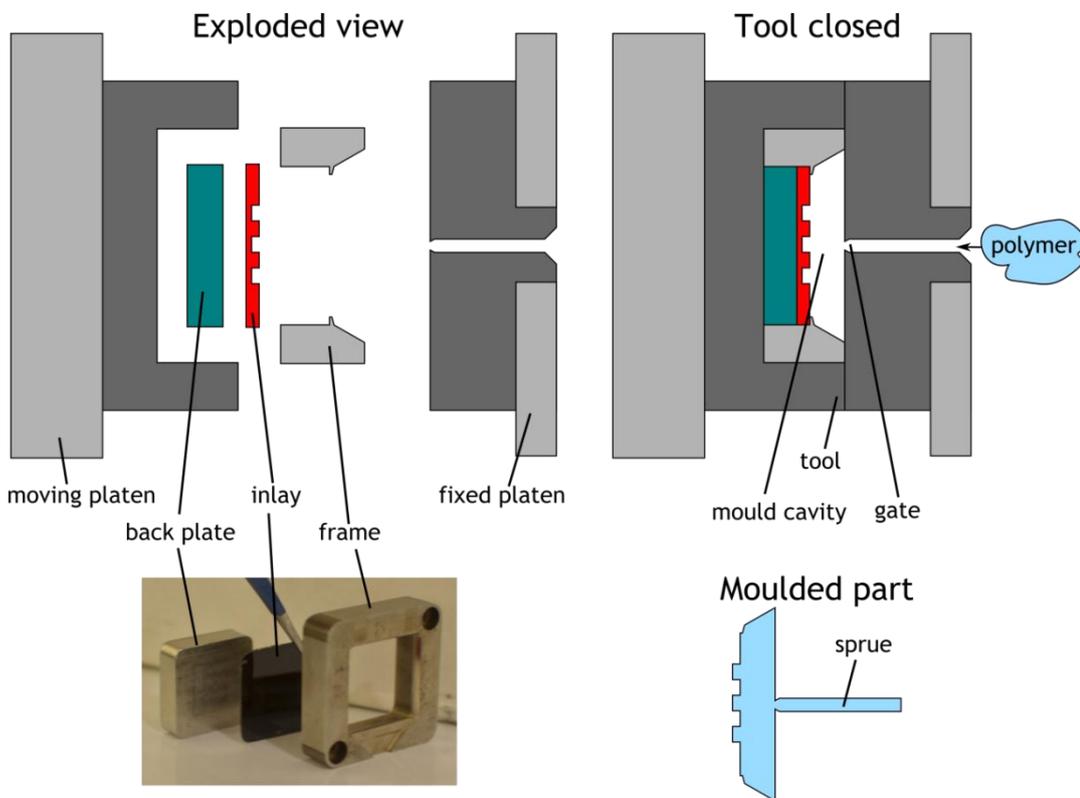
Figure 1.6 - Schematic diagram and corresponding photograph of an inlay-frame tool design.

In this configuration the inlay (sometimes referred to as an *insert* in the literature) is a planar substrate which has been patterned in advance by other means. The tool is designed such that the inlay slots into a frame which, in turn, slots into the bulk of the tool, allowing parts of one particular size and shape (or *format*) to be produced with the pattern from the inlay formed on one of its surfaces. The term *tooling* is used to refer to the material(s) of which the inlay is comprised or indeed the inlay itself.

1.3.4 Tooling material

The fabrication of micro- or nanopatterned inlays generally requires a wafer based approach as would be employed to fabricate structures of this size for any purpose, although milling processes are an option for larger structures.[71] For this reason, the likes of silicon, quartz and III-V materials might seem like an obvious choice with which to fabricate inlays and they have indeed been used to conduct research in the field[68, 72] although the brittle nature of these materials may cause them to shatter under the high pressures of the injection moulding process depending on the specifications of specific equipment and processing parameters.[73] Because of this, nickel, with its durable characteristics, has become a standard tooling material for the injection moulding of micro- and nanostructures.[71] Nickel tooling is commonly formed by a LIGA(in German:

lithographie, galvanik und abformung meaning lithography, electroplating and moulding)-like process whereby it is galvanically electroplated against a prefabricated master pattern. The electroplating step is a carefully controlled electrolysis process where patterned target of nickel deposition is the cathode.

As described earlier, the molten polymer is injected into the tool which has its temperature kept below the polymer's T_g. As the hot melt makes contact with the tool wall it quickly cools and a skin layer is formed.[74] The formation of the skin layer largely inhibits the ability to produce raised structures (e.g. pillars) at diminishing length scales and increasing aspect ratios. A the polymer melt moves into the patterned holes of the inlay, the surrounding metal conducts the heat away so quickly that the polymer cools below T_g and freezes before it has been able to completely fill the hole. This does not adversely affect the replication of holes like those which pattern optical media, but it does make it difficult, if not impossible, to replicate structures which stand proud of the surface which are often desirable for the type of biomimetic and cell engineering applications mentioned earlier. An example with titanium tooling highlights another possible artefact of this problem in which polycarbonate (PC) broke off inside the inlay's 50 nm holes, causing the replication of 50 nm holes rather than the intended pillars in subsequent shots.[68] Nonetheless, this example did show Ti to be robust and damage free after 50 shots while the robustness of Ni is surely evidenced by its widespread use in the commercial replication of optical media.

One type of method which had been developed to combat the premature cooling of injected polymer is known as variothermal injection moulding. Variothermal techniques use elaborate mechanisms that will require the incorporation of plumbing or electrical systems into the construction of the tool, with these additions being used to heat and cool the tooling surface at the appropriate times in order to aid the filling of micro and nanostructures.[75, 76] Variothermal heating with a MEMS heater located behind nickel tooling has been shown to improve the filling of 320nm wide grooves with PC from 20 nm to 60 nm, but was still short of the 82 nm groove depth[77, 78] and laser mediated heating (capable of temperature gradients of 300K/s) was successfully used to fabricate superhydrophobic microstructures in polypropylene (PP) with steel tooling.[79] These structures were conical pillars with a base diameter of around 5 µm and were not replicated to a high level of uniformity. Yet other ways to implement variothermal injection moulding include heating the tooling surface by electrical induction[80] which has been shown to enhance the filling of nanostructures in nickel tooling,[81] or by electrifying the actual inlay surface[82] which permitted the formation of nanoscale hair-like structures over a 2 minute cycle time. Furthermore, a variothermal process may use steam and coolant to respectively heat and cool the tool and has been used to successfully replicate a 46 inch LCD panel although the heating and cooling added well over a minute to the cycle time.[83, 84]

In an infrared based variothermal approach nanochannel filling was further aided by the introduction of a heat resistant polymer layer behind the Ni inlay to further impede the heat transfer to the surrounding tool.[85] This use of heat retardant material offers a simpler approach to variothermal techniques which has been adopted by a number of researchers. Over several publications [86-89] Yoon, Barry *et al.* document their successes with silicon and hybrid metal-polymer inlays for injection moulding of microscale features. They have shown that inlays made from an unspecified polymer coated with aluminium or titanium allowed injected PS to fill 1-2 μm trenches (depth dimensions are unclear, but do not appear to be more than the width) to twice the depth of fluorinated silicon tooling,[89] (work which went on to form the basis of a patent application).[90] They also showed that embossed polycarbonate (PC) inlays, somewhat unsurprisingly, suffered deformation during injection moulding with the same polymer, but that polyimide (PI) coated with aluminium was capable of replicating microstructures in PC and PMMA for over 1000 cycles.[87] Polymer-metal tooling has shown similar durability in the form of photolithographically patterned SU-8 microstructures on Ni which showed no sign of damage after 300 replicas with cyclic olefin copolymer (COC)[91] although heat retardation was not required in this case. Embossed polymer tooling has other reported successes at the microscale in the form of UV-cured poly(urethane acrylate) (PUA), with additional insulation provided by poly(ethylene terephthalate) (PET), replicating gratings of 1-10 μm in width and 10 μm in height.[92] At the nanoscale, an embossed polyvinyl alcohol (PVA) film, produced features down to 100 nm in size in COC, but required that the adhesive inlay be sacrificially dissolved after each replication, somewhat cancelling out the core advantage of injection moulding as a high throughput technique.[93] An example of a non polymeric heat retardant material, bulk metallic glass, also shows promise as a robust tooling solution that can facilitate the formation of 100-200 nm bumps in PMMA.[94]

It is clear that there exist two main schools of thought for how best to tackle the problem of premature freezing induced poor mould filling: variothermal and heat retardation. Variothermal techniques offer a means of precise control that could lead to more predictable outcomes, but do not seem to be any more advantageous in that regard in the evidence presented by the current literature. Furthermore, the development of complex heating/cooling systems is time consuming and costly, and with the exception of the laser heating[79] and induction[80, 81] examples these solutions caused significant increases in cycle time. The polymeric tooling approach is appealing, not just for its simplicity, but also for the fact that it opens up a wealth of alternative inlay material and patterning options (e.g. UV-NIL) that remove the requirement for expensive Ni electroforming and can be adapted to the individual's own fabrication capabilities. With the simple approach the imagination is free to ponder the nature of the next pattern rather than concentrate on the seemingly unnecessary technicalities of developing a sophisticated variothermal solution.

1.3.5 Surface coatings

A common feature in replication based micro- and nanofabrication is the use of non-adhesive surface coatings to aid both the filling of moulds and the subsequent demoulding of the replica.[95-97] This section discusses some of those reported in the literature and provides a summary of these in Table 1.1.

In a NIL process they can greatly improve results through the reduction of surface energies and resulting interfacial friction which occurs at the critical moment when the master and replica are separated.[98] These forces, which are amplified at higher aspect ratios, can lead to the structural failure of features on both the master and moulded or imprinted product.[99] Fluorosilanes are a popular choice when it comes to anti-stiction coatings as they will readily form a thin monolayer on a chemically activated surface that greatly reduces surface energy.[52, 100, 101] The affinity of fluorosilanes for silica has led to silicon, glass/quartz and other surfaced oxidized materials (such as NiO and TiO[95] and some specially formulated PIs)[102] being widely used as imprint masters[103] and have also been used successfully to improve the release properties of SU-8 moulds.[104] It has also been shown that the introduction of nitrides to fluorocarbons can enhance the durability of non-adhesive coatings.[105]

Measurements of water contact angles (WCAs) on surfaces can be an indicator of surface energy and therefore replication performance. A high WCA indicates a low energy which will decrease the potentially damaging forces experienced during separation and a low angle implies a strong wetting ability which is beneficial to the initial filling of structures. This implies that a good replication surface will display a happy medium between these two extremes that will depend on physical conditions such as the pattern geometry, viscosity of the replication material and available.[106]

The success of injection moulding of micro- and nanoscale features relies as much on smooth demoulding as in a nanoimprint process. Yoon *et al.* demonstrated that fluorinated silicon tooling was not only protected from the damaging effects of interfacial friction, but also made it possible to almost completely fill 4 µm wide 9.2 µm deep trenches with thermoplastic polyurethane (TPU) where uncoated tooling could not even fill half.[107] These type of coatings have even made it possible to fight the filling problems associated with Ni tooling and permit the replication of 40 nm diameter pillars in COC.[108] Fluorosilane treatment of Ni has also helped to reduce the build-up of injected PC and poly(4-methyl-1-pentene) (PMP) residue for over 15 000 machine cycles in an experiment where molybdenum nitride and tungsten nitride coatings also performed favourably in this regard.[109] Elsewhere, chromium and titanium nitrides have shown benefits in terms of tool durability,[110] while one broad UV NIL study of five metal nitrides and seven metal oxides saw no single coating performing better than another, suggesting that the most effective release at the

demoulding stage must be determined by the specific master-replica material combination rather than by a single mould coating which outperforms all others in all situations.[111]

In cases of purely metallic coatings, aluminium and titanium coatings on polymeric tooling have been shown to double the filling of microstructures with PS compared to fluorinated silicon with a heat insulating back plate.[89, 90] Aluminium did however show slight peeling on imprinted PI tooling after 1000 cycles with PS and PC.[87] Gold coated nickel was reported to be resistant to residue when PMMA was moulded up against it,[86] although Ni, as the traditional tooling of choice, is itself not prone to residue build-up or it would unlikely have achieved such status.

It is abundantly clear that non-adhesive surface coatings are a vital addition to any replication based fabrication process, and while fluorosilanes appear to offer a solution in most situations, they may require some optimisation of their composition[96] or prove inferior to metals in some cases.[89] There is probably no one-coating-fits-all solution, but indicative techniques such as water contact angle analysis can guide the way to design and interpret the practical development of potential tooling solutions.

Surface coating	Stamp / tooling material	Method	Replica material	Performance
Fluorosilanes (FS)	Si / SiO$_2$	T-NIL / UV-NIL / embossing.	Various thermoplastics and curing polymers	Widely regarded as effective non-adhesive coating in replication based fabrication.[52, 100, 101]
(NiO,TiO)+FS	Ni	NIL	PMMA	Not as effective as SiO$_2$+FS.[95]
FS	SU-8	NIL	PMMA, PDMS	High quality replication of multilayer microstructures [104]
FS	PI	T-NIL / UV-NIL / embossing.	Thermoplastic and UV curing polymers.	Faithful replication on 4 inch wafer.[102]
Nitrided fluorocarbon	SiO$_2$	NIL	PMMA	Enhanced durability over non nitrided fluorocarbons.[105]
FS	Si	Injection moulding (IM)	TPU	Protected tooling and enhanced filling of micropillars.[107]
FS	Ni	IM	COC	Made it possible to fill sub 100 nm pillars.[108]
FS, MoN, WN	Ni	IM	PC, PMP	Prevented polymer build-up over 1500 cycles.[109]
CrN, TiN	Steel	IM	Polyamide with glass fibre	Lower wear to tooling than with traditional methods (heat treatment, Cr deposition, nitriding).[110]
Al,Ti	polymer	IM	PS, PC	Improved PS filling of microstructures over polymerbackplate+SiO$_2$+F.[89, 90] Al peeling after 1000 cycles.[87]
Au	Ni	IM	PMMA	Resistant to residue.[86]

Table 1.1 - Summary of non-adhesive coatings used in NIL/embossing processes and injection moulding.

1.4 Summary

1.4.1 Aims of this thesis and contribution to the field

This chapter has introduced several applications of nanostructured surfaces. These included non-reflective surfaces, superhydrophobic surfaces, dry adhesive surfaces, anti-fouling surfaces and surfaces for exploring the interaction of living cells with their physical environment. All of these applications can be realised by replication based fabrication methods such as hot embossing, NIL, polymer casting, thermoforming, roll-to-roll and roll-to-plate techniques and injection moulding. It has been put forward that injection moulding offers the greatest potential of these in terms of high throughput mass production and is on par with the best in terms of replication fidelity. It is also well established as an industrial fabrication technique, offering the potential for a relatively easy transition from research to commercialisation, and is proven to be capable of producing nanostructured surfaces in the form of optical media. Admittedly, the quantity of literature-based evidence for injection moulding is far less substantial than other replication based nanofabrication techniques, especially compared to embossing and NIL, but this itself presents the opportunity to make a significant contribution to the field through any knowledge gained in the development of processes to fabricate nanostructures by injection moulding.

The specific aims of this thesis are as follows:

- Develop enabling fabrication techniques to augment the existing selection of nanofabrication processes available for the nanopatterning of thermoplastic polymers. Achieve this through reliable, consistent and repeatable fabrication processes, using standard nanofabrication materials and equipment (such as those found in the JWNC) wherever possible.

- Utilise injection moulding as a means to apply these enabling techniques to the high throughput mass replication of high quality nanopatterned samples.

- Implement a solution to the problem of incomplete mould filling of raised nanostructures (i.e. pillars). This must be integrated with our injection moulding equipment with as few modifications as possible; therefore a heat retardation method (rather than a variothermal method) would be preferable.

- Develop methods which are versatile, adaptable and applicable to as many applications as possible. Potential adaptations may include the size, shape and aspect ratio of nanostructures, the materials used and different tool configurations. It is not feasible to

address directly any and all potential applications, but a short list to keep in mind would be: non-reflective surfaces, non-wetting surfaces, dry adhesive surfaces and, in particular, nanostructured surfaces for cell-substrate interactions. The potential to expand this to nanopatterned implantable materials would also be beneficial.

- Fabricate surfaces to be used by biologists tailored to their needs as closely as possible. This requires that samples be as flat as possible for ease of microscopy, be of a suitable shape and size to fit into standard labware and be constructed from biocompatible materials.

- Attempt to fabricate demonstrators of non-reflective, non-wetting and dry adhesive surfaces.

- Quantify results at all stages of process development to enable analysis and refinement of techniques.

- Document the successes and failures in the pursuit of these aims. Any knowledge gained should be recorded to add to the limited literature on the subject. Process details should be fully and accurately recorded to enable the work to be built upon in future.

1.4.2 Structure of the thesis

The next chapter details the relevant materials, methods and background theory that are relevant to the project. Following that are three chapters which document the development of techniques that are pertinent to the primary aims in cell engineering applications and form a solid foundation to enable the realisation of the others. The first focusses on the limitations of injection moulding as a means to replicate pillared nanostructures with the second building on this to pursue the realisation of high aspect ratio nanopillars and systematically study how a range of tooling surface coatings might enhance the technique. The third further utilises these new methods to assess the capabilities of an elastomeric polymer in terms of the minimum feature size it can be used to replicate, and provides a means to up-scale the production of a micron scale pattern used to study the mechanical behaviour of cells. The final chapter is devoted to the drawing of conclusions on the success of the work and the future outlook for the techniques developed therein.

Chapter 2 Methods

2.1 Overview

This project is concerned with the fabrication of nanostructures by injection moulding which are widely considered difficult or impossible to produce by this method. In order to produce such structures by injection moulding a new tooling solution had to be developed. The new tooling was manifested in the form of inlays, small interchangeable samples that can be inserted into the tool of the injection moulding machine, which themselves were made using a variety of fabrication processes which had to be developed and refined. This chapter provides practical and technical details of the injection moulding process and the methods used to fabricate inlays, as well as the techniques used to characterise the results. A more concise summary of a process to produce nanopatterned parts by injection moulding is provided in the appendix at the end of this thesis. Structurally, this chapter works backwards by first discussing injection moulding followed by inlay fabrication and then the methods used to create the precursors to those, before finally describing sample characterisation. All processes were carried out by me unless otherwise stated and all fabrication and characterisation was conducted in the James Watt Nanofabrication Centre (JWNC) except injection moulding which I conducted in the mechanical workshop in the School of Engineering.

2.2 Injection moulding

2.2.1 Thermoplastic polymers

Thermoplastics are a class of polymer that are characterised by their reversible temperature dependant physical characteristics; they may be melted and frozen repeatedly without chemical alteration of their constituent molecular chains. This behaviour is in contrast to thermosetting plastics and other curable materials which form cross links between their molecular chains when energy is applied by, for example, heat or UV radiation. Thermoplastics can be classified as amorphous (random molecular structure) or semi-crystaline (molecules are ordered in a crystalline manner) polymers, or thermoplastic elastomers (rubbery, elastic polymers with interesting properties discussed in Chapter 5).

Above its glass transition temperature (T_g) an amorphous thermoplastic will move from its solid state to a more malleable one, increasing in malleability until it reaches its melting temperature (T_m) when it behaves as a liquid. This easily controlled phase change and the fact that they retain their original characteristics upon refreezing have seen thermoplastic polymers be used in the manufacture of countless products and devices where they are formed into a functional shape by a mould based process such as thermoforming or injection moulding.

In this project a number of thermoplastic polymers were used in processes to replicate micro- and nanostructures by injection moulding. These were: poly(carbonate) (PC), poly(propylene) (PP), poly(styrene) (PS), poly(methyl methacrylate) (PMMA) and thermoplastic poly(urethane) (TPU).

2.2.2 The injection moulding machine

Figure 2.1 - The Engel Victory 28 injection moulder

The machine used was an Engel Victory 28 fully hydraulic injection moulder (pictured in Figure 2.1), typical in specification to what would be used in industry to create similar sized parts to those made in this work. Given that the very essence of injection moulding is founded in efficiency in an industrial production setting, it was central to the validity of this work that the techniques developed be in line with these values. This is why such an industry standard machine was chosen. The moulder's key specification parameters are summarised in Table 2.1.

Maximum injection pressure	2200 bar
Maximum clamping force	280 kN
Screw diameter	18 mm
Maximum barrel temperature	450°C
Maximum tool temperature	200°C
Minimum tool temperature	~ 15°C (water cooled)
Maximum shot volume	20 cm^3

Table 2.1 - Engel Victory 28 specification summary
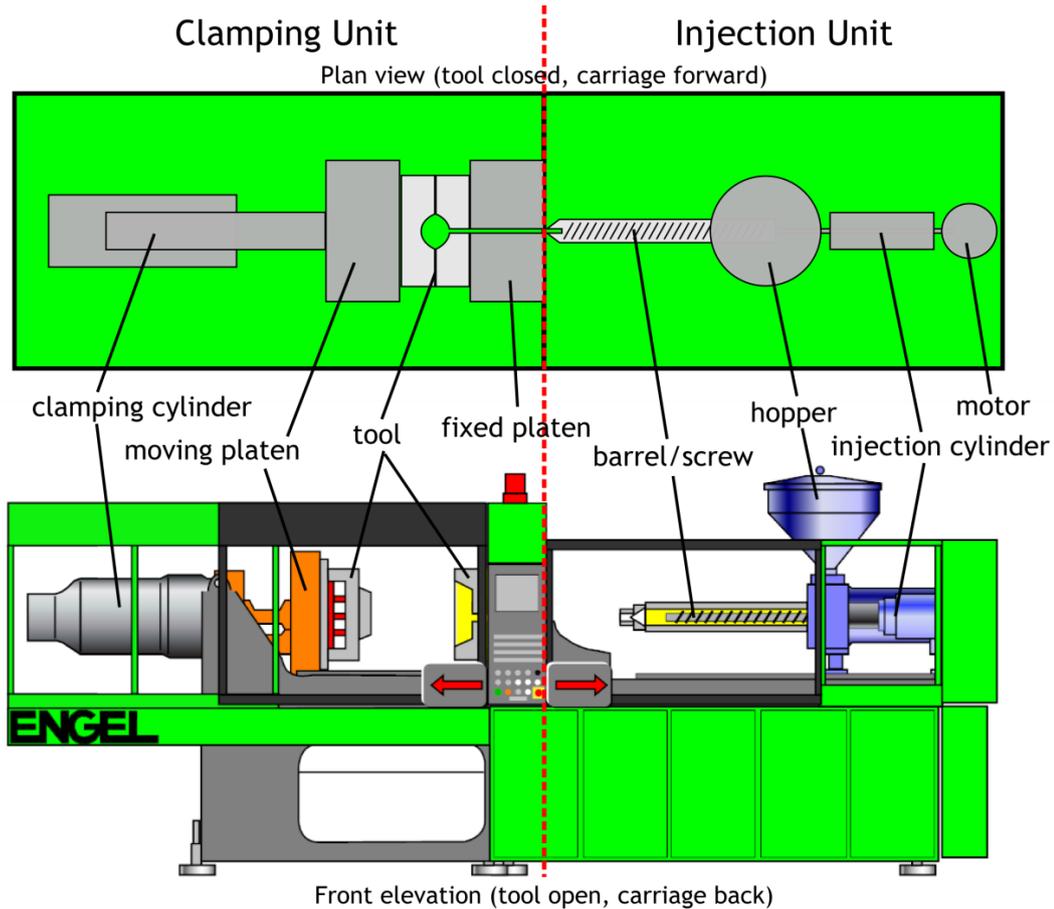
Figure 2.2 - Layout of Engel Victory 28 injection moulding machine - plan view and front elevation (screen grab from Engel VirtMold virtual machine software).

Figure 2.2 shows a schematic layout of the injection moulding machine as viewed from above and a corresponding illustration of it as viewed from the front. An injection moulding machine is made up of two distinct units: the injection unit and the clamping unit. The polymer that will eventually be moulded starts its journey in the hopper located to the right of the injection unit in the form of small beads measuring a few millimetres across which are gravity fed through the throat into one end of the screw. The screw is heated by four elements which increase in temperature progressively from right to left (see Figure 2.3) and terminates at the nozzle where the temperature is set to the value defined as the melt temperature (T_m) in the processing conditions. The cylindrical barrel which houses the screw and the threads of the screw itself has constant diameter along its length, but the central shaft of the screw increases in diameter as it approaches the nozzle, thereby decreasing the gap through which the polymer moves. This combination of increasing temperature, rotational motion and narrowing gap serves to gradually melt, pressurise and mix the polymer to ensure that by the time it reaches the end it is homogeneous in both its temperature and consistency.
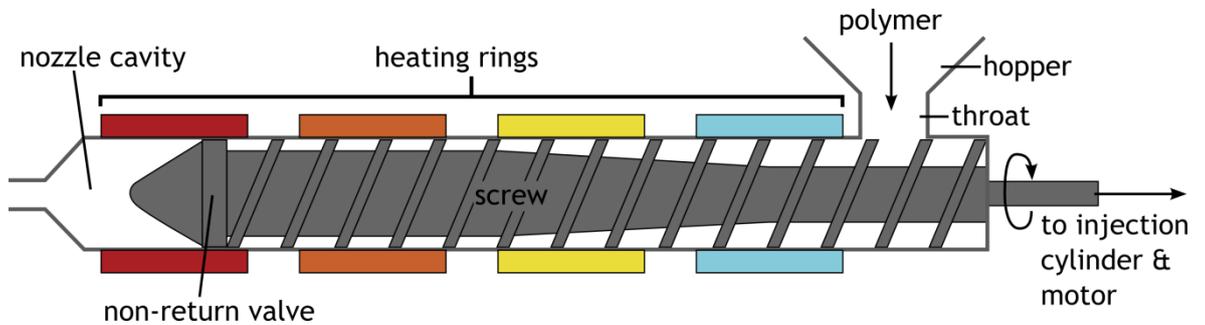
Figure 2.3 - The barrel.

Located at the nozzle is a non-return valve (see Figure 2.4) which moves back under the pressure of the polymer as it fills the nozzle cavity, having been pushed through the narrow gaps by the turning screw in a process known as *plasticising*. When the cavity is full the check ring blocks the progress of any more polymer, the plasticising stops and the next shot is ready for injection. It is important to note that the presence of a previous injection's completed part is required to block the nozzle and allow the polymer for the next shot to build up; without this the polymer is free to flow out of the end of the nozzle when plasticising is active. The thrust for the injection itself is supplied by the injection cylinder at the far end of the screw.
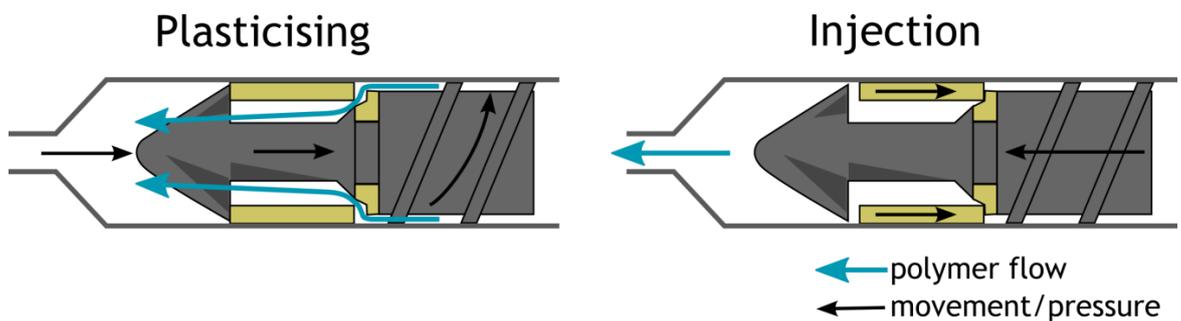
Figure 2.4 - Operation of the non-return valve.

The clamping unit houses the all important mould, a cavity located at the centre of the tool (see Figure 2.5). The tool comprises two halves, the moving platen and the fixed platen, which allows it be closed while the polymer is injected before reopening so that the final moulded part can be ejected. The size and shape of the mould cavity define those of the moulded part. Examples of parts produced during this project are depicted at the bottom of Figure 2.5. They are flat, square parts with dimensions 24 x 24 x 2 mm with a fan gate attached to a ~4 cm sprue which can be broken off at a weak point where the gate meets the sprue. A single face of the part can be patterned by inserting a patterned inlay into a frame in the mould as illustrated in Figure 2.5.
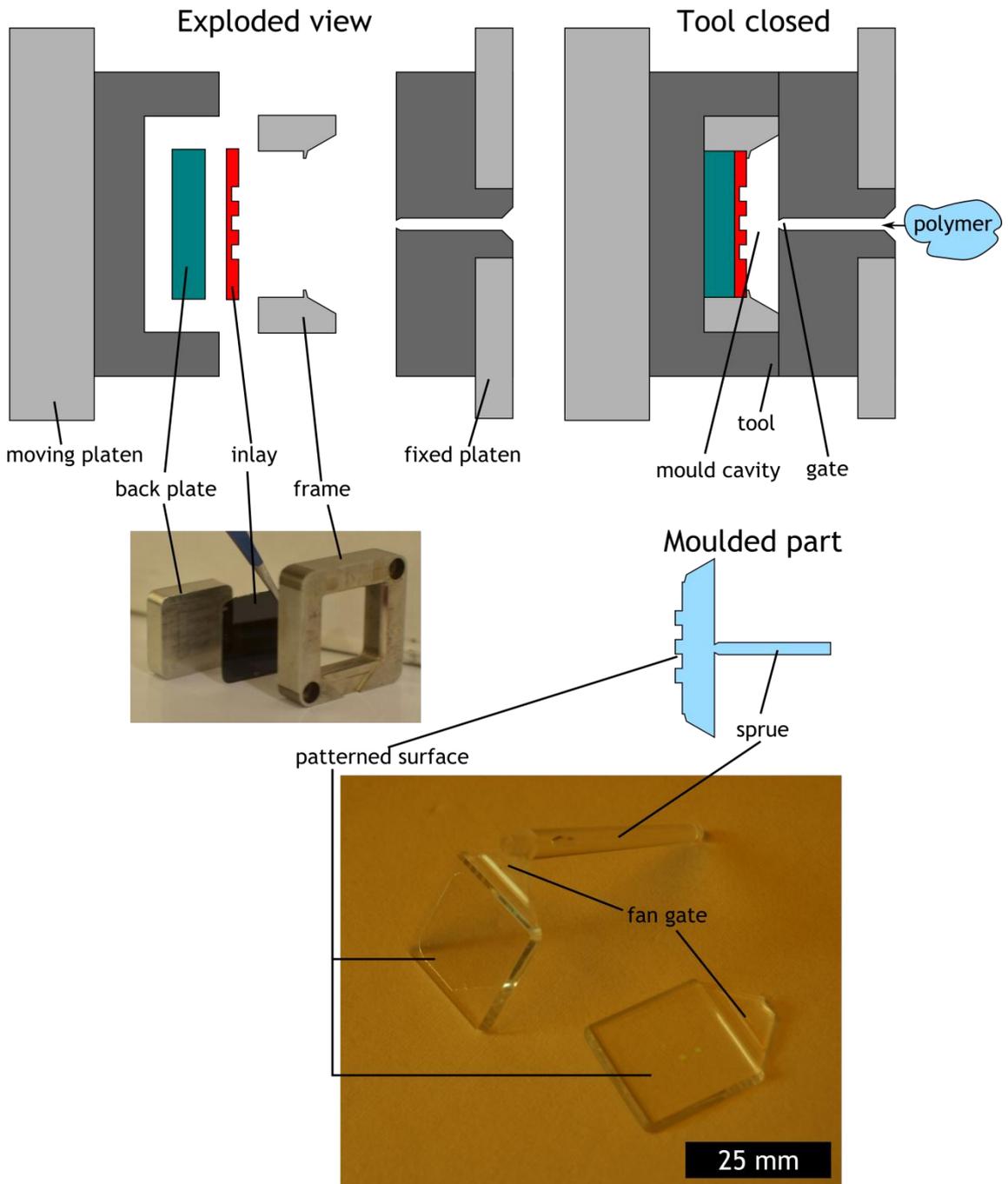
Figure 2.5 – Assembly of tool, frame and inlay and polycarbonate parts produced with the Engel Victory 28 injection moulding machine.

2.2.3 The injection moulding process

A typical moulding session will last for a few hours with a warm-up and post moulding purge specific to the polymer in use. Table 2.2 summarises various preparation and purging conditions for polymers used in this project and Table 2.3 summarises their typical processing conditions.

Polymer	Brand (manufacturer)	Drying temperature (ºC)	Drying time (hours)	Priming material (temp (ºC))	Purging material (temp (ºC))
Poly(carbonate) (PC)	Makrolon OD 2015	110	2	PC (250)	PP (250-240)
Poly(propylene) (PP)	Capilene 125	No drying	No drying	PP (230)	Not required
PP (purging grade)	Capilene E50E	No drying	No drying	N/A	N/A
Poly(styrene) (PS)	Total 1810	No drying	No drying	PS (220)	PMMA (240), PP (240)
Thermoplastic poly(urethane) (TPU)	Estane X1393-041 (Lubrizol)	60-70	3	PS (250)	PS (210-240), PMMA (240), PP (240)
TPU	Tecoflex EG80A (Lubrizol)	60-70	3	PS (250)	PS (210-240), PMMA (240), PP (240)

Table 2.2 - Preparation and purging conditions for polymers used in this project.

Polymer (brand)	Melt temp (nozzle) (ºC)	Tool temp (ºC)	Injection speed (cm^3s^{-1})	Holding pressure (bar)	Cooling time (s)	Shrinkage (%)
PC (Makrolon OD 2015)	280	80	50	1000	5	0.6
PP (Capilene 125)	230	40	50	1000	5	1.0-2.5
PS (Total)	260	60	30	1000	5	0.4-0.7
TPU (Estane X1393-041)	190	20 (water cooled)	Minimum (0.9)	100	80	0.5
TPU (Tecoflex EG80A)	190	20 (water cooled)	Minimum (0.9)	80	60	0.8-1.2

Table 2.3 - Typical processing conditions and shrinkage values for polymers used in this project.

A typical injection moulding session lasts for several hours and the precise details depend on the processing requirements of the polymer in use. The process for poly(carbonate) (PC) injection moulding proceeds as follows:

- Collect the required volume of polymer beads and dry in vacuum oven at 110°C for 2 hours.

- Turn on injection moulding machine and cooling unit, allowing 30-60 minutes for the hydraulics to warm up.

- Load the appropriate program in the injection moulding machine's software which will recall all necessary parameters including melt/mould temperature, injection speed, cooling time, holding pressure etc.

- The PC recipe will set tool temperature to 80°C and melt to 280°C (the screw contains four heating elements set to progressively warmer temperatures along its length – in the case of PC they will be set to 250°C, 260°C, 270°C and 280°C from hopper end to nozzle end).

- Before it rises too high set melt temperature to 250°C and purge the system by pouring about 750 g of un-dried PC into the hopper and plasticising it through the screw.

- Set melt temperature back to 280°C for processing.

- Insert mould inlay and set mould height in software.

- Pour dried PC into hopper and plasticise until melt runs clear.

- Wipe nozzle, close mould, advance injection unit until hydraulic pressure build-up is achieved.

- Activate automatic plasticising which will stop when the mould is filled. This also fills the nozzle cavity with polymer ready for the first proper shot.

- Open mould and eject part. This part will not be fully formed and may be discarded.

- Switch to semi-automatic mode and run several cycles one-by-one until happy with smooth operation and general part quality – adjust parameters as necessary and repeat.

- Switch to automatic mode and run continually. Continue to assess part quality until acceptable consistency is evident.

- Set required number of parts and run automatically until this number is reached.

- At the end of the run retract the injection unit and purge the remaining PC from the screw by automatic plasticising.

- Turn off tool heating, remove inlay and leave tool close, but not under pressure.

- Reduce melt temperature to 260-240°C.

- Pour ~750 g of purge-grade PP into hopper and plasticise through until empty.

- Turn off melt heating and hydraulics. Turn off injection moulding machine and cooling unit.

The timeline of a single cycle is illustrated in Figure 2.6 and described in the following bullet points:

- mould closing – the two halves of the mould come together under pressure.

- carriage unit forward – pressure is built up at the end of the screw.

- injection – the polymer is pushed into the mould at high speed.

- holding pressure – the mould is held under pressure so that as the polymer shrinks due to cooling, more may be forced into the mould to ensure a full filling.

- cooling time and plasticising for next cycle – time delay to allow polymer to freeze; the next shot of polymer is prepared by plasticising with the newly injected part blocking the nozzle, thus allowing the plasticised material to build up.

- carriage unit back – screw pressure relaxed.

- mould opening – mould opens with moulded part stuck to inlay side of mould.

- ejection of part – ejector pins pop out and part falls into collection bucket.
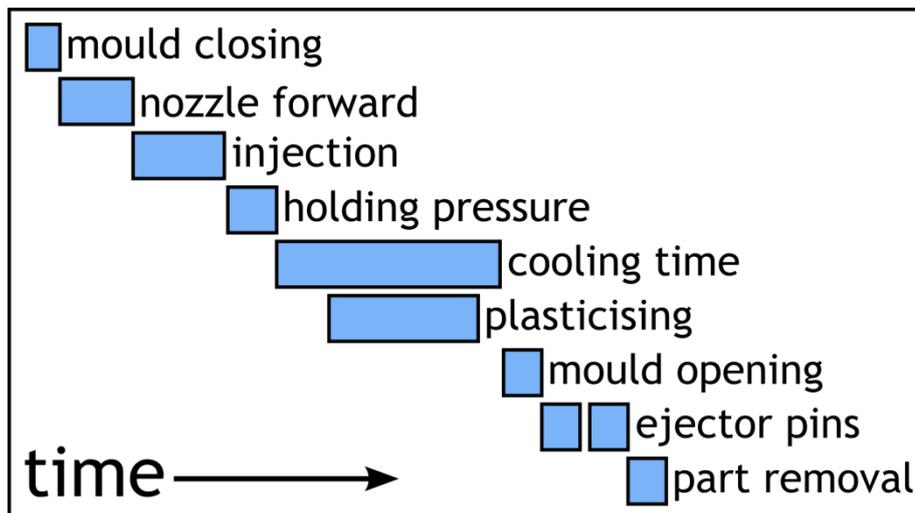
Figure 2.6 - Timeline of a single injection cycle.

There are a great many parameters that can be set on the moulding machine. General practice is to start off with the manufacturer's guideline values and then adapt conditions based upon observation of the parts produced. The following parameters are of particular importance:

Injection speed directly affects the injection time and injection pressure and dictates how quickly the polymer is forced into the mould. If it is too slow the polymer may freeze before it has fully filled the mould, leading to an incomplete part; too high and it may result in polymer being forced into unwanted areas of the tool (this is known as *flashing*).

Tool temperature affects how quickly the melt cools in the mould, if it is set too low it will result in poor filling, and if it is too high it can lead to an unnecessarily long cooling time or cause the part to not be fully frozen upon mould opening which can cause ejection problems.

Melt temperature directly affects the fluidity of the melt at the point of injection. If it is too low it will not flow well enough to fill the mould properly and if it is too high the cooling time may be unnecessarily long or, in extreme cases, the polymer may burn.

Holding pressure determines the pressure at which the polymer is held in the mould immediately after injection. As the part cools the polymer shrinks so holding pressure is required to push more polymer into the cavity to compensate for this shrinkage and ensure that a fully formed part is produced. Too low a value may result a concave drooping on the nozzle-facing surface of the part which is undesirable when a planar geometry is required.

Cooling time is a post injection, post holding pressure waiting period during which the tool remains closed so that the part may cool to an acceptable level, ideally the tool temperature. If cooling time is not sufficient the part may come out too hot and deform upon ejection; too long and you're just wasting time.

Moisture in certain polymers can affect its physical properties in a detrimental way which can cause a range of quality issues such as bubbles or streaks appearing in the moulded parts. This is why some polymers are dried before use.

2.3 Fabrication of inlays

Inlays are interchangeable samples which can be inserted and removed at will to change the pattern displayed on a single face of the mould cavity (Figure 2.5). For example, injection moulded compact disks are all the same size and shape, but it is the change of an inlay that means the difference between Debussy and Dire Straits, Mozart and Madonna. In this work inlays were fabricated from a number of materials in a number of ways, all of which are described in this section.

2.3.1 Substrate material

Single layer polymer inlays
Inlays for injection moulding were patterned by photolithography or nanoimprint lithography (NIL) in SU-8 3000 Series photoresist on one of 3 substrates: 740 μm thick Cirlex, 127 μm thick Kapton, 25μm thick Kapton.

Kapton® is a polyimide (PI) film produced by DuPont® which is stable up to around 400°C. The thinner it is, the more flexible it is, but all variants used in this work were thin enough to be cut with scissors. Cirlex® (Katco UK) is made from Kapton, but is thicker. While it can be cut with scissors it is preferable to machine it with an automated cutting tool when accuracy is required.

Dual layer *sandwich* inlays
SU-8 photolithography was used to fabricate microscale and millimetre scale *subtopographies* on Cirlex substrates. For injection moulding, subtopographies were placed in the frame with a 127 μm or 25 μm Kapton inlay on top of them. During moulding the flexible top layer would conform to the geometry of the subtopography, thus superimposing one pattern onto another.

Nickel inlays
Nickel inlays were fabricated by a LIGA like process. LIGA is a German acronym for Lithographie, Galvanoformung, Abformung (Lithography, Electroplating, and Moulding) wherein the sample is produced by galvanic electroplating of nickel over a pre-existing structure defined by another process such as EBL. This process was outsourced.

2.3.2 Photolithography

Photolithography is widely used in the microelectronics industry to create integrated circuits for mass produced electronic devices. By exposing a photosensitive material, known as a resist or photoresist, with light through a mask it is possible to define a pattern of microscale dimensions, with the minimum feature size related directly to the wavelength of the incident light. The exposed resist is chemically altered such that a subsequent aqueous development process will remove either the exposed or unexposed region depending on whether the resist is positive (exposed area is removed) or negative (unexposed area is removed). The remaining material can be used to define a pattern for further processes such as metal deposition or etching, or may form a useful structure itself. The JWNC is equipped with a Karl Süss MA6 mask aligner with which it is possible to define features down to around $1 - 2$ μm in size for thin resist layers. That value increases for thicker resists. A typical photolithography process proceeds as depicted by Figure 2.7.
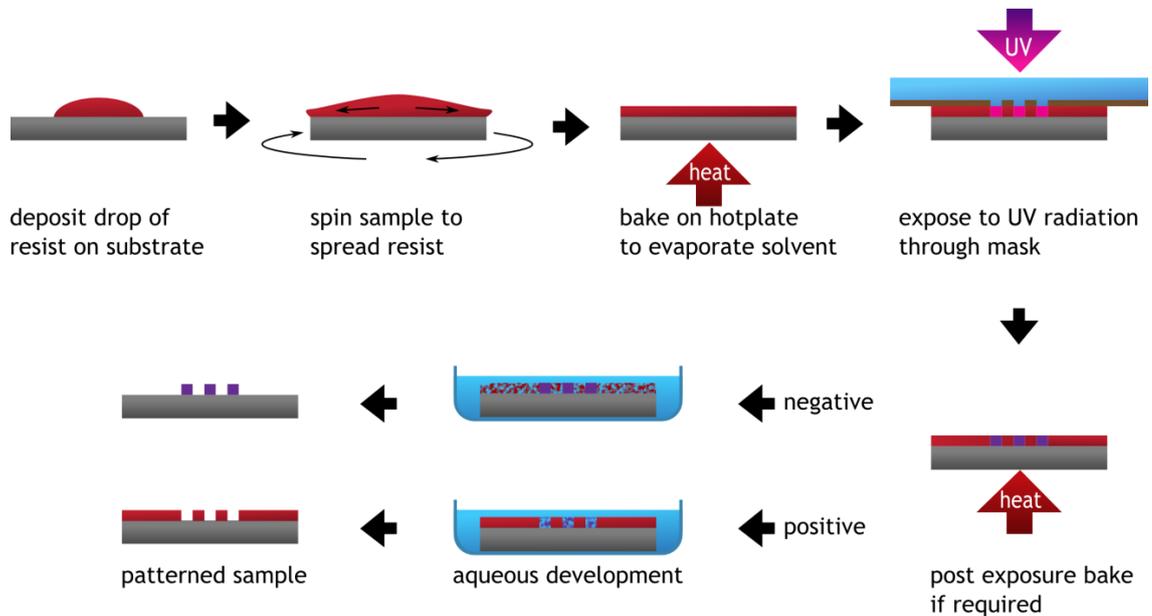
Figure 2.7 - A typical photolithography process.

In this work, SU-8 3000 series photoresist was used to form the actual structures on inlays. The process for this is summarised in the bullet points below and parameter details are given in Table 2.4 and Table 2.5.

- Clean sample in acetone, methanol and isopropyl alcohol (IPA) for 5 minutes each in ultrasonic bath.

- Expose to O_2 plasma for 1 minute at 200 W.

- Spin on resist according to Table 2.4.

- Remove edge bead if required.

- Bake on hotplate according to Table 2.4.

- Expose in MA6 mask aligner according to Table 2.5.

- Post exposure bake on hotplate according to Table 2.5.

- Develop in EC solvent according to Table 2.5.

- Rinse in IPA and dry with N_2.

- Bake in oven at 180ºC for 1-3 hours to harden resist.

Desired thickness (μm)	Variety & dilution (SU8:cyclopentane by volume)	Spin speed for 30 s (krpm)	Softbake time at 95ºC (mins)
2.6	3005 4:1	3	2
2.2	3005 2:1	3	2
1.9	3005 2:1	4	2
0.7	3005 1:1	3	1.5
3	3005 7:1	4	3
4	3005 7:1	3	5
10.5	3050 5:1	4	15
12.5	3050 5:1	3	15-20
16-18	3050 5:1	2	20-30
5	3005 neat	3	10
50	3050 neat	3	120-180
100	3050 neat	1	180-240

Table 2.4 - Resist spinning conditions for SU-8 3000 series photoresist obtained from experience during this project.

Substrate material	Resist thickness (μm)	Mask polarity	Min feature size (μm)	Exposure time (s)	PEB (at 95°C after 1min at 65°C)	Development time in EC solvent (mins)
Cirlex + 5μm 3005	0.6-0.7	Dark field	5	4-5.5	2:30	5
Cirlex	10	Dark field	5	14	2-3	5
Cirlex + 10μm 3050	10	Dark field	5	7	1-3	5
Cirlex (with or without precured baselayer)	5	Light field	5	13	1	5
Cirlex	50-100	Light field	10	40	1	30

Table 2.5 - Exposure and post exposure bake (PEB) conditions for SU-8 3000 series photoresist from experience obtained during this project. Exposure times are specific to Karl Süss MA6 mask aligner.

One of the challenges faced in this project involved photolithography with very thick (50 – 100 μm) layers of SU-8 3000 series photoresist. SU-8 is a negative resist with which attempts were made to fabricate deep holes that would be used to form tall pillars by injection moulding (see section 3.4.1). SU-8 is designed for the fabrication of thick structures, but I was operating at the limits of feasibility, attempting to produce holes with aspect ratios approaching 10:1 (i.e. 5 μm, 50 μm depth) which was made very difficult for several reasons which are depicted in Figure 2.8 and explained below.

The more viscous dilutions of SU-8 are designed to form thick layers when spun (e.g. SU-8 3050 will form a 50 μm layer when spun at 3000 rpm). Such layers tend to be less flat than their thinner counterparts and suffer from considerable edge beading, a phenomenon by which excess resist builds up at the edge of the sample and forms a rim several times thicker than the layer itself. Untreated, an edge bead causes the target area of the resist to be further away from the mask during exposure at the expense of focus which is detrimental to the quality of the features, causing them to deviate from their intended size. Edge bead can be removed through physical or chemical means, but some artefact of such a process generally remains which, together with the often non-flat target

area, can compromise the conformity of the contact between the mask and resist during exposure (Figure 2.8 – left).
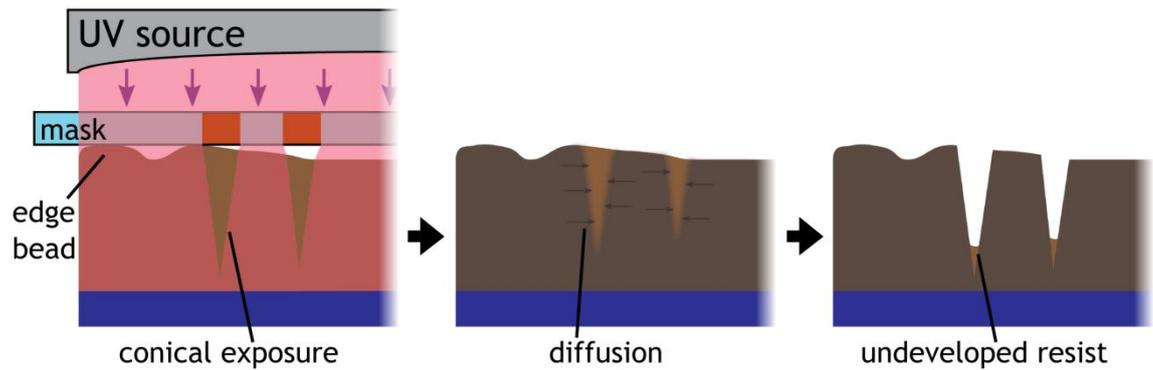
Figure 2.8 - Difficulties with high aspect ratio photolithography in SU-8.

Even with a perfect spun layer, the nature of light itself makes it difficult to obtain the desired feature size in a thick resist. The diffraction which occurs as the light passes from the mask changes the direction of the exposure causing a sloping of the ideally vertical sidewalls which, for example, will make intended cylinders tend towards a conical morphology (Figure 2.8 – all).

The exposure of SU-8 does not cure the material immediately. It merely activates an acidic precursor which must be heated before the full chemical change occurs. This precursor may diffuse laterally in the intervening period between exposure and this post exposure bake (Figure 2.8 – middle) as well as during the early stages of the PEB which must be gradual to prevent stress induced cracking. This diffusion can adversely affect the sharpness of features and cause their size to differ significantly from what was intended.

The energy delivered to the SU-8 during exposure may also diffuse somewhat, so when attempting to make holes in SU-8 the appropriate dose will be somewhat lower than if the polarity were reversed due to the larger ratio of unmasked to masked area. With a thick layer, however, a relatively large dose is required to ensure that enough energy is delivered to the resist at the bottom of the layer. If the resist is not fully exposed at the base the entire layer will delaminate during development. The fine balancing act between these two requirements is yet another limiting factor to what is possible with this material and this technique. In addition to these factors, you are also faced with a very long development time (~15 minutes) if all the unexposed resist is to be fully removed from the deep hollows (Figure 2.8 – right).

A number of options exist to mitigate this plethora of challenges, and were employed in this work to make photopatterned inlays capable of producing the injection moulded structures seen in the next chapter, Figure 3.4. These included the use of an optical filter to limit the MA6's exposure to the I-line wavelength to which SU-8 is most sensitive and, at 365 nm, is at the short end (higher

resolution, less diffraction) of the MA6's mercury lamp's emission spectrum. Extended soft bake times greatly beyond the manufacturer's guidelines helped to remove excess solvent, limiting the potential for post exposure diffusion, and a great amount of care for the flatness of the spun layers and fine tuning of exposure times also served to aid the cause. As a result of these efforts, the inlays fabricated went on to produce injection moulded pillars of 10 μm diameter with heights of around 75 μm, albeit with a significantly reduced diameter and rounded morphology toward the tip.

2.3.3 Nanoimprint lithography

Nanoimprint lithography (NIL) is a bit of misnomer in that it does not actually involve a conventional lithographic process like that of electron beam or photolithography. It is more similar to hot embossing but differs by merit of a chemical change in the imprinted material which can be mediated by heat, radiation or both. The imprint material of choice in this project was SU-8 3000 series photoresist which is cured by exposure to UV radiation in the I-line (wavelength = 365 nm) and a simultaneous or subsequent bake at 95°C or higher. A summary of the NIL process used in this project is depicted in Figure 2.9 with more details appearing later in this section.
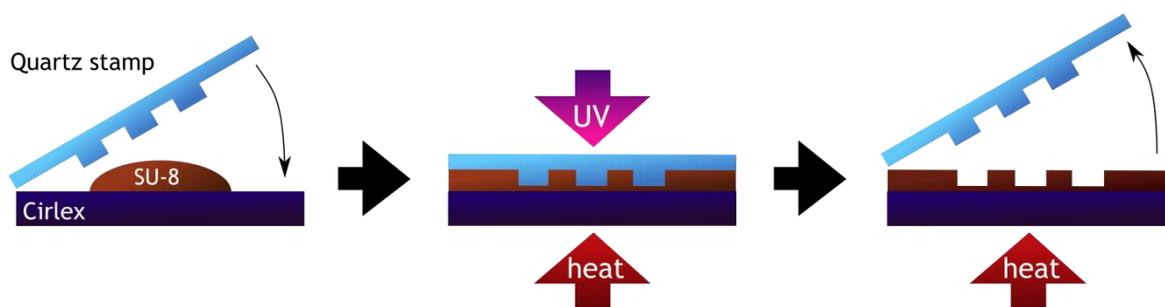
Figure 2.9 - NIL with SU-8 on Cirlex using a quartz stamp. The stamp is applied at an angle to prevent air bubble entrapment.

NIL processes used in this project made use of two thermal imprint devices present in the JWNC and several iterations of custom made imprinting tools, the *pocket imprinters*, named for their small, portable form factors.

The two large thermal imprinters used were a Specac press and an Obducat NIL-2M-OB-PL-LW-230V NIL tool. The Specac is a simple device comprising two heated plates and manually activated hydraulics with which to clamp the two plates together, with the stamp and substrate in between, with a force of up to 50 kN. The Obducat is a more specialised device with computer aided control and a pump that allows thermal imprints to be performed under vacuum. Unfortunately, neither device provided very satisfactory results, particularly when nanoscale features and/or high aspect ratios were concerned. The reasons for this are not totally clear, but with the Specac it was difficult to maintain a constant pressure and the Obducat had a tendency to lose its vacuum and/or clamping pressure mid-imprint with the restrictive computer control making it impossible to intervene and correct the fault at the critical moment. Even if a good imprint was

obtained, neither device had the ability to expose the SU-8 to the UV radiation required to cure it, forcing this do be done at a later stage followed by a post exposure bake which would reflow the material enough to obscure any nanopattern before the solidification of the curing process fully occurred. It seemed to be that SU-8 could not be reliably nanopatterned with thermal imprinting alone, so the custom pocket imprinters were created for a solution involving UV.

The first pocket imprinter (hereafter known as version 1.0) was designed by Ali Khokhar[112] and made in the university's mechanical workshop. It is pictured in Figure 2.10. This device allows the stamp and substrate to be clamped together in an aluminium frame with a force applied by some internal springs and UV radiation provided by an LED at a wavelength of 365 nm. It does not, however, allow for any simultaneous heating which not only means that a post imprint bake is required to cure the SU-8, but also that it had to retain its solvent content for the imprint stage (photoresists are generally designed to have their solvent content removed by soft baking after being spun onto the substrate) so that the material is able to flow around the features of the mould, making unwanted bubbles a likely occurrence.
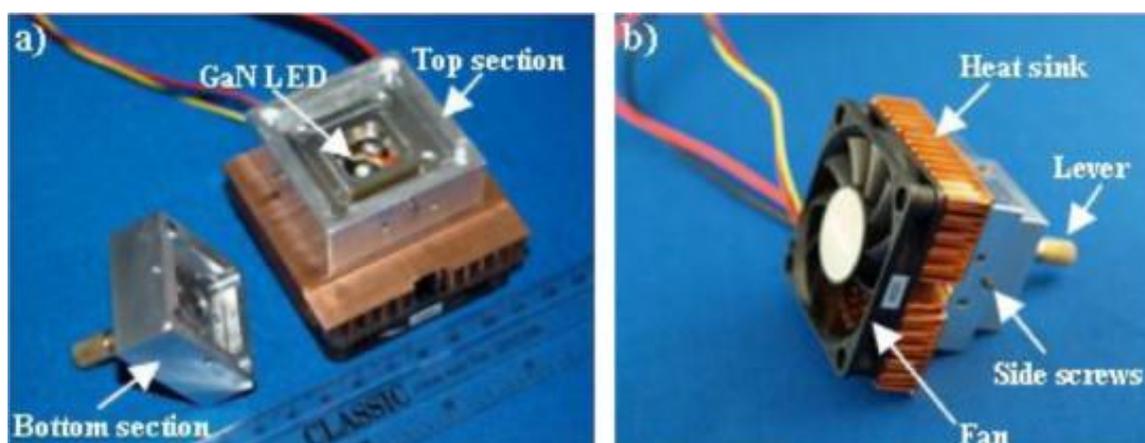
Figure 2.10 - Photographs of pocket imprinter version 1.0. Image taken from reference [112].

Pocket imprinter version 2.0 (pictured in Figure 2.11) was designed as a simple thermal imprinter which contains a spring activated pressure plate similar to that of version 1.0 and is intended to sit atop a hotplate during the imprint process. This device was intended to be a portable alternative to the Specac and Obducat for purely thermal imprinting or embossing of any suitable material.
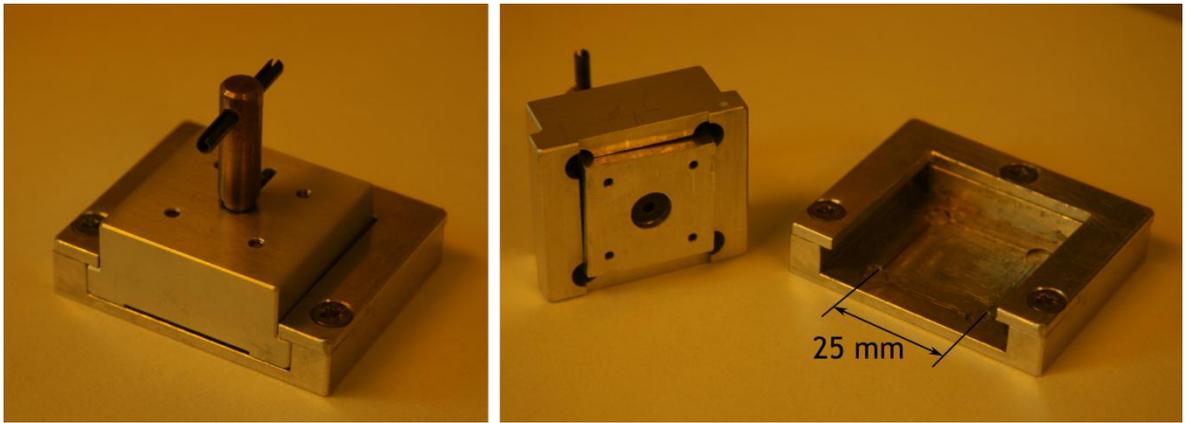
Figure 2.11 - Photograph of pocket imprinter version 2.0 in close (left) and open (right) positions.

Pocket imprinter version 3.0, and subsequent refinement version 3.1 (version 3.1 leaves a larger unexposed region around the edge to facilitate a better seal with the frame of the injection moulding machine), pictured inFigure 2.12, were designed for the imprinting of SU-8 with a transparent (usually quartz) stamp and allows simultaneous heating and UV exposure. It does not contain springs or any means by which to apply a particular force other than that attributed to its own weight, and is really little more than an appropriately shaped housing for a 365 nm UV LED and 25 x 25 x 1 mm quartz stamp which rests upon the substrate housed in an aluminium frame to restrict lateral movement.
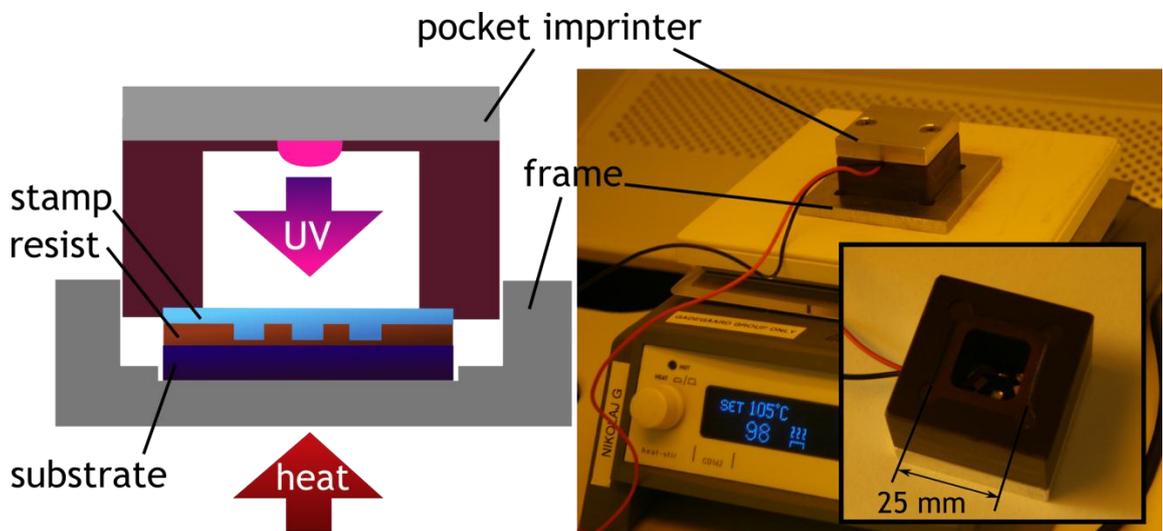
Figure 2.12 - Schematic diagram and photograph of picket imprinter version 3.1 during UV-NIL process. A view of the underside of the device is also provided (inset).

This entire setup is placed on a hotplate and provided the most successful SU-8 imprints of any of the NIL tools discussed in this section. An imprint with a 3rd generation pocket imprinter would proceed as follows:

- Clean substrate and expose to oxygen plasma at 200 W for 1 minute to activate surface to improve adhesion.

- Place a drop of SU-8 3050 on substrate and bake at 105°C for 2-3 hours to remove solvent content.

- Place frame on hotplate and heat to 100°C.

- Place substrate in frame and leave for 4 minutes.

- Slowly lower quartz stamp face down onto sample as carefully and gradually as possible. If the stamp is applied at an anglethe formation of air bubbles will be minimised.

- Allow SU-8 droplet to spread out beneath stamp, pressing gently to allow any air bubbles to escape via the edge.

- Ensure substrate and stamp are located centrally within the frame and carefully place pocket imprinter on top of the stamp.

- Wait 4 minutes to allow the assembly to relax and let SU-8 flow around the features of the stamp.

- Turn on UV LED and wait for 3 minutes for curing to occur.

- Turn off LED and remove imprinter.

- Carefully separate stamp from substrate with a razor blade. This is performed on the hotplate at imprint temperature to minimise stress caused by differences in the thermal expansion properties of the two materials.

- Place stamp and imprinted sample in acetone to dissolve unexposed SU-8 from the edges.

- Oven bake inlay at 180°C for at least 1 hour to harden SU-8.

2.3.4 Chemical vapour and induction coupled plasma deposition

Induction coupled plasma (ICP) and chemical vapour deposition (CVD) were used to deposit SiO_2 and Si_3N_4 onto inlays for the purposes of experiments described in Chapter 4 and Chapter 5. These processes were conducted by lab staff and the details are presented in Table 2.6.

Process	Pressure (bar)	Temperature (ºC)	RF power (W)	Gas 1 / flow rate (sccm)	Gas 2 / flow rate (sccm)	Gas 3 / flow rate (sccm)
ICP Si_3N_4	4.4	35	100	SH_4 / 7.2	N_2 / 6	-
CVD Si_3N_4	1000	300	20	SH_4 / 8	N_2 / 170	NH_3 / 16
CVD SiO_2	1000	300	15	SH_4 / 7	N_2O / 200	N_2 / 85

Table 2.6 - ICP and CVD deposition parameters for inlay surface coatings.

2.3.5 Metal deposition

Some inlay surface coatings were applied by metal deposition using electron beam evaporation in either of two Plassys MEB550S metal evaporation tools. The processes were already established so no development or refinement was required.

2.3.6 Deposition of fluorosilane layers

Trichloro(1H,1H,2H,2H-perfluorooctyl)silane (TPFS) was used as a non-adhesive coating on some inlays and all stamps. It was deposited by vapour deposition in the following process:

- Expose sample to O_2 plasma for 1 minute at 200 W.

- Place sample in petri dish on a hotplate at 150-200°C beside a small drop (approx. 50 μl) of the TPFS solution.

- Wait for 15 minutes then remove sample.

- Rinse sample in RO water, acetone and IPA then dry with N_2.

2.4 Fabrication of stamps

Samples to be used as master stamps for NIL were fabricated in silicon and quartz using electron beam lithography (EBL), metal lift-off and dry etch. Photolithography was occasionally used for making microstructured stamps, but for the majority of the results in this thesis the structures were below the resolution limit of this process so EBL was used. A typical stamp manufacture process incorporating EBL using poly(methyl methacrylate) (PMMA) as the resist, metal lift-off with

nichrome (NiCr) and dry etch with CHF_3 and argon plasma is depicted in Figure 2.13, with details on the constituent methods detailed in the remainder of this section.

deposit drop of PMMA on quartz substrate

spin sample to spread resist

bake on hotplate to evaporate solvent

heat

deposit charge conduction layer

Al

e-

e- e- e-

expose in beamwriter

removal of Al

development

deposit etch mask

NiCr

e-

lift-off

CHF₃/Ar

dry etch

mask removal

completed stamp

vapour fluorination

heat
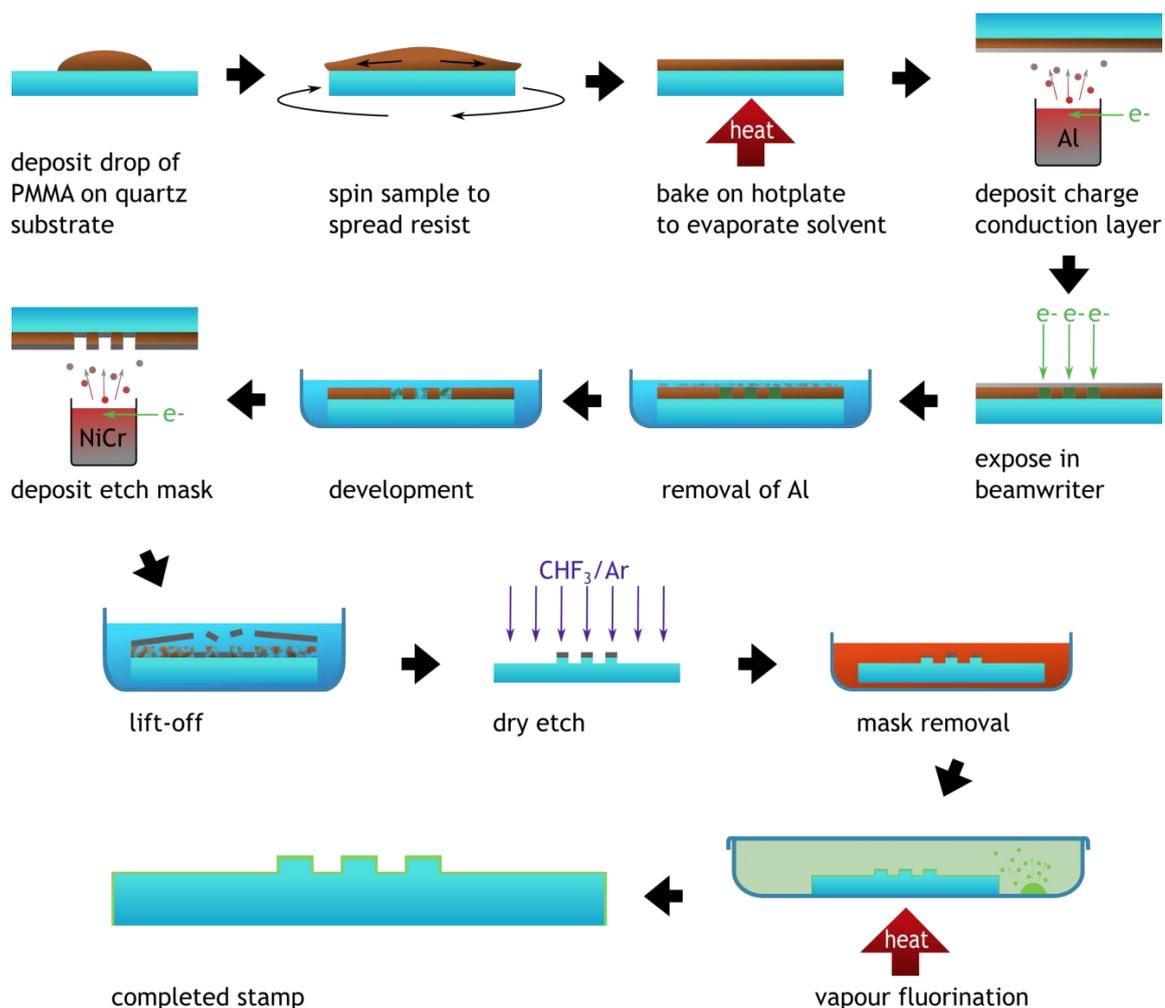
Figure 2.13 - Fabrication of a quartz stamp.

2.4.1 Electron beam lithography

Electron beam lithography (EBL) is similar in principal to photolithography except the energy used to define the pattern in the resist comes from secondary electrons generated by a high energy primary beam rather than from electromagnetic radiation and it can be used to define features below 10 nm in size. EBL is not commonly used for mass production because it is a serial write process and thus is time consuming, but it is useful for prototyping and for small volume production. The Vistec VB6 UHR EWF electron beam writer tool in the JWNC was used extensively in this project to fabricate submicron features.

For the purposes of this project, one of the most commonly fabricated types of structure that had to be made were pillars with diameters in the region of 100 nm. EBL generally defines structures by

building them gradually through the exposure of the resist as a series of pixels. The centre to centre spacing between each pixel, known as the VRU, is generally slightly smaller than the beam diameter so subsequent exposures overlap and the cumulative result is that of a continuous shape. However, when the intention is to define an array of individual circles, that will ultimately go on to form nanopillars, it is faster to use a process known as dot writing in which each feature can be defined by a single pixel, with the VRU acting as the pitch between each feature. This principal is illustrated in Figure 2.14. This also makes pattern design simpler as all that is required is a single solid block to define the extent of the dot array, rather than having to account for each and every circle.
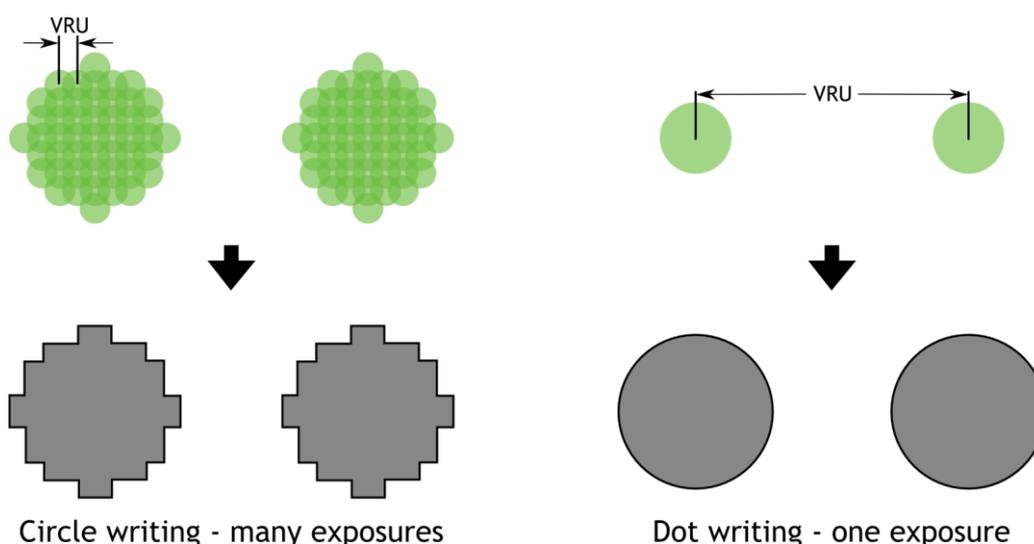
Figure 2.14 - Circle writing vs. dot writing.

The amount of energy required to expose the resist, known as the dose, depends on the properties of the resist, the dimensions of the desired features and their proximity to one another. This quantity is conventionally expressed in μCcm^{-2} and for a fixed pitch one would obtain larger dots with a higher dose and smaller dots with a lower dose. This relationship, however, becomes somewhat less intuitive when the pitch is varied as, to retain the same size of dot, the dose must be reduced for a sparser array and increased for a denser pattern. The confusion arises because the dose is expressed in terms of charge per unit area when perhaps charge per dot might be more appropriate. Imagine a single square centimetre upon which dots are to be exposed with a dose of x μCcm^{-2}, each dot will receive an individual dose of y μC, where $y = \frac{x}{number\ of\ dots}$. Now increase the spacing between each dot such that there are half the amount of dots within that 1 cm^2 box, then each dot would receive a dose of $2y$ μC causing them to be bigger than they were at the original pitch. In order to keep them the same size the dose when defined as a charge per unit area must be reduced by a factor of two so that the charge per dot remains the same. This project required that similarly sized dots be patterned with a variety of pitches so it was often necessary to think in terms of dose per dot rather than conventional dose. The results of a number of dose tests and other jobs

in which dots were written in PMMA on quartz were collated and put together to form the plot in Figure 2.15 which serves as a guide for determining the appropriate dose to produce the desired size of dot at any pitch with a square grid geometry. The formula to convert from charge per dot into charge per unit area is given below the figure where D is dose in μCcm^{-2}, Q is charge per dot in fC and ρ is dots per unit area in cm^2 which will depend on the desired pitch and the geometry of the dot spacing.

$$D = \frac{Q}{\rho}$$
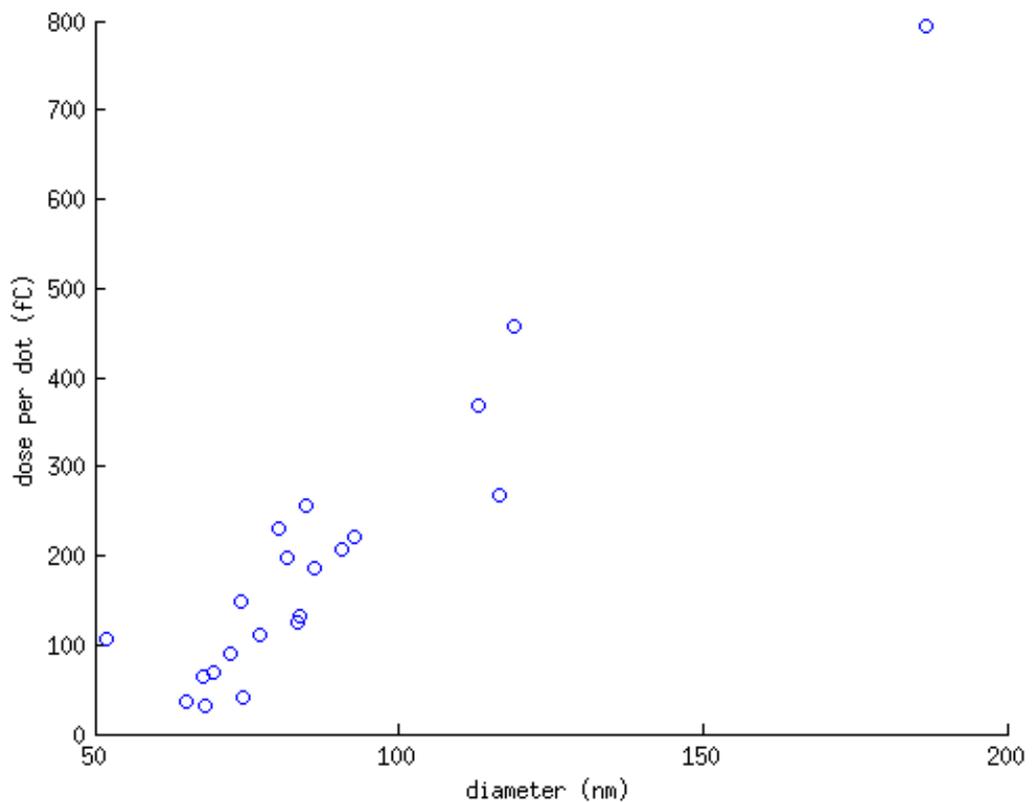
Figure 2.15 - Plot relating dose per dot to diameter for one dataset collated during this project.

The vast majority of EBL work conducted in this project used poly(methyl methacrylate) (PMMA) as the resist on quartz substrates with a 10 nm Al charge conduction layer. The procedure for such a process is as follows:

- Clean sample in acetone, methanol and isopropyl alcohol (IPA) for 5 minutes each in ultrasonic bath.

- Dehydration bake in oven at 180ºC for 1 hour.

- If a bilayer is desired spin low molecular weight PMMA (2010 dilution) at the appropriate speed to obtain a thickness of around twice the depth of the intended subsequent metal deposition.

- Oven bake at 120ºC for 20 minutes.

- Spin high molecular weight PMMA (2041 dilution). In the case of a bilayer ensure thickness is greater than the intended subsequent metal deposition depth. In the case of a single layer aim for at least twice the metal deposition depth.

- Clean back of sample with acetone and cotton bud.

- Oven bake at 120ºC for 20 minutes.

- Deposit 10 nm Al charge conduction layer.

- Expose in beam writer with the appropriate dose for the pattern.

- Remove charge conduction layer by immersion in 49:1 RO water : Tetramethylammonium Hydroxide (this dilution is known as CD26) for 2 minutes.

- Rinse in RO water and dry with N_2.

- Develop in 2.5:1 IPA: Methyl isobutyl ketone(MIBK) at 23ºC for time (minutes) = 0.3 x resist thickness (nm).

- Rinse in IPA and dry with N_2.

2.4.2 Metal deposition and lift-off

As well as being used to deposit some inlay surface coatings (section 2.3.5), metal deposition by electron beam evaporation was uses for two purposes in the stamp fabrication process: charge conduction layers and hard masks for dry etch.

Charge conduction layer: In EBL the sample must be conductive to prevent the charge from the electron beam building up and reducing the quality of pattern writing. Typically a 10-20 nm layer of aluminium was used for this.

Etch mask: During an etch it is usually desirable to protect some areas of the sample whilst etching the others. This can be done with a number of materials including resist, several metals

and oxides. This project made extensive use of NiCr as an etch mask for both quartz and silicon samples. Patterning of an etch mask is done by a lift-off process (see Figure 2.16) in which metal (or another material such as chemical vapour deposited oxide) is deposited on top of a pre-patterned resist layer. After deposition the resist is dissolved, leaving the metal on the sample forming a pattern which is the inverse of that originally present in the resist.

patterned resist on sample → deposition (sputtered/evaporated metal, CVD etc.) → lift-off (resist dissolved) → inverted pattern now on sample
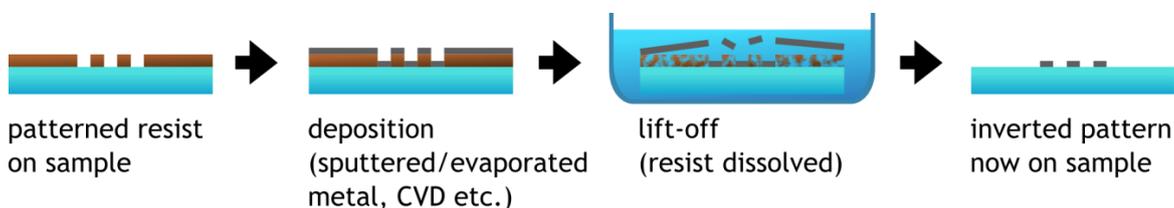
Figure 2.16 - Generic lift-off process.

2.4.3 Dry etch

Dry etching is a destructive fabrication process in which material is removed by bombarding it with high energy plasma, with the aim usually being to transfer a pattern on a sample's surface into the bulk of the substrate material. The specific combination of reactive and passivating ions used depends on the substrate material(s) and the resulting physical profile that is desired. The primary advantage of dry etching over wet etching is that it is relatively easy to obtain anisotropic profiles (straight sidewalls) while a wet etch tends to follow the crystalline structure of the substrate material which usually results in a predictable yet sloping profile.

In this project dry etching was performed on silicon and quartz substrates in the latter stages of stamp fabrication using the JWNC's STS ICP and Oxford 80+ RIE tools respectively. Dry etch processes were performed by lab staff and are detailed in Table 2.7 where the material selectivity to NiCr is also supplied as this was the etch mask of choice in most situations.

Etch description	Pressure (bar)	Temp (ºC)	RF Power (W)	Gas 1 / flow rate (sccm)	Gas 2 / flow rate (sccm)	Etch rate (nm/min)	Selectivity to NiCr
Si nano etch	2	22	100	Ar / 2	-	100	>100:1
Si micro etch	10	20	9	C_4F_8 / 50	SF_6 / 40	500	~1000:1
Quartz etch	30	20	200	CHF_3 / 25	Ar / 18	40	~10:1

Table 2.7 - Dry etch processes used in this project.

2.5 Sample characterisation

2.5.1 Optical microscopy

Optical microscopy is a ubiquitous technique used in many professions to inspect small objects by means of the magnification provided by the lenses of a microscope. With an optical microscope, the minimum resolvable lateral distance between two objects (R) is limited by the wavelength of the light being used (λ) and defined by the Rayleigh criteria as:

$$R = 0.61 \frac{\lambda}{NA}$$

where NA is the numerical aperture of the objective lens which itself is defined by:

$$NA = n \sin \theta$$

where n is the refractive index of the viewing medium (air in all cases in this project, n of air = 1) and θ is the angle of the point of the cone of light observable by the objective lens as shown in Figure 2.17.
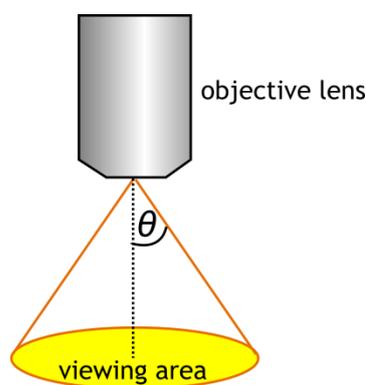
Figure 2.17- Depiction of the viewing angle that defines the numerical aperture of a lens.

In this project all optical microscopy was conducted with air (n =1) as the medium of light propagation which imposes a maximal limit on NA of a little less than 1, meaning that the smallest resolvable distance between features was a slightly larger than half the wavelength of visible light, around 350 nm or so, but in practice the imaging of objects near this theoretical limit does not provide the clarity to make accurate measurements of their size, serving more as a guide that could later be examined more closely with another technique. As the majority of the structures produced in this work were smaller than this limit, optical microscopy was predominantly used as a means to assess quickly the overall quality of a fabrication step with electron microscopy and atomic force microscopy being used to make more precise measurements.

2.5.2 Scanning electron microscopy

A scanning electron microscope (SEM) uses electrons rather than light as the means of illuminating the sample of interest, making it possible to resolve much smaller features (of the order of only a few nanometres if the microscope and user are both working well). Typically, it is possible to make useful measurements of structures around 20 – 100 nm in size and larger with the JWNC's Hitachi S4700 and FEI Nova NanoSEM 630 microscopes.

SEMs operate under vacuum conditions, firing a beam of electrons at the sample, detecting the secondary electrons scattered by this primary beam and converting what is detected into a greyscale image displayed on a computer screen. The use of high energy electrons is destructive and may damage the sample, depending on its constituent materials. Metals generally cope well as they are able to dissipate the energy, but polymeric materials such as those of injection moulded samples can often be seen to warp as they absorb this energy, often causing pillars to bend substantially if they are exposed for too long. It is also usually a requirement that a sample be conductive for SEM imaging to prevent the build-up of charge in a small area and allow a useful range of contrast. This can be done by coating a non-conducting sample in a layer of metal, for which a gold-palladium sputter coater was employed frequently during this project. The FEI Nova NanoSEM 630 provides a useful alternative to this for situations where Au/Pd coating might be undesirable. It provides a couple of specialised detectors which operate in a low vacuum mode where the atmosphere is permeated by water molecules which take on the role of conducting the charge away. This technique was used frequently for the examination of quartz masters throughout their fabrication process when the addition of a metal layer would have been detrimental to the on-going process and final function of the stamps.

2.5.3 Atomic force microscopy

Atomic force microscopy (AFM) is a type of surface profilometry capable of measuring the heights of features and roughness of surfaces with sub nanometre accuracy. A physical probe, or tip, on the end of a cantilever is dragged across the surface and as it encounters topographical features the cantilever is bent which alters the reflected position of a laser beam pointed at the cantilever. These subtle changes in position are detected and translated into a relative difference in the height at that position on the sample. As the scan progresses, a picture is built up of the topography of the sample as seen by the moving tip, with resolution and accuracy being determined by the speed of the scan and the force behind the tip. AFMs can be operated in a number of modes relating to how the tip is moved to build up the scan. In this project a mode in which the tip rapidly oscillates over the sample, only making contact for brief moments, was used exclusively. Known as tapping mode, it is preferable to a continuous dragging motion as it minimises both wear and tear to the tip and the chance of it accruing a collection of any particles present on the surface.

As the tip is a physical object of a certain size, it is important to consider the effect of this and the artefacts it may induce in the resulting data. Figure 2.18 illustrates the principal of AFM operation (top) as well as a number of potential tip-related issues that can occur.
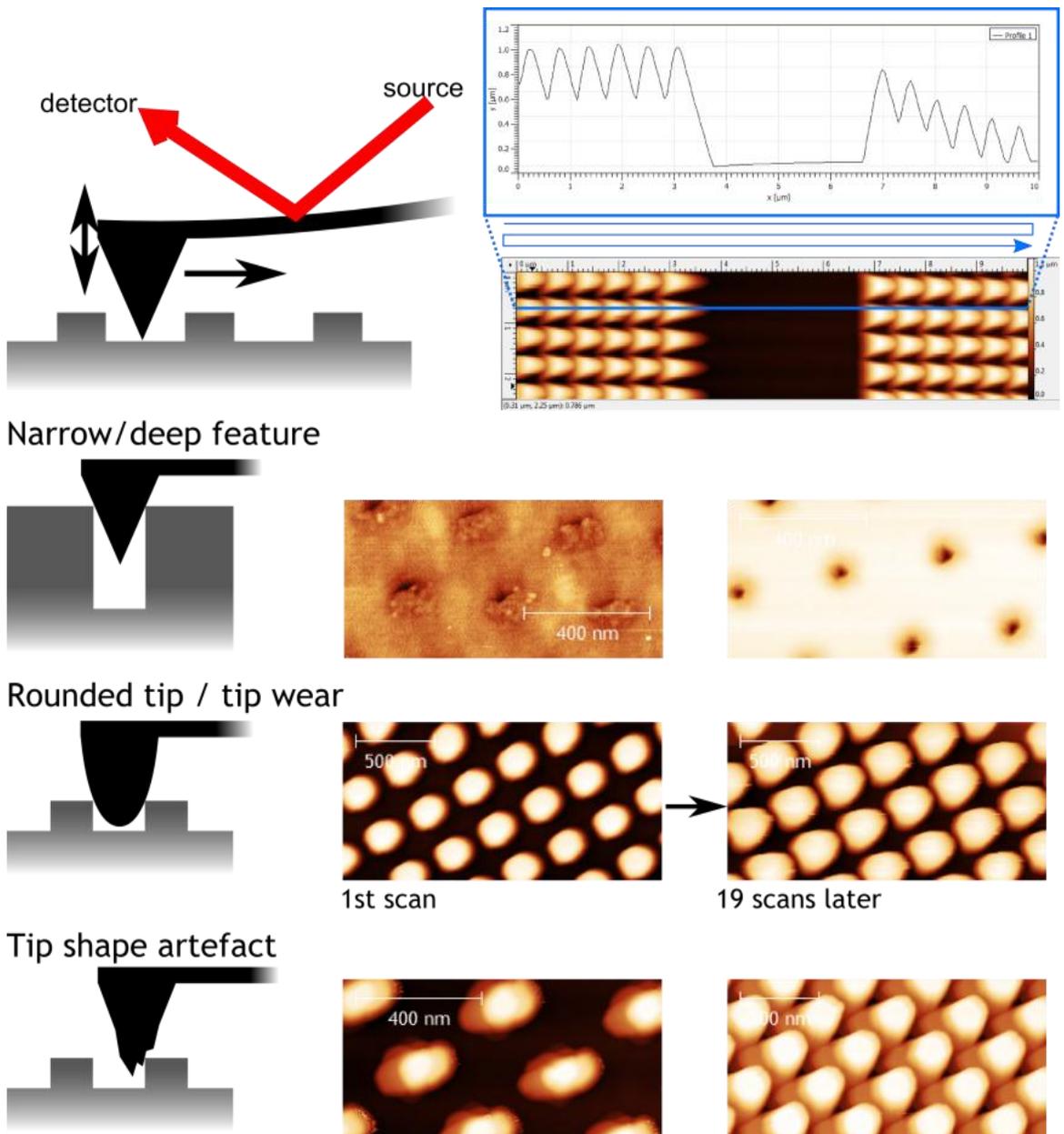
Figure 2.18 - Illustration of AFM function and some potential pitfalls.

The lateral movement of the AFM tip is controlled by a piezoelectric material which is subject to a certain degree of drift, particularly when its range is recently changed, so it is common to see features appear to move sideways, or lateral dimensions to appear contradictory to those expected. As a result of this and the limitations illustrated in Figure 2.18 all AFM scans require a degree of informed interpretation, but the technique is still unrivalled in its ability to make accurate high resolution measurements of the heights of nanometre scale features.

2.5.4 Water contact angle

Water contact angle (WCA) analysis is a very useful tool for the analysis of both surfaces and surface structures. The angle a drop of water (or indeed any liquid) makes upon contact with a solid (or denser liquid) surface is illustrative of the interaction between the two substances. Practically, it provides a useful analogue to surface energy facilitated by the type of functional chemical groups which may be present on a surface, a phenomenon which correlates directly with its adhesive properties. For example, SiO_2, the compound which forms glass, quartz and the surface of a silicon wafer, has a relatively low contact angle (~20°) which is indicative of a high surface energy which allows it to readily bond to other materials. This angle can be decreased further by the action of high energy plasma which breaks chemical bonds on the surface thereby raising the surface energy and causing a water drop to adopt an almost flat morphology. In the spheres of replication based fabrication such as NIL and injection moulding, it is desirable to minimise the surface energy (maximise the WCA) of interacting materials so that they will demould smoothly and not cause deformation or damage to the structure of the stamp or its negative replica. To this end, techniques like fluorination (see section 2.3.6) are used to deposit the appropriate chemistry on a surface that it might mitigate these detrimental interactions.

On surfaces which contain a topographical structure much smaller than a water drop (i.e. micro/nanostructure or roughness) the WCA can be radically increased. Indeed, it is by means of nanoscale surface structure that the lotus leaf famously exhibits superhydrophobic properties.[14] When hydrophobicity is mediated by surface structure, it falls into one of two wetting states: the homogeneous state, in which the drop fully conforms to the surface topography, and heterogeneous state where surface tension keeps the drop suspended on the tips of the surface structure. These two states are illustrated in and are characterised by the famous Wenzel and Cassie-Baxter equations respectively.[16]
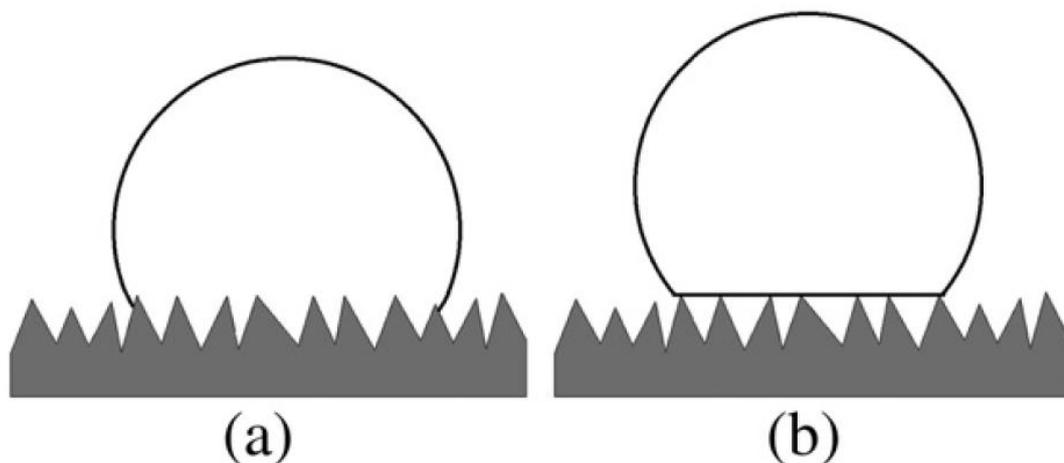
Figure 2.19 - Homogeneous (a) and heterogeneous (b) wetting states of a topographically structured or rough surface. Image taken from reference[15].

Despite the fact that not-wetting surfaces are a potential application of the processes developed in this project, there was no WCA characterisation of topographically structured surfaces performed. The technique was used exclusively as an indicator of the non-adhesive properties of inlay surface coatings in Chapter 4. For this type of characterisation, three types of measurement were taken: static WCA, advancing WCA and receding WCA, (see Figure 2.20) with the difference between the latter two being calculated to determine a quantity known as the contact angle hysteresis (CAH). Yan *et al*[15] state that:

> *"To describe a superhydrophobic state, the static angle as well as the CAH should be measured both. For an extremely stable superhydrophobic state, its static contact angle should be as high as possible, and its CAH as small as possible, otherwise the achieved wetting state might transit to a different one."*

Therefore it was decided that a measure of both provide greater insight into the nature of the surfaces in question than the static angle alone.
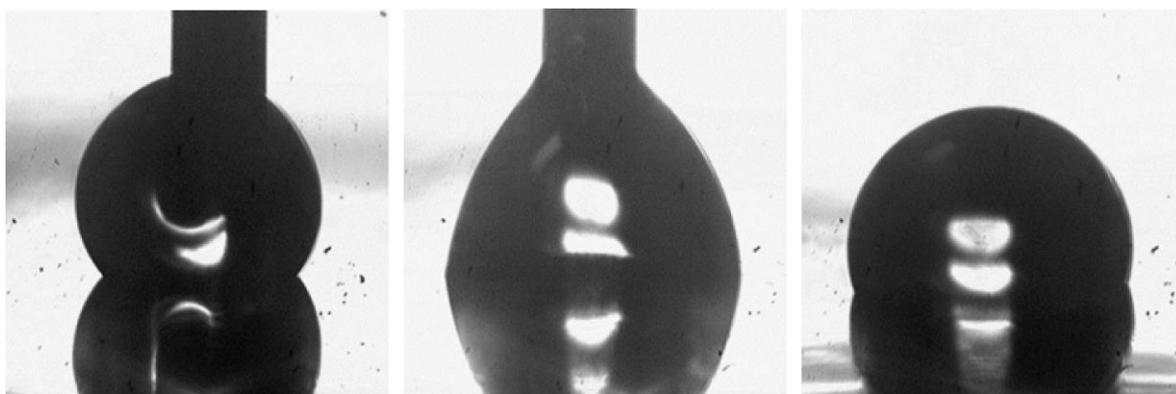
Figure 2.20 - Left to right: advancing receeding and static sessile drops captured with the apparatus used in this project.

WCA measurements were carried out using the sessile drop method[113] on a self-made apparatus comprising a back lit stage and a x10 microscope objective positioned on its side with a camera attached. Water drops were supplied manually by a microliter syringe located above the stage and a relatively constant drop volume was ensured by measuring only drops that almost completely filled the field of view. Advancing, receding and static water drops were recorded as video and split into individual frames in ImageJ. After irrelevant frames (such as those captured before drop initiation) were discarded, between three and six frames for each experimental condition were analysed using the DropSnake plugin (freely available from http://bigwww.epfl.ch/demo/dropanalysis/) in ImageJ. Means and standard errors calculated from these measurements were used to characterise the surfaces in question.

2.5.5 X-ray photon spectroscopy

X-ray photon spectroscopy (XPS) is a surface analysis technique that makes it possible to determine the elemental composition of the uppermost 5-20 nm of a surface. In XPS surface bound electrons are excited by incident x-ray radiation causing them to be ejected from the surface. These electrons are detected and the elements from which they originated determined by cross referencing their kinetic energies with known energy levels unique to specific elements. The results are presented as a percentage of the total number of electrons counted from the surface by integrating the area under peaks in the binding energy spectrum and subtracting the x-ray source associated background noise.

A SAGE 100 XPS machine with a spatial resolution of approximately 6 mm was used to characterise the surfaces of inlay coatings used in Chapter 4.

2.6 Software

2.6.1 Simulations

Simulations were conducted in Comsol Multiphysics software using simple models which are described where they are used.

2.6.2 Image analysis

ImageJ (available freely from http://rsb.info.nih.gov/ij/) was used for all quantitative image analysis with subsequent data processing being done in Matlab and/or spread sheet software if required.

Top down SEM image analysis, such as that used in Chapter 4 proceeded as indicated in Figure 2.21 and the bullet points below it.

original image

cropped binary image

	HV	mode	WD	det	mag	tilt		— 10 µm —
	10.0 kV	SE	6.0 mm	TLD	10 000 x	0 °		

Results

File   Edit   Font   Results

	Label	Area	Perim.	Circ.	Feret	FeretX	FeretY	Fer
2616	binarySEM.png	35908.485	854.187	0.618	287.978	12660.819	24122.807	15
2617	binarySEM.png	36763.449	861.282	0.623	314.922	13157.895	24122.807	15
2618	binarySEM.png	30778.701	730.133	0.726	277.393	13654.971	24210.526	18
2619	binarySEM.png	28213.809	637.397	0.873	249.825	14210.526	24239.766	20
2620	binarySEM.png	35053.521	771.485	0.740	298.188	14649.123	24152.047	16
2621	binarySEM.png	32488.629	688.782	0.861	251.530	15233.918	24269.006	35
2622	binarySEM.png	31633.665	671.654	0.881	269.577	15730.994	24298.246	40
2623	binarySEM.png	32488.629	688.782	0.861	275.847	16198.830	24239.766	32
2624	binarySEM.png	29068.773	671.654	0.810	251.530	16754.386	24298.246	54
2625	binarySEM.png	33343.593	688.782	0.883	277.393	17192.982	24210.526	18
2626	binarySEM.png	35908.485	747.262	0.808	287.978	17690.058	24122.807	
2627	binarySEM.png	32488.629	713.005	0.803	269.577	18684.211	24210.526	12
2628	binarySEM.png	30778.701	671.654	0.857	261.528	19210.526	24239.766	26
2629	binarySEM.png	31633.665	754.356	0.699	277.393	19678.363	24152.047	16
2630	binarySEM.png	31633.665	688.782	0.838	251.530	20233.918	24269.006	35
2631	binarySEM.png	31633.665	705.910	0.798	277.393	20672.515	24181.287	18
2632	binarySEM.png	31633.665	730.133	0.746	277.393	21169.591	24181.287	18
2633	binarySEM.png	30778.701	671.654	0.857	269.577	21695.906	24152.047	16
2634	binarySEM.png	29923.737	647.431	.897	251.530	22222.222	24239.766	35
2635	binarySEM.png	34198.557	781.518	.704	305.272	22631.579	24152.047	16
2636	binarySEM.png	31633.665	771.46	68	298.188	23157.895	24152.047	16
2637	binarySEM.png	36763.449	812.83	699	314.922	23654.971	24093.567	15
2638	binarySEM.png	34198.557	854.187	589	326.911	25116.959	24152.047	16

further processing

analyse particles

Figure 2.21 - Summary of the analysis method for a SEM image used in Chapter 4.

- The image is cropped to a predetermined size with the crop boundary aligned so as to ensure the same number of columns and row are included in each image.

- The image is converted to binary form. Contrast is adjusted prior to this if initial attempts do not yield a satisfactory representation of the original.

- The *Analyse Particles* function is run with particles on the edge and outwith a predetermined size being ignored.

- The results appear in a table and are saved as comma delimited text for subsequent processing.

2.6.3 AFM data analysis

AFM scan data consists of a collection of height values arranged in the x and y dimensions in a manner similar to a greyscale image. Several methods were used to extract the required information from this data depending on the circumstances.

Simple height data, such as that used in Chapter 3 was gathered by peak to peak histogram analysis using a Matlab program to read the images and generate the resulting data. Figure 2.22 indicates the principal of this type of analysis where the most frequently occurring height values in an image will tend to form peaks at the high and low ends of the range. The difference between these high and low modal height values was taken as the height value for the entire image and treated as a single measurement in subsequent averaging and analysis.
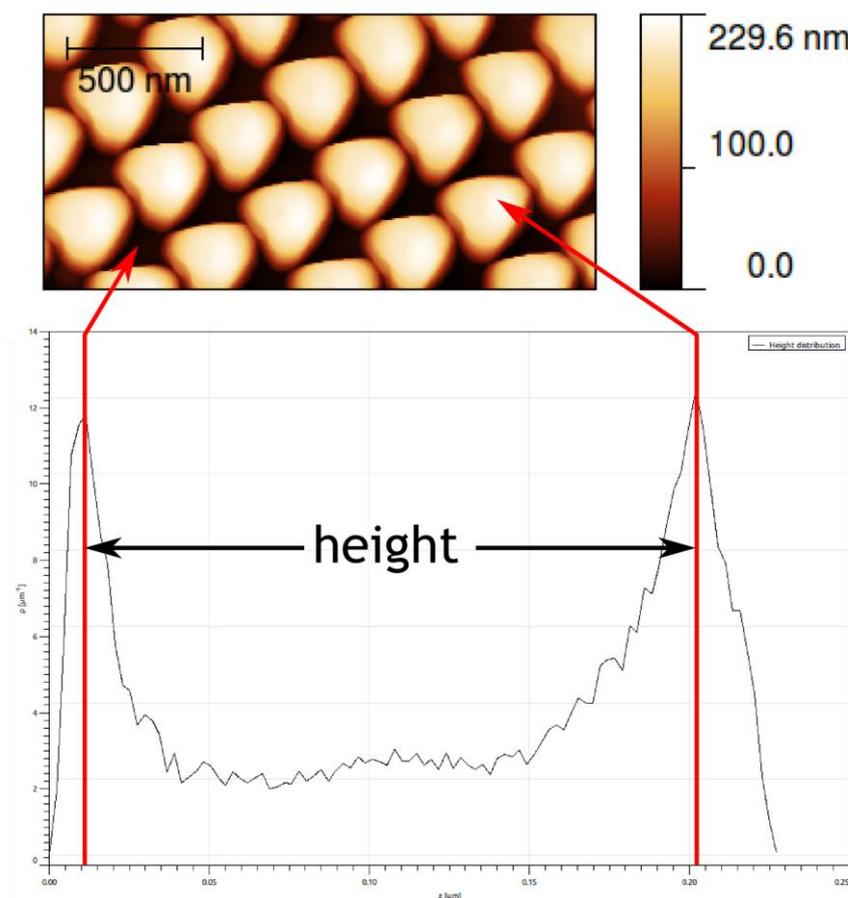
Figure 2.22 - Peak to peak histogram analysis of an AFM scan with arrows indicating that the low and high peaks in the graph correspond to the sample base and feature tops respectively.

Some data, such as that used in Chapter 4 did not generally contain distinct peaks with which to determine the desired height data through the simple histogram analysis described above. In the case of Chapter 4 a more involved process was used that relied upon certain characteristics of the arrangement of features on the samples that were undergoing the analysis. The features on these samples were too tall (1 µm) and close together (<400 nm gap) for an AFM tip to reliably reach the sample base in between them, so the patterns were made with 3, 5 and 10 µm wide gaps within the array of features. This would ensure a large and easily identifiable peak in a histogram analysis as indicated in the top left of Figure 2.23. Unfortunately the high peak was usually more elusive as a result of the AFM tip getting part of the way down between the features and a general variability in feature height. The solution to this was to extract the physical peaks of features within the image

by locating peaks in the trace profile in both x and y directions before performing a logical AND to generate a heat-map like that in Figure 2.23 (right, middle). Histogram analysis on this dataset would yield a distinct modal peak height value from which the low peak could then be subtracted and an overall height value for the image obtained. This process is summarised in bullet points below the corresponding illustration, Figure 2.23.
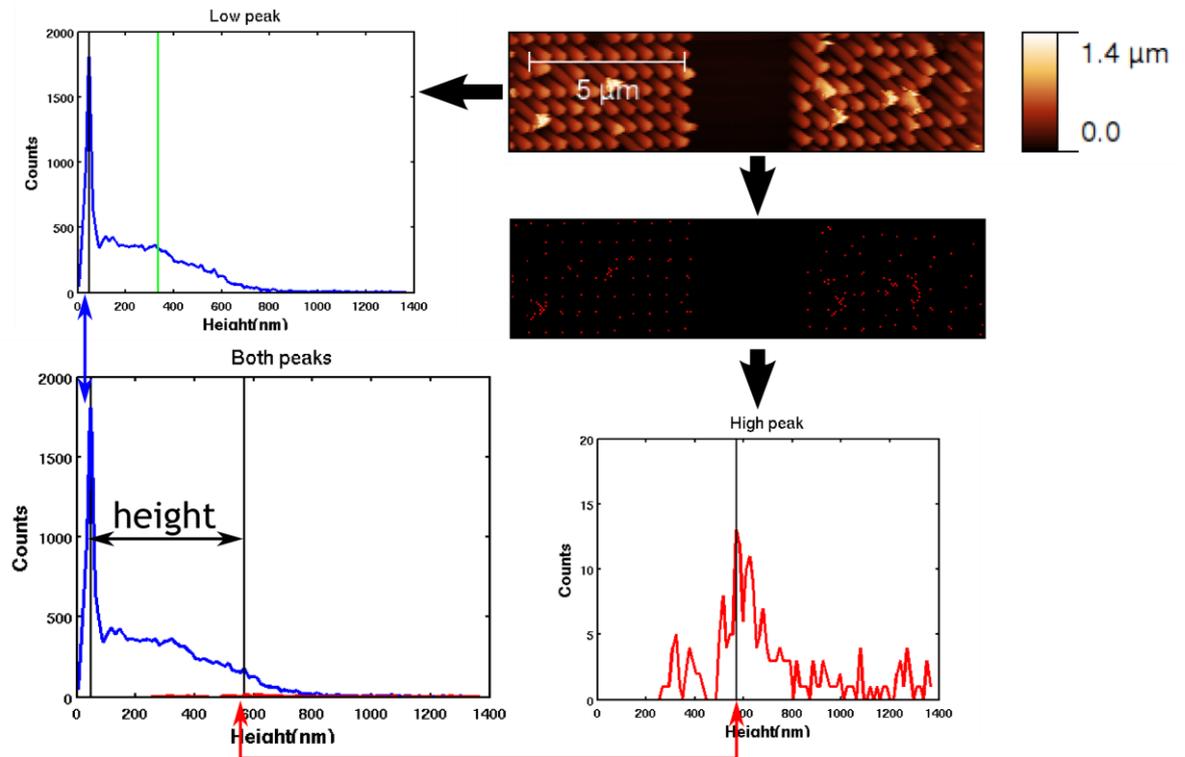
Figure 2.23 - Analysis of feature height by a pattern-specific method involving histogram analysis and peak feature height extraction. Details in text below.

- Obtain low peak by histogram analysis (top left).

- Locate physical peaks in each row and column of the image.

- Perform a logical AND to obtain physical peak heights (mid right).

- Obtain modal peak height value through histogram analysis.

- Subtract low peak value from high peak value.

The AFM scans obtained in Chapter 5 required yet another slightly different method of data extraction. The samples scanned in this experiment all contained linear grating patterns from which both height and periodicity data was required. Sections of the process are shown in Figure 2.24 and the full process summarised beneath it.
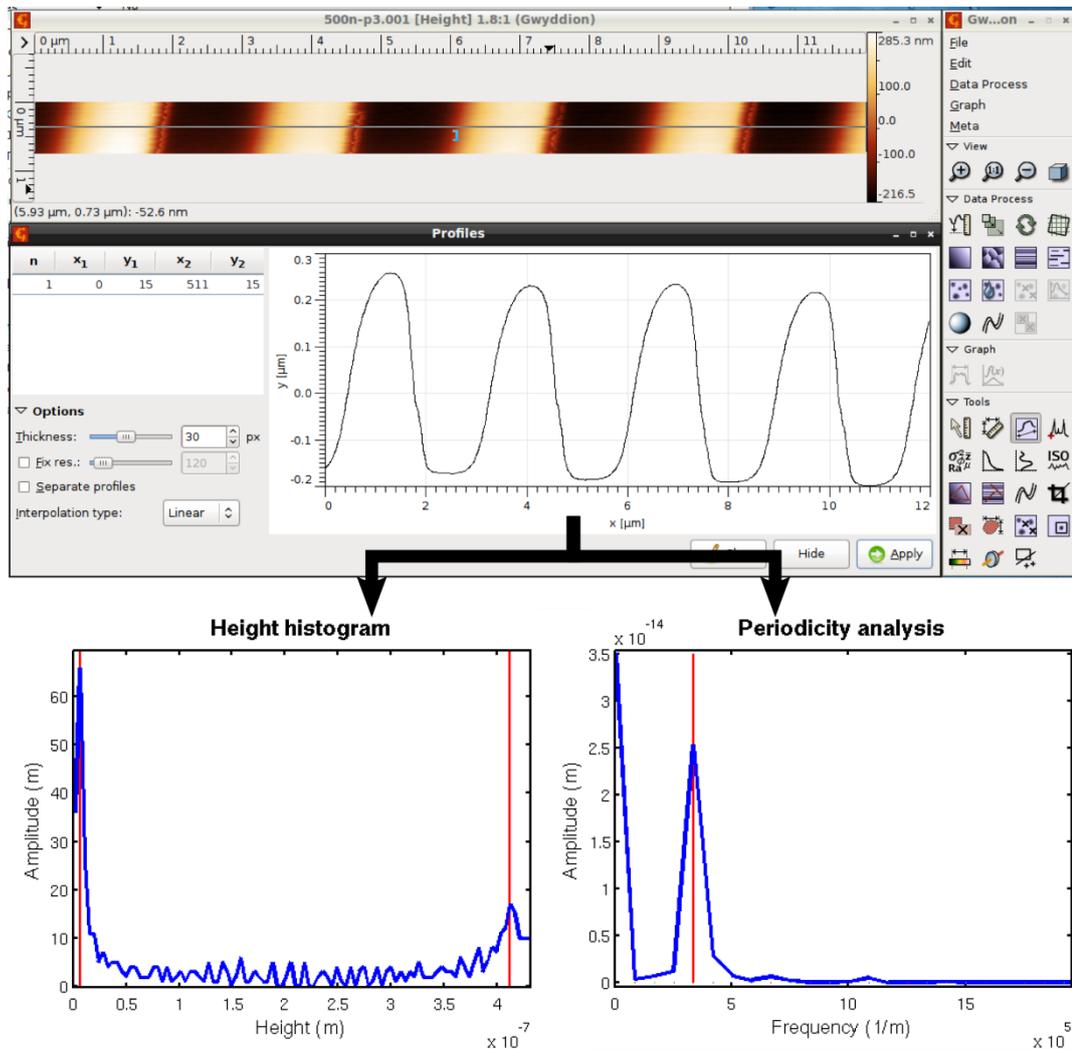
Figure 2.24 - Obtaining height and periodicity data by analysis of AFM profile trace. Details in text below.

- Narrow (aspect ratio 8:1) AFM scans were made on grating samples.

- Scans were flattened in Gwyddion SPM data analysis software (freely available from www.gwyddion.net) and horizontal profiles (averaged in y direction) were exported as comma delimited text.

- Profile traces were analysed in Matlab to obtain height values by peak to peak histogram analysis (described above, Figure 2.24 left) and period values by FFT analysis (Figure 2.24 right).

2.6.4 Figure creation

The majority of graphs were constructed in QtiPlot using data compiled elsewhere and a minority were made in Microsoft Excel and Matlab. Further annotation and formatting as well as all other image preparation was performed using graphical software including GIMP, Inkscape, Adobe Illustator and Adobe PhotoShop.

Chapter 3 Development of hybrid polymer inlays for injection moulding nanostructures

3.1 Outline

3.1.1 Introduction and aims

Injection moulding offers great potential as widely used means to mass produce nanostructured surfaces for many applications including important research into the interactions of living cells with their physical environment.[114] However, as explained in section 1.3.4, the nickel tooling most commonly used for injection moulding nanostructures, is limited in the type of features that it can produce.[71] Without the use of thermally insulating tooling materials or the addition of complicated heating and cooling mechanisms, it is not possible to create raised nanostructures such as pillars because the polymer melt freezes too quickly upon contact with the thermally conductive surface of the mould. The use of thermally insulating tooling materials has delivered success at the micro-[89, 92] and nanoscale,[93] but a tooling solution of this type that takes full advantage of the high throughput production offered by injection moulding for the production of nanostructures is yet to be demonstrated. As such, the potential for heat retardant tooling as a means to replicate raised nanostructures by injection moulding deserves further investigation and is the primary motivation behind the aims of this chapter. These aims are as follows:

- Implement a solution to the problem of incomplete mould filling of raised nanostructures (i.e. pillars) using a heat retardation method as opposed to a variothermal technique. Preferentially, the solution will not add significant complexity to the equipment setup or require significantly greater cycle time to produce replicas.

- Fabricate surfaces containing pillars in the size range of those currently used in cell-nanotopography research (~100 nm).

- Establish a set of materials and processes that can lay the foundation of an enabling technology to mass produce high quality nanopatterned surfaces by injection moulding. New processes should be versatile and adaptable do that they can be further developed enable the replication of different surface patterns such as high aspect ratio nanostructures and multiscale (combined nano/micro/millimetre) surface patterns. They should also be adaptable to different tool configurations, inlay-based or otherwise.

- Fabricate surfaces to be used by biologists tailored to their needs as closely as possible.

- Quantify, analyse and document successes and failures in these pursuits.

3.1.2 Chapter overview

This chapter documents the development of a hybrid polymeric tooling solution which is capable of producing micro- and nanostructures by injection moulding. It covers heat transfer simulations and the use of inlays patterned by both photolithography and nanoimprint lithography (NIL) on polymer films of different thicknesses, as well as the use of multi-layered tooling to create superimposed multiscale structures in the moulded parts. A phenomenon whereby nanopillars are stretched during the moulding process is identified and quantified in terms of injection moulding parameters, and finally an assessment of the long term durability of the new tooling is presented.

3.2 Tooling material

To realise the objectives required two things: a thermally insulating substrate and a platform with which to fabricate nanopatterns using the tools available at the JWNC, both of which had to be thermally stable at temperatures above those of the molten polymers that would be used (polycarbonate (PC), polystyrene (PS) and polypropylene (PP) all have processing temperatures of between 240 and 300°C).

A work by Hansen *et al* [91] pointed to SU-8 photoresist as a suitable candidate for the latter. It cures to form a rigid structure with a high degradation temperature (~380ºC)[115] and low thermal conductivity (0.2 $Wm^{-1}K^{-1}$) which will not reflow within the processing temperature ranges of the polymers mentioned above.[116] In this research it had been photolithographically patterned on nickel substrates which served as effective tooling for the injection moulding of microstructures with cyclic olefin copolymer (COC). Taking this as a cue, it was proposed that SU-8 may be used in a similar way as a platform for nanostructures. Clearly photolithography is not an option for the fabrication of nanostructures and SU-8 is too sensitive to distantly scattered electrons to be patterned by electron beam lithography (EBL), so NIL was proposed as the method by which to nanopattern the tooling. In further contrast to the referenced work, SU-8 3000 Series, rather than the 2000 Series, would be used as it is designed to have superior adhesive properties which would hopefully provide greater resilience and durability in the harsh physical and thermal environment of the injection moulder.

For the substrate, the commercially available polyimide film Kapton ® (DuPont) was an attractive option owing to its reasonable price, thermal durability (T_g > 360°C), low thermal conductivity (0.12 $Wm^{-1}K^{-1}$) and availability in a variety of thicknesses (25 – 127 μm). Kapton finds uses in many industrial applications where reliable performance under demanding conditions is required and according to the manufacture's website, "has been used successfully in applications at

temperatures as low as -269°C…and as high as 400°C.". The material was also available in a thicker (740 µm), and therefore more rigid, format under the brand name Cirlex ® (Katco UK). Experimentation was performed with two thicknesses of Kapton film and with Cirlex, the latter eventually emerging as the main substrate of choice for most of this project.

3.3 Simulations

Computer simulations were used to model the thermal flux of the polymer melt in the presence of both hybrid and nickel inlays. The physical dimensions of the simulation models are closely based on those of the actual tool and inlays that were used and are shown schematically in Figure 3.1. The initial temperature of the PC was set to 280°C with both inlay types set to 80°C. All boundaries (i.e. the tool) set and held at 80°C throughout.
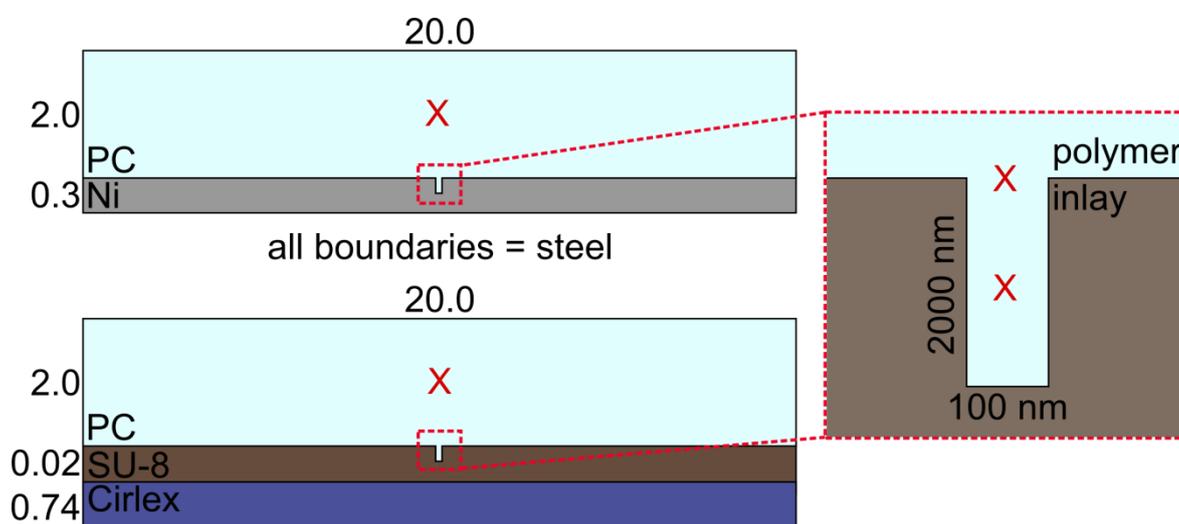
Figure 3.1 - Schematic diagram of thermal simulation models for PC with Ni (top) and hybrid (bottom) inlays. Crosses mark locations of temperature probes. All dimensions in mm unless otherwise indicated.

This model was used to track the change in temperature from the initial conditions at three locations over a period of 20 s, thus simulating the cooling of the polymer after injection. The three locations, marked with crosses in Figure 3.1, are located at the centre of the bulk part (1 mm from the inlay surface), at the base of a 100 nm wide feature in the inlay (on the line of the polymer-inlay interface) and 1µm into this 2µm deep feature. Figure 3.2 contains plots from these simulations which highlight two important comparisons between the two inlay types.
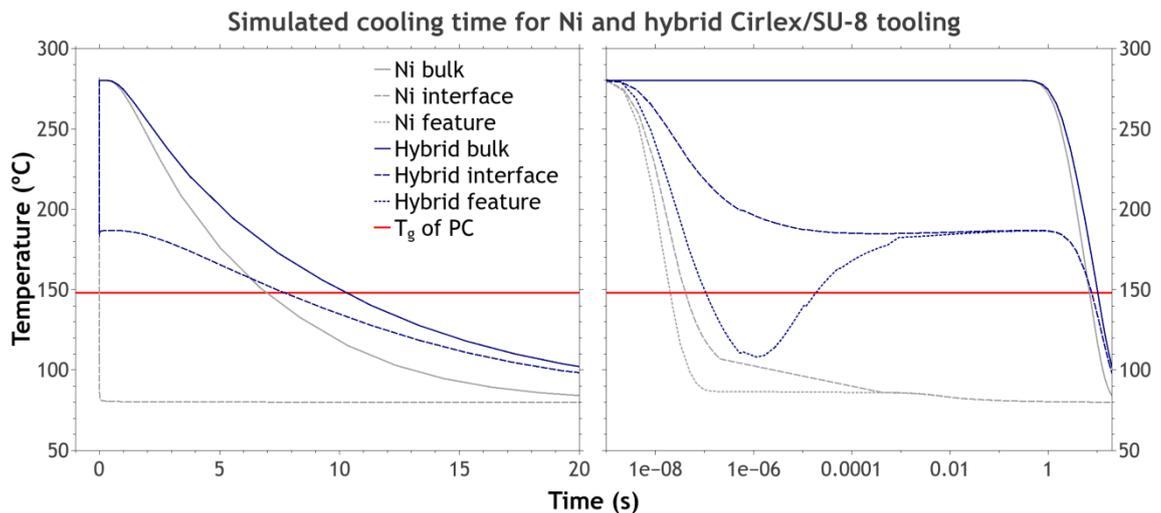
Figure 3.2 - Simulation results showing the time it takes for PC to cool from T_m to T_w at three locations for two types of tooling.

The long-dashed grey and blue lines show plots of the temperature of the injected polymer at a location at a base of a pillar-creating cavity at the mould/melt interface over a period of 20 s after injection, with nickel and Cirlex/SU-8 inlays, respectively. It shows that when a hybrid inlay is used the polymer stays above its glass transition temperature (T_g) for around 8 s which gives it a better chance of filling the holes before freezing compared to the nickel inlay which results in almost instantaneous cooling to the tool temperature. The solid grey and blue lines show plots of the same polymer cooling scenario, except that the temperature measurements are taken at the core of the mould cavity. At this location there is much less of a difference between the two inlay types, indicating that the overall moulding timescale is not adversely extended when using hybrid inlays. A third pair of traces is provided on the logarithmic plot on the right which shows the temperature change at a point half way down a 2 μm deep feature with 100 nm width. In this case the nickel inlay again results in immediate freezing while the hybrid inlay allows the polymer, after a brief dip below T_g, to return to a temperature well above that whereupon it follows a similar trend to the melt at the feature's base. This dip may be an artefact of the simulation, but if it does reflect reality then it should not significantly inhibit filling as it returns to the molten state within period of injection and long before the holding pressure phase is complete.

3.4 Results and discussion

3.4.1 Inlays patterned by photolithography

Having taken the cue from Hansen *et al* [91] to use SU-8 as a tooling material, Cirlex and Kapton samples were patterned by photolithography and used as inlays for injection moulding with PP and PC. As can be seen from Figure 3.3 and Figure 3.4, this type of tooling proved to be effective,

providing accurate inverted replicas of the photolithographically defined structure, even for the high aspect ratio pillars in Figure 3.4 (aspect ratio ≈ 7.5:1).
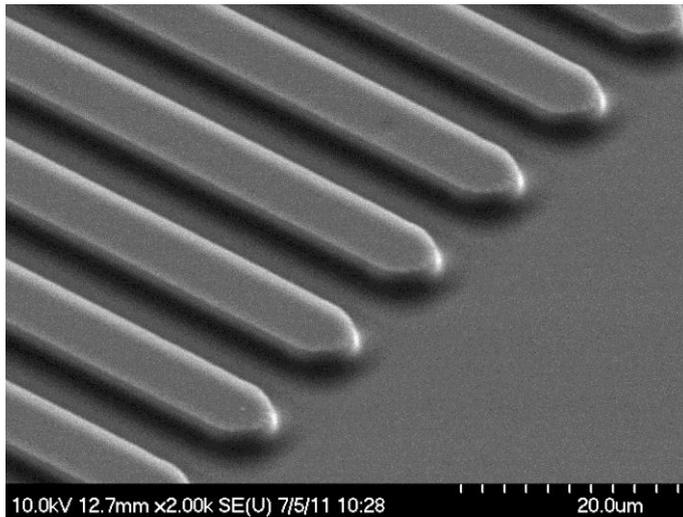
Figure 3.3 - PC micrograting made by injection moulding with an inlay comprising photolithographically patterned SU-8 on a Cirlex substrate
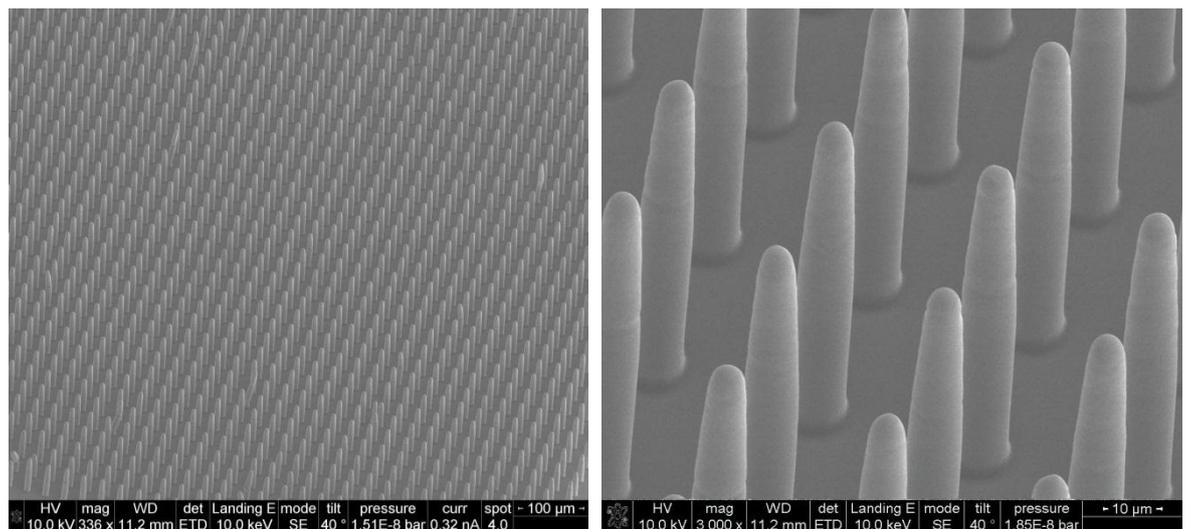
Figure 3.4 - Large area and close up SEM images of 10 μm diameter (of base) pillars injection moulded in PP using an inlay made from photolithographically patterned SU-8 on a Cirlex substrate. The tapering diameter is due limitations of the photolithography process.

From these results it was clear that the injection moulding process used in conjunction with these tooling materials is quite capable of producing even rather adventurous structures at micrometre length scales, but the resolution limit of photolithography would prevent the production of structures much laterally smaller than these. To move to the submicron range another method, such as nanoimprint lithography (NIL) would have to be employed.

3.4.2 Inlays patterned by NIL

Inlays were patterned by UV-NIL on Cirlex and Kapton (25 µm and 127 µm thick) substrates using all variants of the pocket imprinters (see section 2.3.3, page 47), but over time it became apparent that Cirlex substrates were the easiest to work with owning to their less flexible nature and thus tended to produce the best imprints. Being the thickest of the three, Cirlex also offered the most effective heat retardation capabilities which would aid the formation of difficult nanostructures, in this case a 1 cm square array of 120 nm diameter pillars on a 300 nm pitch measuring 120 - 130 nm in height. The quartz stamp for UV-NIL was patterned by EBL (on-the-fly dots, 250 µCcm^{-2}), NiCr lift-off (20 nm) and dry etch (CHF$_3$/Ar, 3 minutes) as detailed in Chapter 2, section 2.4. A study was undertaken to explore the performance of Cirlex/SU-8 hybrid inlays over a range of parametric conditions (see Table 3.1) and to compare their performance with that of similarly patterned nickel inlays. This work resulted in a journal article published in 2012.[117]

T_t (°C)	T_w (°C)	v_i (cm^{3}s^{-1})	t_c (s)
260	60	10	2 – 20
280	80	23	for T_t = 280 & T_w = 80
300	100	37	
for all T_w and v_i		50	3.5 – 20
(up to 310 for T_w=80)	for all T_t and v_i	for all T_w and T_t	for T_t = 300 & T_w = 80

Table 3.1 - Parameter space for initial nanopatterned hybrid inlay tests.

As was expected from the simulations discussed above, the hybrid inlays showed far superior replication of nanopillars than nickel inlays. Figure 3.5 shows cross sections of moulded parts produced with a hybrid and nickel inlay (plus inverted cross-sections of the inlays themselves) using the following process parameters: melt temperature (T_m) = 280°C, tool temperature (T_w) = 80°C, cooling time (t_c) = 5 s and injection speed (v_i) = 50 cm^{3}s^{-1}. The nickel inlay produced parts with features of little more than 30 nm height, despite the inlay having holes of 100 nm depth. Pillars produced by hybrid inlays with the same process conditions were actually taller than the depth of the inlay holes (i.e. stretched), a phenomenon which has previously been observed with NIL.[118] Despite the fact that physical differences between the nickel and hybrid inlays do not offer an explicitly direct comparison; it is clear that nickel inlays are not capable of achieving anything close to what is required.
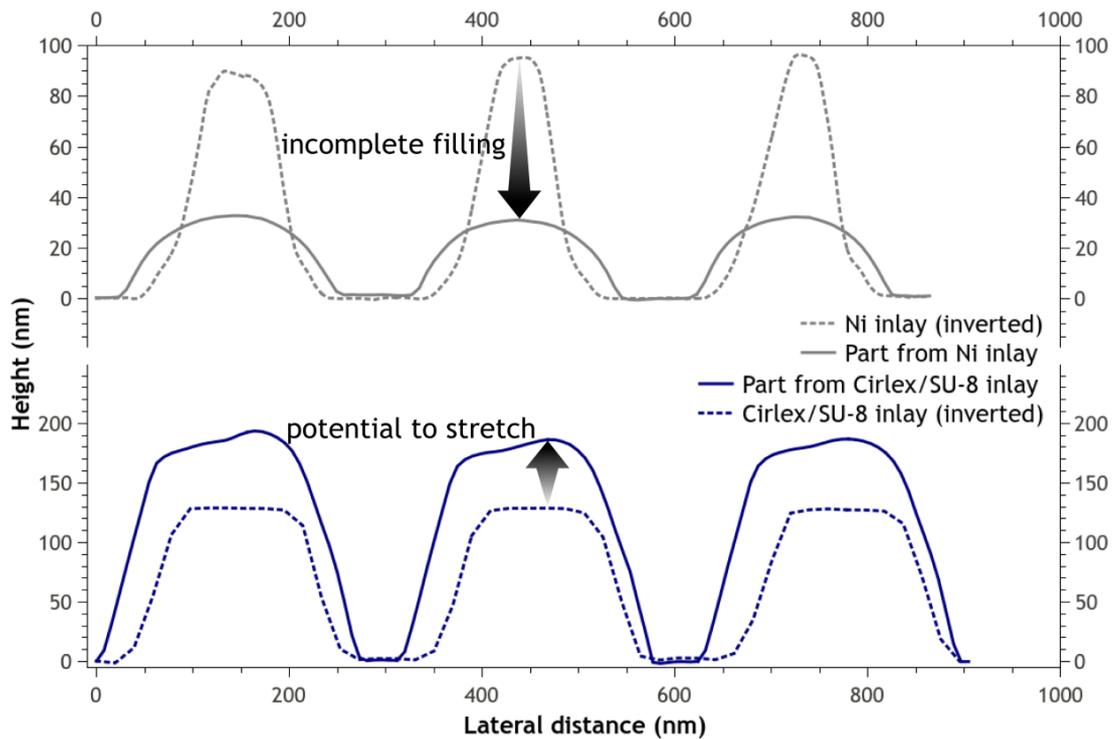
Figure 3.5 - Typical profiles, measured by AFM, comparing injection moulded PC parts with the nickel (top) and hybrid (bottom) inlays they were made with.

In addition to the AFM traces of Figure 3.5, the shape of pillars captured from tilted SEM imaging (right of Figure 3.6) also suggested that an element of stretching had occurred during the injection moulding process, most likely during demoulding when the melt near the interface could still be above T_g. This unexpected effect is similar to, but less extreme than, the intentional stretching of injection moulded microscale pillars by Michaeli *et al*[119] and the *nanodrawing* technique sometimes employed in embossing processes.[120]
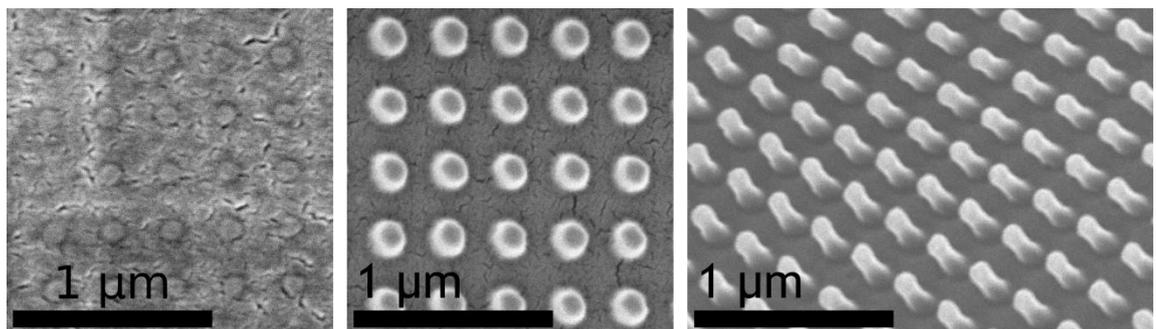
Figure 3.6 - SEM images of PC parts made with (left) nickel inlays and hybrid inlays showing (middle) typical appearance of nanopillars from above and (right) visibly stretched nanopillars on a slope viewed at 45° tilt.

The effects of several parameters on this stretching phenomenon were investigated. Variation in cooling time has been shown to be important for the production of microstructures by injection moulding[107, 121] and so was examined here. Figure 3.7 shows normalised pillar heights

obtained in injection moulded polycarbonate (PC) with different cooling times and the following constant parameters: $T_w = 80°C$, $v_i = 50$ cm^{3}s^{-1}, $T_m = 280°C$ (blue) or $300°C$ (red). The solid lines show the results of the 1st experiment and the dotted lines show those of a 2nd experiment performed to assess the repeatability of the results.
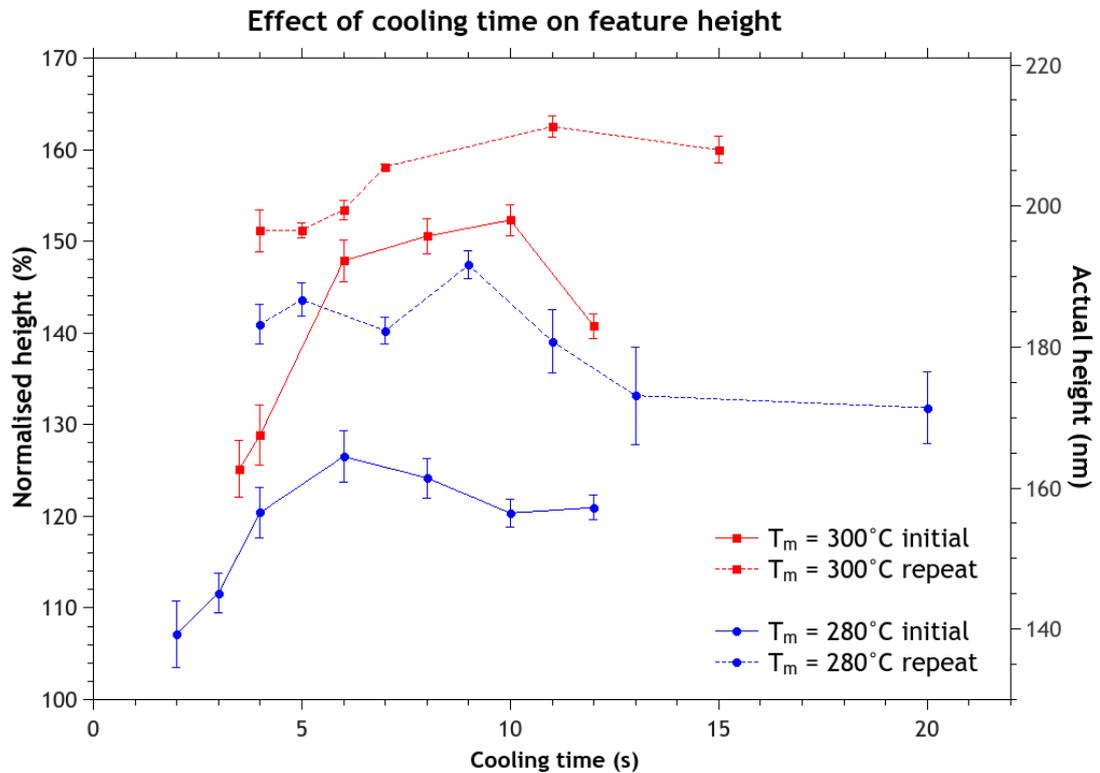
Figure 3.7 – Effect of cooling time at two melt temperatures on two separate occasions. $T_w = 80\,°C$ for both.

The discrepancies between the initial tests and the repeats are clear, suggesting that t_c is not a reliable parameter to be used as a means to control moulded pillar height. Despite this the general trends are quite consistent with all traces are relatively flat above around 6 s and showing a decrease in height below that, albeit a more marked decrease in the 1st set of results. At cooling times less than those recorded on the graph the parts were too soft to be ejected properly, being bent by the ejector pin rather than forced out due to the bulk of the part being too warm. This is in general agreement with the simulations described in section 3.3. The results shown in Figure 3.7 highlight an inherent variability in the results for which any stage of the fabrication process could be responsible. Indeed, EBL, metal lift-off, dry etch and NIL, as well as the injection moulding process, all have the capacity for minor variations so the cumulative effect of these and the characterisation process (in which only two 2 x 1 µm locations on each of two moulded parts were scanned by AFM) would likely have contributed to the observed discrepancies.

Shifting the attention to injection speed, the flat nature of the plots in Figure 3.8 shows that it had little influence on the amount of filling and stretching that occurred (with the exception of a

positive correlation at $T_w = 60°C$ $T_m = 300°C$ and a negative gradient at $T_w = 100°C$ $T_m = 300°C$, albeit with a missing data point), but the relative positions of these traces indicate that both melt and tool temperatures play a pivotal role.
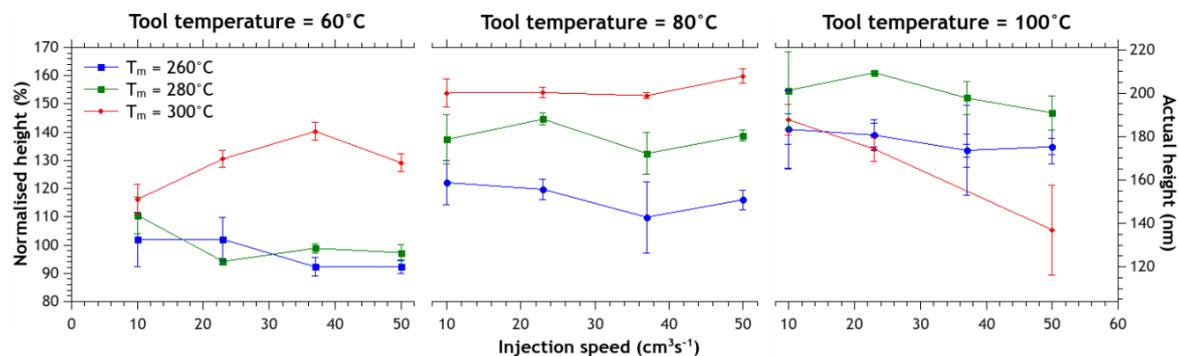
Figure 3.8 - The effect of injection speed on pillar height at different melt and tool temperatures.
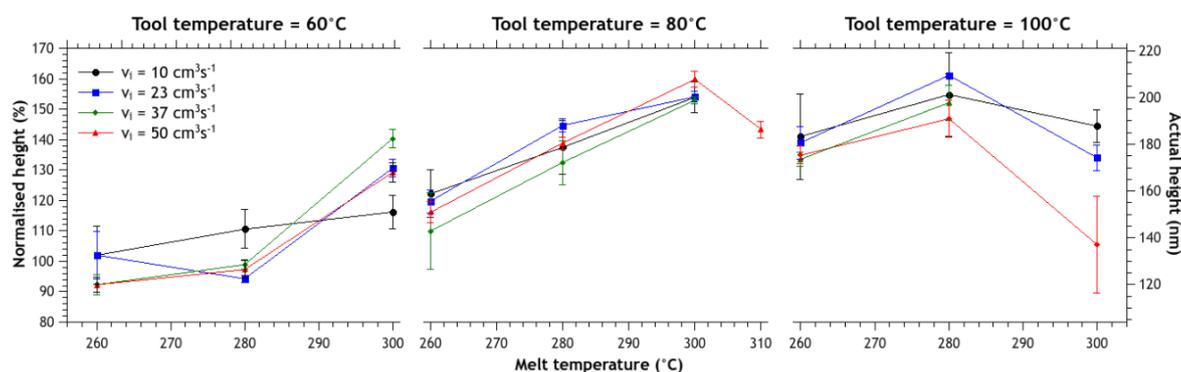
Figure 3.9 - The effect of melt temperature on pillar height at different tool temperatures and injection speeds.

The effect is traced in terms of melt temperature in Figure 3.9 where we see a clear positive correlation when the $T_w = 80°C$ and slightly less so at $T_w = 60°C$. Looking at both sets of plots together, we see the clearest effects of parameter change around $T_w = 80°C$ and $T_m = 280°C$, which is the optimal temperature combination when using PC with conventional tooling, and a less clear relationship with a greater margin for variation at the fringes of these recommended process conditions.

Having obtained an impression of the importance of melt and tool temperature on the stretching of nanopillars, a series of repetitions were performed to further elucidate the effects of these parameters. By focussing on tool temperature in the range 40 - 90°C at only two melt temperatures, 260°C and 280°C, the graph in Figure 3.10 was produced which indicates a profound relationship between tool temperature and pillar height which are similar except for a fairly constant shift at the two melt temperatures. Quantitatively, T_w can affect pillar height by around

40% for T_m of 260 and 280°C for this particular inlay depth (130 nm). The relatively small standard error bars indicate that this phenomenon is highly repeatable and that pillar stretching can be tuned to meet a desired height, with the 280°C plot indicating a maximal stretching limit at this melt temperature (Figure 3.8 and Figure 3.9 indicate that 60% stretching is possible at T_m = 300°C, but this was not tested any further). While optimal conditions for accurate replication and part quality with nickel inlays are T_m = 280°C and T_w = 80°C it seems that hybrid inlays seem to give the most accurate replication (not stretched) when T_m = 260°C and T_w ≈ 65°C.

Effect of tool temperature on feature height
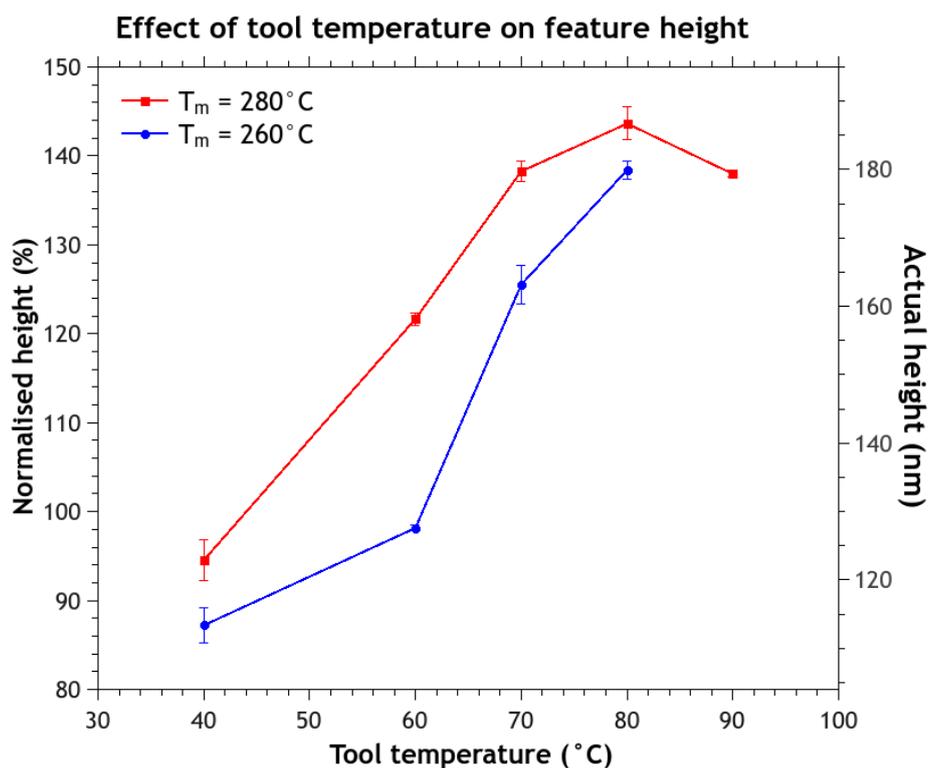
Figure 3.10 - Plots of Tw versus pillar height for T_m = 260 and 280 °C.

3.4.3 Multi scale patterning with hybrid inlays – dimples and sandwiches

Cells have been shown to respond to surface topographies in different ways at different length scales [4] with both micro and nanoscale features playing a role in influencing their behaviour.[122] With this and other potential applications in mind, it was thought that the flexible nature of Kapton might allow it to be manipulated to conform to an underlying structure and that such a multi-layered approach might allow nanostructures to be superimposed upon a microstructured background. By inserting a thin, flexible nanopatterned inlay (e.g. 25 μm Kapton) into the frame on top of larger scale features (e.g. holes drilled in the back plate or a separate micropatterned inlay) it might be possible to create a moulded part with both a nanotopography and

a micrometre or millimetre scale subtopography. This principal is illustrated schematically in Figure 3.11.

Using the configuration illustrated in the upper half of Figure 3.11, an array of 100 nm diameter pillars and a 500 nm grating (see Figure 3.12) were successfully superimposed onto a 2 mm dome. Nanopillars were also successfully superimposed upon a microscale grating (see Figure 3.13) using the multilayer sandwich approach, but as can be seen from Figure 3.14 this also highlighted some possible limitations of the process.
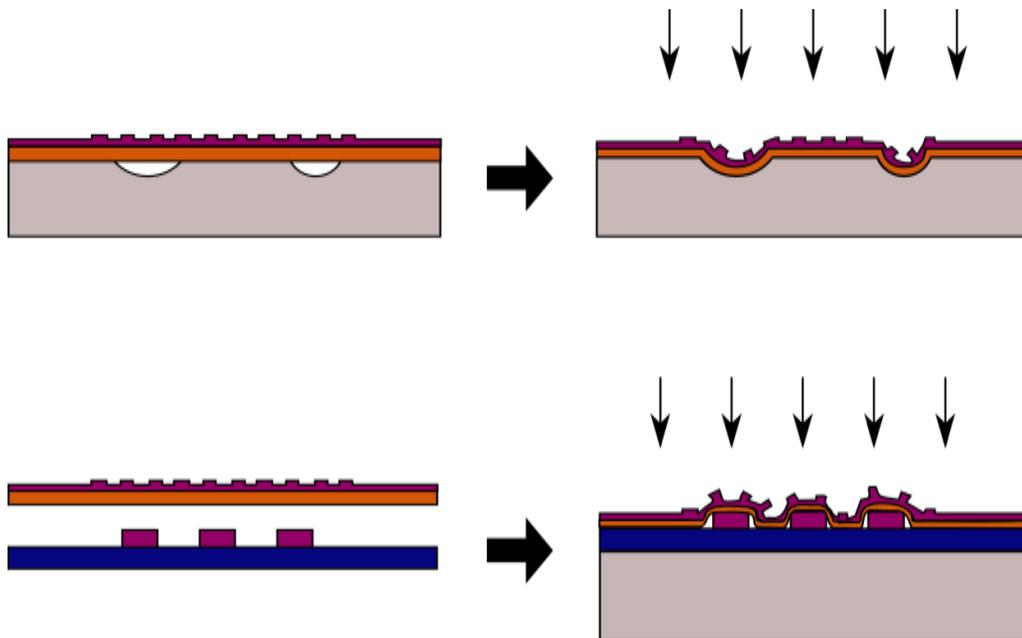
Figure 3.11 - Schematic illustrations of a nanopatterned Kapton/SU-8 inlay conforming under pressure (thin vertical arrows) to the shape of an underlying subtopography patterned (above) by drilling into the backplate and (below) by SU-8 photolithography on Cirlex substrate.
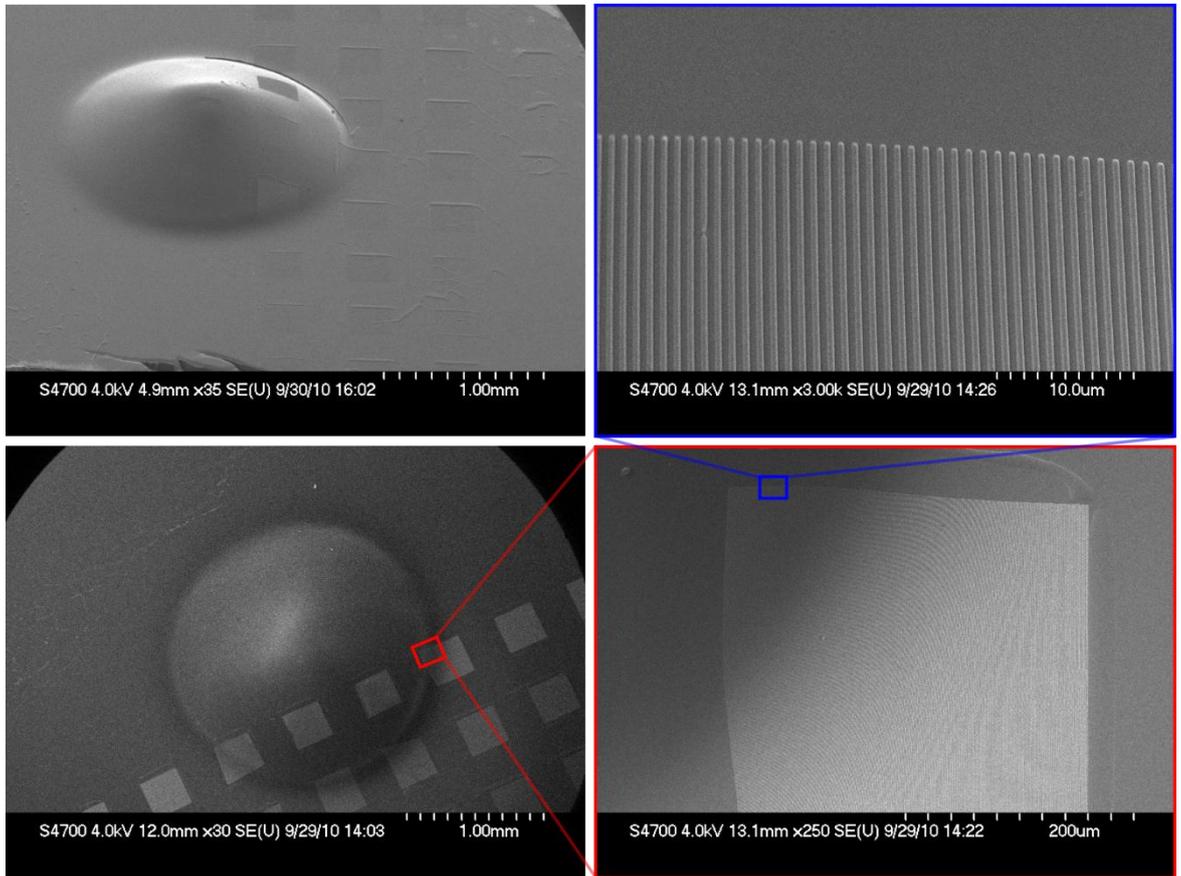
Figure 3.12 - 500 nm grating superimposed on a 2 mm dome made in PP.
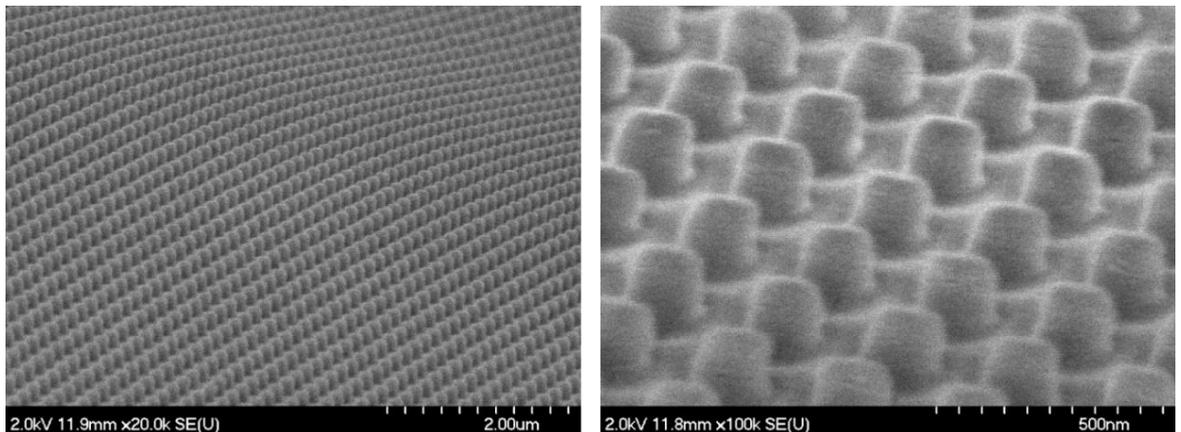
Figure 3.13 - PC nanopillars rounding the crest of a hill defined by a subtopography.

Figure 3.14 shows that the nanopattern on the top layer can be significantly deformed by the injection moulding process. This seems to only occur in the grooves (corresponding to ridges on the inlay) and could be explained by the fact that the localised pressure over these small areas must be significantly higher than in recessed regions during the injection and holding pressure phases. The inverted traces of moulded parts with the corresponding subtopographies from the inlays in Figure 3.14 (top left) and Figure 3.15 indicate the amount of deformation to which the top layer

inlays were subjected. These traces show that the thinner 25 μm Kapton (right) conformed much more closely to the subtopography compared to the 127 μm Kapton (left).
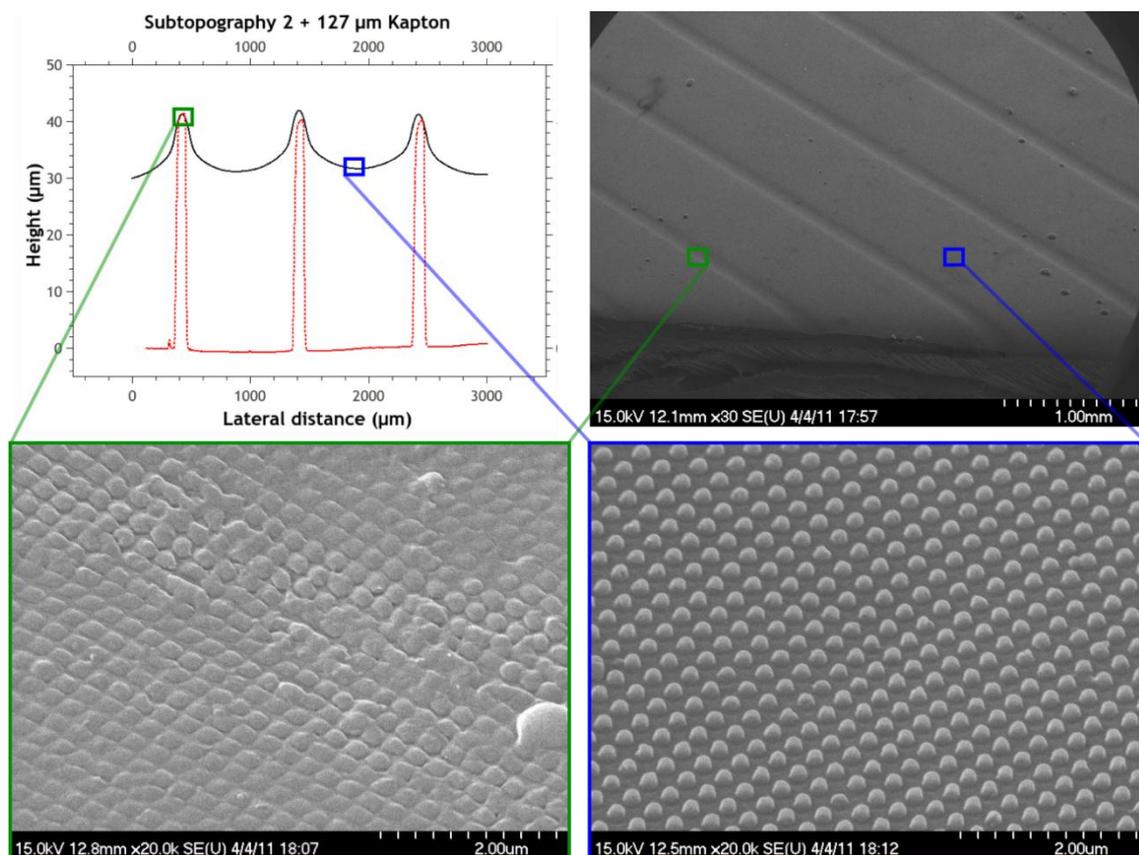
Figure 3.14 - Inverted profile trace (black line) of PC part formed by a nanopatterned Kapton/SU-8 inlay on top of a subtopography grating (red line). The SEM images correspond to locations on this trace as indicated.
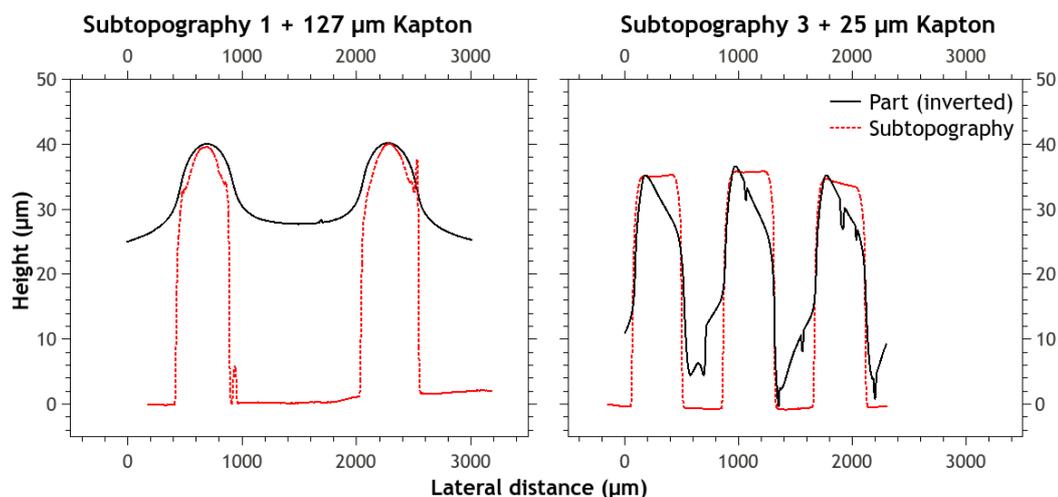
Figure 3.15 - Inverted profile traces of parts formed by nanopatterned Kapton/SU-8 inlays on subtopography gratings.

Attempts were made to use 25 μm inlays atop other subtopography patterns, such as round pillars, but in most cases the Kapton was ripped within the 1st or 2nd shot. Given that the thickness of the top layer of any inlay sandwich imposes a limit on the ultimate minimum lateral resolution and sharpness of the underlying micropattern, and that the 25 μm Kapton was not strong enough to withstand multiple moulder cycles, it would appear that achieving high quality sub 100 μm patterns superimposed with nanopatterns is probably not possible with this material and this method. A thinner, stronger material would be required and even then the nanopattern damage shown in Figure 3.14 could still be an issue.

3.5 Inlay Durability

A single nanopatterned hybrid inlay with continuous SU-8 up to the sample edge (as made with pocket imprinter version 1.0 or 3.0 – see section 2.3.3) has been used to make more than 2000 replicas with no measurable sign of wear and tear to its surface or physical integrity, but those with the SU-8 developed off at the edges to facilitate a neater fit in the frame (as made using pocket imprinter version 3.1) displayed a small amount of peeling around this periphery after prolonged use as illustrated in Figure 3.16.
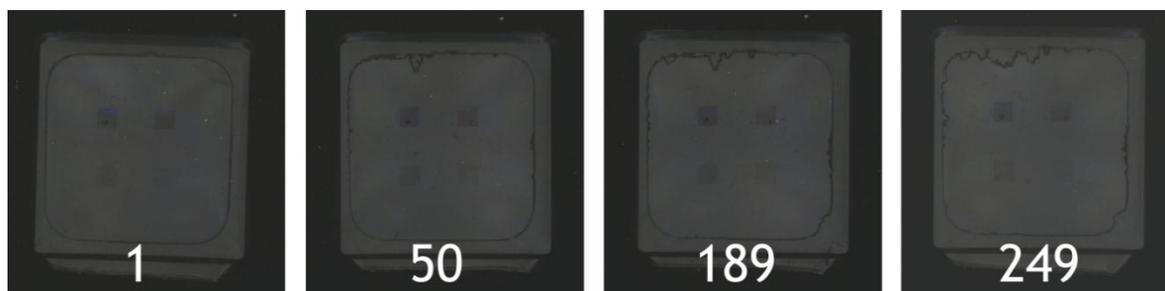
Figure 3.16 – 1st, 50th, 189th and 249th parts from a continuous moulding session which show inlay wear over time.

Furthermore, AFM measurements show a small decrease in the depth of features on the inlay over time and in some instances with this type of tooling, a visible build up of polymer has occasionally been observed on the surfaces of inlays. Figure 3.17 shows how inlay depth drops very quickly before settling into a fairly constant negative gradient of less than 1.0 nm per shot. After cleaning with N-methyl-2-pyrrolidone (NMP), average feature depth returned to its original value which suggests that the depth reduction is due to a build-up of polymer residue at the base of the nanopits in the hybrid inlay. To combat this polymer build-up it was proposed that the addition of non-adhesive coatings to the tooling surface may be able to alleviate the situation as it has been shown to improve the performance of imprinting and embossing processes.[95] This proposal and a push towards higher aspect ratio structures set the stage for the next section of the investigation.
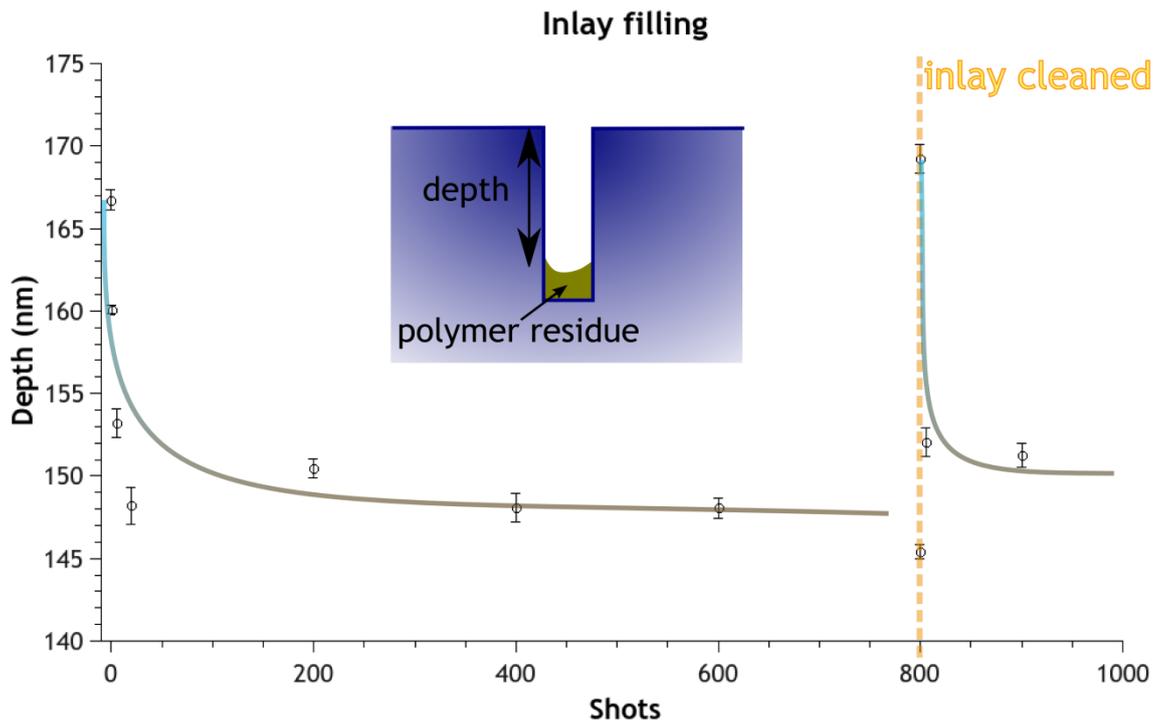
Figure 3.17 – Plot showing the variation in depth of a Cirlex/SU-8 hybrid inlay as injection moulded replicas are produced when $T_m = 260°C$ and $T_w = 65°C$. After 800 shots the inlay was cleaned and the process restarted with $T_w = 80°C$.

3.6 Conclusions

In this chapter a hybrid polymeric tooling solution has been developed which comprises PI inlays patterned with SU-8 photoresist that can succeed where traditional nickel tooling fails in the large volume production of nanoscale pillars with diameters of the order of 100 nm by injection moulding. This is achieved by a simple method of slowing the heat transfer from melt to tooling to allow the polymer time to fill the mould before freezing and does not require any adaptations to injection moulding equipment.

This is an enabling solution for injection moulding as a technique for the production of such structures, making it an attractive alternative to the relatively slow disciplines of embossing and NIL. This process retains the advantages of speed (cycle time was around 17 s, but no attempt was made to optimise this) and reproducibility which are characteristic of injection moulding and offers a relatively simple inlay patterning process that is useful for both prototyping and full scale production.

This hybrid tooling is suitably durable over ~1000 cycles (but may benefit from non-adhesive coatings – addressed in the next chapter) and its potential for patterning is limited only by what can be fabricated on a master stamp. Furthermore, it offers a simple means of 3D patterning with

concurrent micro and nano scale structures using the inlay sandwich technique which, despite showing some limitations, shows promise and could well be enhanced by the use of alternative materials.

Samples have been fabricated in large numbers and passed on to biologists who continue to use them to explore the interactions between cells and their physical environment for aplications in regenerative medicine. The samples are of a suitable size, shape and material to be used with existing tissue culture labware and processes.

A stretching effect has been identified and quantified whereby the height of nanopillars can be tuned from around 90% to 140% of designed height simply by varying the tool temperature. This could prove to be very useful for the production of high aspect ratio structures where the durability of pillars on imprint stamps may limit the heights to which they can be made. Indeed it is high aspect ratio structures and inlay surface coatings which are the focus of the next chapter of this thesis.

Chapter 4 Development of a method to fabricate high aspect ratio nanostructures by injection moulding using non adhesive coatings

4.1 Outline

4.1.1 High aspect ratio nanostructures

Many potential applications of nanostructured surfaces require structures which have aspect ratios (ratio between height and width) that exceed those normally required for general nanofabrication processes such as electronic devices where the thickness each layer of a device tends to be substantially less than its lateral dimensions.[123] Because of this, high aspect ratio (HAR) structures may be considered somewhat of a niche speciality and not a significant driver for the development of micro- and nanofabrication technologies. There are, of course, a few notable exceptions such as SU-8 photoresist which can be used to fabricate microstructures with aspect ratios of 40:1 by photolithography and 100:1 by X-ray lithography.[124]

Despite the fact that it is often technically challenging to build something much taller than it is wide, there are many examples of HAR nanostructures in the literature focused on the pursuit of various applications. Bioinspired non-reflective,[2] superhydrophobic[14] and dry adhesive[20] surfaces all require nanostructures with aspect ratios greater than 1:1. There are also several applications in cell biology research[125] including some which are of particular interest to this project which involve culturing cells on arrays of high aspect ratio pillars.[126, 127] In these publications cells were cultured on elastomeric PDMS micropillars of different heights to both modulate the effective substrate rigidity and provide a way to measure the contractile forces exerted by cells (see Figure 4.1). The manipulation of substrate stiffness has been shown to direct the lineage commitment of stem cells [27] and the magnitude of the forces exerted by cells can be a predictor of this.[127] As such, this type of investigation can offer valuable insight that may benefit the advancement of regenerative medicine.
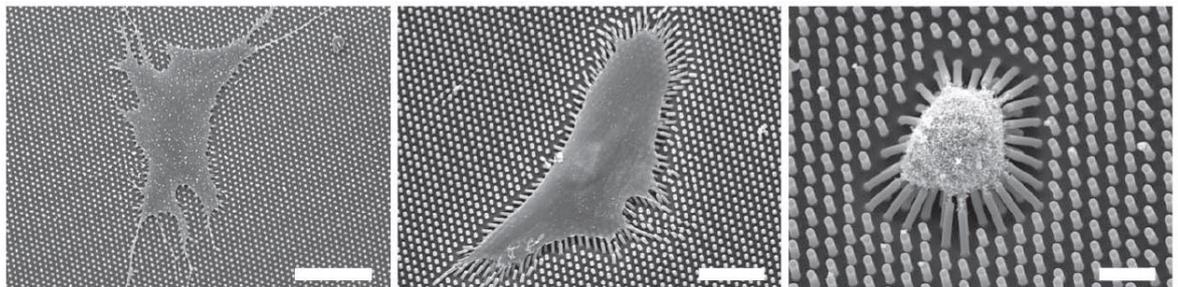
Figure 4.1 - SEM images of human mesenchymal stem cells on PDMS pillars with height (left to right) 0.97, 6.10 and 12.9 μm. Pillar diameter ~2 μm , centre-to-centre spacing = 4 μm. Scale bars = (left to right) 50 μm, 30 μm and 10 μm. Image taken from [127].

The process of PDMS casting can take several hours which is currently a limiting factor in this type of work. If the substrate material can be changed to a thermoplastic polymer then injection moulding, which can replicate samples in a matter of seconds, has the potential to enable the up-scaling of the production of this type of experimental substrate enormously. The next chapter focuses on the replication of this type of microstructure using thermoplastic elastomers which have similar mechanical properties to the PDMS (Young's modulus = 2.5 MPa), but this chapter concerns attempts to provide a nanoscale alternative (diameter ~100 nm) using the amorphous thermoplastic poly(carbonate) (PC). The nanoscale approach has the potential to be advantageous because the smaller structures may be packed more closely together and so provide a surface that could appear more planar from the cell's perspective whilst still providing an effective way to simulate substrate stiffness via the bending of nanopillars. It is also feasible that nanotopographical patterns known to initiate certain effects on cells (e.g. disordered 120 nm features on a 300 nm pitch)[36] could be incorporated into the positioning of these pillars.

The force required to bend a cylindrical pillar with a fixed base of known height L, diameter D, and Young's modulus E by a distance δ is given by the formula:[127]

$$F = \frac{3\pi}{64} E \frac{D^4}{L^3} \delta$$

As can be seen from this equation, the force required to bend a pillar by a fixed distance is heavily dependent on the relationship between the diameter D and the height L; i.e. the higher the aspect ratio, the greater the contribution by the L^3 term and the smaller the force required to bend the pillar. The nature of this relationship between force and the extent of pillar bending provides a practical reason why, if one wishes to replicate these structures in PC, the pillar size must move from the microscale to nanoscale. The Young's modulus of the PC Makrolon OD2015 is 2.35 GPa while that of the PDMS used to form the micropillars is 2.5 MPa; three orders of magnitude lower. In order to retain a force of the same order of magnitude, this 10^3 increase in the Young's modulus E in the equation above must be counteracted by the other variables. In order for the value δ to remain measurable by optical microscopy it cannot be reduced by much more than one order of magnitude (the maximum bending in Figure 4.1 is around 10 µm) to stay within the size range of optical microscopy as defined by the Rayleigh criteria (see Chapter 2, section 2.5.1); around 400-500 nm for a good microscope. The only other way to reduce the size of the required force is to minimise the $\frac{D^4}{L^3}$ term. The arithmetic below indicates that this necessitates a move of both diameter and height to the nanoscale in order to counteract the 10^3 increase in E.

$$\frac{D(micro)^4}{L(micro)^3} = \frac{(10^{-6})^4}{(10^{-6})^3} = 10^{-6}$$

$$\frac{D(nano)^4}{L(nano)^3} = \frac{(10^{-9})^4}{(10^{-9})^3} = 10^{-9}$$

Specifically, Fu *et al*.[127] calculated that the cells they used exerted forces of around 20 nN on PDMS micropillars. Figure 4.2 shows what L would be required for a range of pillar diameters D to keep the force F required to bend a PC nanopillar at 20 nN for a fixed bending distance $\delta = 500$ nm.
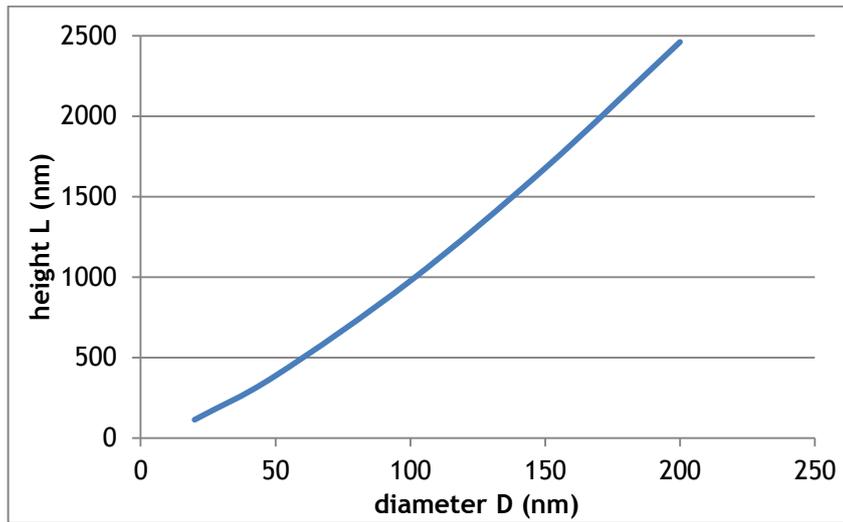
Figure 4.2 - Height required to for a given diameter to allow a PC nanopillar to bend by 500 nm under a force of 20 nN.

Figure 4.2 indicates that for nanopillars with diameters comparable to those successfully produced in the previous chapter (~ 120 nm) would be required to have a height of about 1200 nm to achieve the desired bending (aspect ratio 10:1).

4.1.2 Non-adhesive surface coatings

As discussed in the introduction chapter, the use of non-adhesive coatings is common in replication based fabrication to enhance the filling of micro- and nanoscale features and reduce the likelihood of damage as mould and replica are separated. A summary of coatings previously used in embossing/NIL techniques and injection moulding is provided in Table 4.1 (reprinted from Chapter 1, section 1.3.5 for convenience).

Surface coating	Stamp / tooling material	Method	Replica material	Performance
Fluorosilanes (FS)	Si / SiO$_2$	T-NIL / UV-NIL / embossing.	Various thermoplastics and curing polymers	Widely regarded as effective non-adhesive coating in replication based fabrication.[52, 100, 101]
(NiO,TiO)+FS	Ni	NIL	PMMA	Not as effective as SiO$_2$+FS.[95]
FS	SU-8	NIL	PMMA, PDMS	High quality replication of multilayer microstructures [104]
FS	PI	T-NIL / UV-NIL / embossing.	Thermoplastic and UV curing polymers.	Faithful replication on 4 inch wafer.[102]
Nitrided fluorocarbon	SiO$_2$	NIL	PMMA	Enhanced durability over non nitrided fluorocarbons.[105]
FS	Si	Injection moulding (IM)	TPU	Protected tooling and enhanced filling of micropillars.[107]
FS	Ni	IM	COC	Made it possible to fill sub 100 nm pillars.[108]
FS, MoN, WN	Ni	IM	PC, PMP	Prevented polymer build-up over 1500 cycles.[109]
CrN, TiN	Steel	IM	Polyamide with glass fibre	Lower wear to tooling than with traditional methods (heat treatment, Cr deposition, nitriding).[110]
Al,Ti	polymer	IM	PS, PC	Improved PS filling of microstructures over polymerbackplate+SiO$_2$+F.[89, 90] Al peeling after 1000 cycles.[87]
Au	Ni	IM	PMMA	Resistant to residue.[86]

Table 4.1 - Summary of non-adhesive coatings used in NIL/embossing and injection moulding. Reprinted from Chapter 1.

4.1.3 Aims of this chapter

The aims of the work documented in this chapter are:

- Further extend the tooling solution established in the previous chapter to replicate high aspect ratio PC nanopillars by injection moulding with a target aspect ratio of 10:1 for pillars with diameters of ~100 nm.

- Push the lower boundaries of lateral feature size that are attainable for HAR nanopillars.

- Extend the new tooling solution to utilise non-adhesive inlay surface coatings to facilitate and/or enhance the realisation of the first two aims.

- Establish which inlay surface coatings were the most effective in terms of replication fidelity, durability and capability to produce HAR nanopillars.

- Establish if non-adhesive inlay surface coatings would mitigate the stretching of nanopillars observed in the previous chapter.

- To realise functional surfaces that could be used in the study of cell-substrate interactions such as those used to modulate substrate rigidity and measure the forces exerted by cells as described above. Consider also other applications such as non-reflective, superhydrophobic or non-adhesive surfaces.

- Quantify, analyse and document successes and failures in these pursuits.

4.1.4 Chapter overview

The bulk of this chapter is concerned with a systematic study into the effects of various inlay surface coatings on the replication of HAR nanopillars by injection moulding using the tooling solution developed in the previous chapter. It begins by describing the fabrication of stamps containing HAR nanopillars and issues that had to be overcome to transfer these patterns to inlays by UV-NIL. The choice of surface coatings and considerations that influenced pattern design are discussed before initial results of attempts to fabricate HAR nanopillars without these coatings is presented. Following this is an assessment of coating durability.

Due to the quantity of data gathered, the results of the systematic study are prefaced by a guide to their interpretation. The results themselves are followed by an analytical discussion, after which two smaller datasets are examined which give further insight into the effects of temperature and feature dimensions. Before concluding, a brief study into the effectiveness of using non-adhesive coatings to mitigate the stretching of low aspect ratio pillars is described.

4.2 Results and discussion

4.2.1 Fabrication of stamps

Quartz stamps were fabricated by EBL, metal lift-off and dry etch using the processes described in Chapter 2, section 2.4. All etch times were 27-30 minutes giving depths of within 100 nm of 1 µm. Results of work with several stamps will be presented in this chapter, but they can be separated into two categories, those that were successful for NIL and those which were not. Details of the fabrication parameters for both are presented in Table 4.2.

	PMMA 2010 thickness (nm)	PMMA 2041 thickness (nm)	Pattern	E-beam dose (µC/cm^2)	NiCr hard mask thickness (nm)
Successful stamps	185	125	100 nm dots, 500 nm pitch	165	100
			150 nm dots, 500 nm pitch	300	
			120 nm dots, 210 nm pitch	280	
Unsuccessful stamps	None - single layer	300	100 nm dots, 500 nm pitch	170	120
			100 nm dots, 2500 nm pitch	280	

Table 4.2 - Chapter specific process parameters.

The reason for the inclusion of unsuccessful stamps is to highlight issues encountered when translating the established UV-NIL process to the high aspect ratios required by the aims of this chapter. These difficulties can arise at the demoulding stage of NIL and are thought to be caused by the increased frictional force associated with the greater total surface area of features with greater height. During initial attempts to emboss SU-8 with HAR quartz stamps it was found that a large proportion of nanopillars would break away from the bulk quartz and become embedded in the SU-8 after the imprint was complete. These pillars had been dry etched with the JWNC's standard quartz etch (CHF$_3$/Ar) and a NiCr etch mask 120 nm thick; a value calculated to be able to withstand the ~ 1 µm quartz etch. It did indeed survive the etch and the end result was a beautiful array of cylindrical pillars (Figure 4.3, left bottom). Unfortunately this straight-edged shape is unsuitable for NIL because large frictional forces build up on these sidewalls as stamp and replica

are separated and lead to pillar breakage such as that experienced in these initial attempts. In order to minimise the possibility of breakage, a slightly positively sloped pillar geometry (~5°) is required so that there is less persistent contact with the material from which the stamp is being demoulded leading to lower frictional forces and less stress on the pillar (Figure 4.3, right bottom).

Unsuccessful | **Successful**

metal deposition

NiCr
PMMA 2041
PMMA 2010
quartz

post lift-off

125nm 170nm
100nm

post etch profile

NiCr removed

105nm
120nm

100nm
170nm

NIL demoulding

SU-8

friction
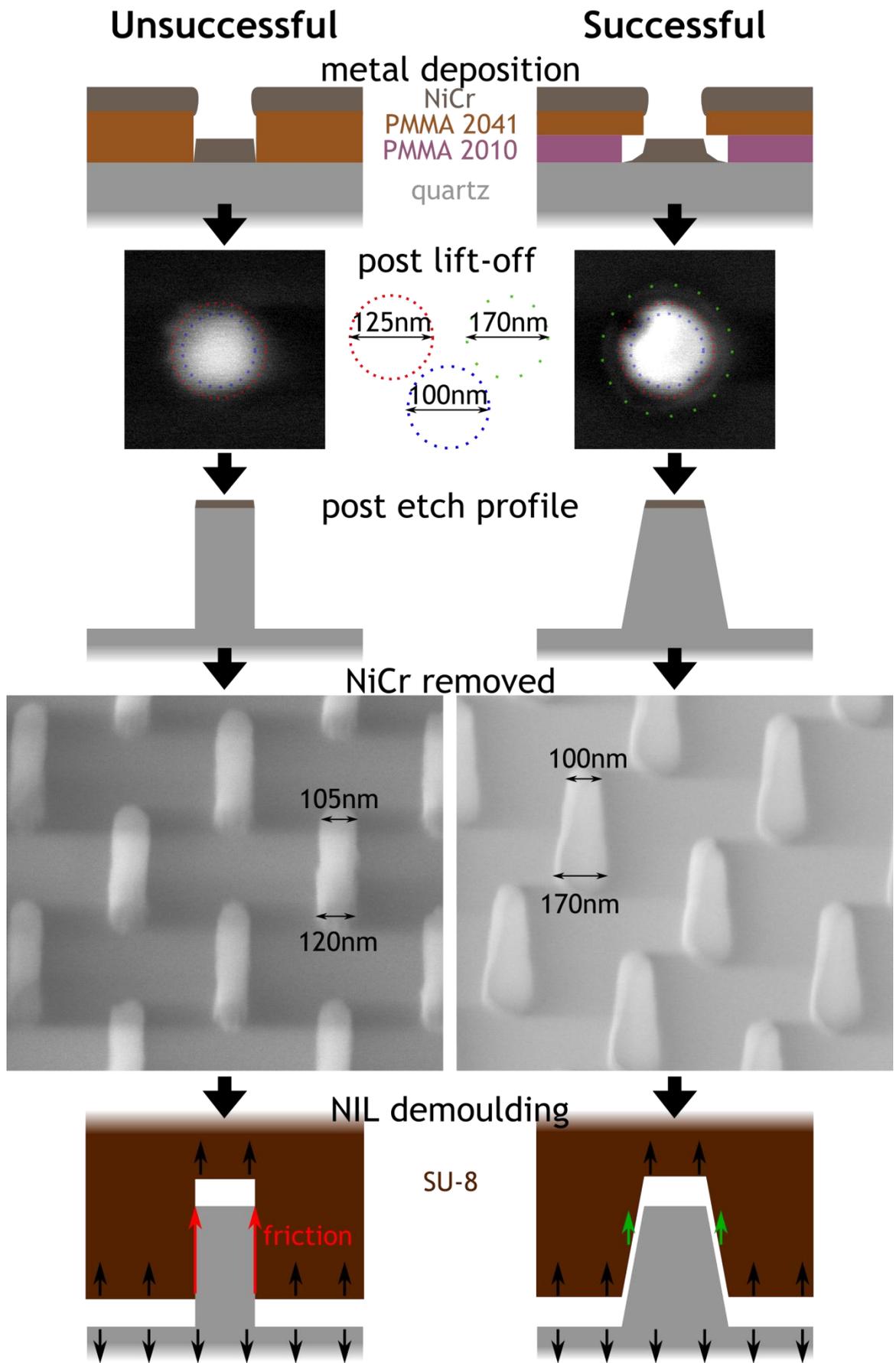
Figure 4.3 - Key steps in stamp fabrication and subsequent NIL processes for successful and unsuccessful stamps. The figure illustrates the importance of a favourable etch profile during stamp separation and how to achieve it.

The key to obtaining such a conical pillar profile lies in the details of the dry etch process and the thickness and shape of the NiCr etch mask. The standard quartz etch recipe used in the JWNC is designed to be anisotropic and will therefore result in a cylindrical profile if the etch mask is not compromised. In order to obtain a conical profile, the etch mask needs to be such that a small amount of over etching is allowed to occur around the periphery of the circular feature where the metal layer is thinner, as illustrated in Figure 4.3. It is thought that the use of an undercut bilayer of resist provides a space for some of the metal deposited to spread out a little as shown in the enhanced contrast SEM images of the post lift-off stage in Figure 4.3 (the overhang is achieved by using a lower molecular weight resist on the bottom layer which forms slightly wider features than the top layer during development). This spreading results in an extended thin periphery, indicated by the green dotted circle and not visible for the unsuccessful stamp, that measures about 170 nm across which is the same width as the pillar base. Although the quality of the high contrast SEMs may not be high enough to be entirely certain of this, it does explain both the sloped sidewall and the broadened base of the pillars on the successful stamp.

Aside from the different type of resist layers, there was one other key difference between the successful and unsuccessful processes. The unsuccessful stamps had 120 nm NiCr hard masks while the successful ones only had 100 nm. This difference may also be related to the different profiles, but it does not explain how an anisotropic etch would lead to the broadened base of the successful stamps' pillars. Whatever the reason may be, the successful process was consistent in delivering conical pillars with a slope angle of ca. 5° from vertical (Figure 4.3, bottom right).

4.2.2 Choice of surface coatings

In light of the beneficial effect of surface coatings reported in the literature for injection moulding and other replication based fabrication techniques such as NIL,[95] ten different surface coatings were chosen as candidates for testing. Some coating choices were based on successes reported in the literature. These are briefly summarised in Table 4.3.

Coating material(s)	Reason
SiO_2 + TPFS	Ubiquitous in NIL[51, 103] and successful stamp material in this project.
Si_3N_4 + TPFS	Improved durability over SiO_2 + a fluorosilane.[105]
Ni + TPFS	Enhanced replication of 40 nm diameter COC pillars compared to Ni alone.
Ti	Improved filling of microstructures compared to SiO_2 + a fluorosilane and Al.[89]
TPFS only	Improved release of embossed PMMA with fluorinated SU-8 stamp.[104]

Table 4.3 - Inlay surface coating choices based on success in the literature.

Additionally, unfluorinated nickel was added to the list due to its widely accepted use as standard injection moulder tooling and uncoated inlays were included as a control. In order to thoroughly asses the effects of fluorosilane layers on replication performance, the blank spaces were filled in by making the further inclusions of untreated SiO_2, Si_3N_4 and fluorinated titanium. The full list of inlay coatings tested in this study are listed in Table 4.4.

Uncoated
TPFS only
Si_3N_4
Si_3N_4 + TPFS
SiO_2
SiO_2 + TPFS
Ni
Ni + TPFS
Ti
Ti + TPFS

Table 4.4 - List of inlay surface coatings tested in the study documented in this chapter.

4.2.3 Fabrication of inlays

Inlays containing HAR nanopits were fabricated by UV-NIL using the method detailed in the methods chapter section 2.3.3 during which   Coatings were applied to the inlays using the methods indicated in Table 4.5 which are detailed in sections 2.3.4 and 2.3.5.

Coating	Thickness (nm)	Method of deposition
Si_3N_4	10	ICP deposition
SiO_2	10-15	PECVD
Ni	10-12	Electron beam evaporation
Ti	10-12	Electron beam evaporation
TPFS	monolayer	Vapour deposition

Table 4.5 - Deposition thicknesses and methods used to deposit inlay surface coatings.

4.2.4 Design of patterned areas

The design of nanopillars arrays needed to take into account the means by which they would be characterised. In order to measure pillar height in a manner similar to the previous chapter, it would be necessary for an AFM tip to fit between them and make sufficient contact with both the floor of the nanostructured surface and the tops of the pillars so that a clear histogram of the frequency of different height values could be established as in the height analysis process in Chapter 3. One possible way to achieve this would be to position pillars relatively far apart, by a distance of around twice their height. This method, however, resulted in a pillar breakage rate of close to 100% during NIL for 100 nm diameter 1 µm tall pillars on a 2.5 µm pitch. This may be due to the lower pillar density causing each pillar to be subjected to a greater proportion of the lateral forces from the flow of the resist than is the case at higher densities. In support of this hypothesis were observations from some stamps which contained pillars of 120 nm diameter on a 210 nm pitch which did not exhibit any sign of large scale failure after multiple imprints.

The final design for the stamp which produced the bulk of the results in this chapter consisted of 1x1 mm arrays of 100 nm diameter pillars with a pitch of 500 nm. Within these arrays, gaps in the pillar field were designed which measured 3, 5 and 10 µm in width to allow the AFM tip plenty of space to obtain a reliable base height value. This approached served the task well, but it was clearly evident that these gaps, as well as the pattern edges and internal defects, tended to act as

sites from which pillar failure would originate, likely for the same reason as the 2.5 μm pitch pillar failure mentioned in the previous paragraph. As Figure 4.4 shows, over the course of the ten imprints the growth of damaged areas increased to a level where the stamp was not far from being unfit for purpose, but thankfully sufficient pillars survived at the gap edges to permit successful completion of the measurements.
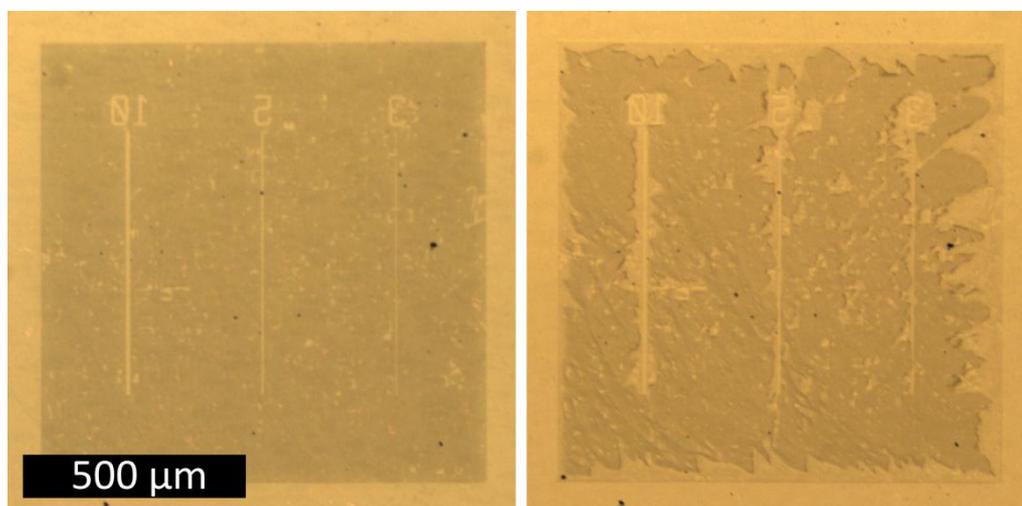
Figure 4.4 - Optical micrographs of the same area from the first (left) and tenth (right) inlays fabricated by UV-NIL using the same stamp. Degradation of pattern is a result of pillar breakage on the stamp. Text indicates the width of gaps in pillar arrays.

In addition to assessing the height of injection moulded nanopillars it was also desirable to assess the proportion of pillars successfully replicated. As well as this, preliminary investigations had shown that injection moulded nanopillars had a tendency to deviate from the ideal vertical orientation by leaning to one side or through the clumping together of their tips, so some means to quantify this would also be useful. To achieve these two goals, SEM images from a top-down viewpoint were captured and analysed as described in Section 2.6.2 to obtain values for success rate (i.e. the number of successfully fabricated pillars compared to what would ideally be present in the image capture area) and circularity, a metric expressed as a value between 0 and 1 which gave an indication of how straight pillars were. The formula used to calculate circularity is given below.[128]

$$circularity = 4\pi \frac{area}{perimeter^2}$$

If the shape is a perfect circle the circularity will be equal to 1 because:

$$4\pi \frac{area}{perimeter^2} = 4\pi \frac{\pi r^2}{(2\pi r)^2} = 4\pi \frac{\pi r^2}{4\pi^2 r^2} = 1$$

A further reason for choosing a pillar-to-pillar pitch of 500 nm was to make it possible to locate them by optical microscopy. As explained in Chapter 2 section 2.5.1, the 100 nm pillars themselves would not be resolvable due to the resolution limit imposed by the wavelength of visible light, however the 500 nm gap between them would be resolvable which would make it possible to study the adhesion dynamics of cells adhered to them without the need for electron microscopy.

4.2.5 Replication of nanopillars without surface coatings

The first attempts to replicate HAR nanopillars were made without the addition of surface coatings. Some results obtained from these attempts with PC (Figure 4.5) and PS (Figure 4.6) are shown below. With PC pillars with diameters of around 150 nm were consistently well replicated, but those with diameters of 100 nm and below did not. As shown by the SEM image in Figure 4.5 (right) structures either did not fill or were broken off except in cases where four adjacent pillars seemed to coalesce, resulting in a wider, highly stretched pillar. This pillar joining was most likely present due to bending/breakage of pillars on the stamp during the fabrication of inlays by UV-NIL.
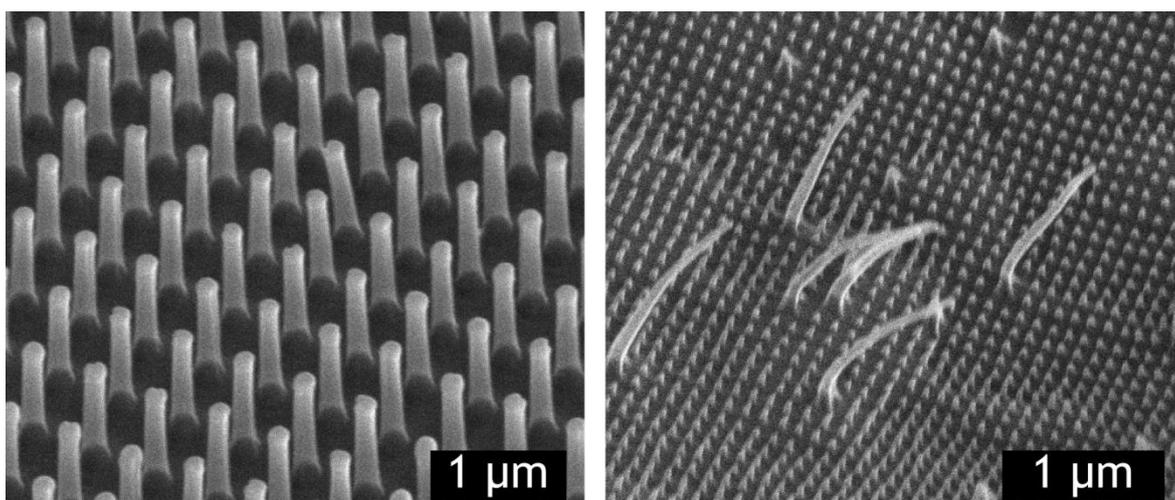
Figure 4.5 - Injection moulded HAR PC nanopillars without surface coatings. Left: 140 nm pillars replicate well. Right: Sub 60 nm pillars do not form except when combined and stretched. T_m=260ºC, T_w=80˚C.

In contrast to the results for PC, replication with PS produced inconsistent results for all nanopillars sizes (Figure 4.6). What is common to both, however, is that the pillars have a clearly defined tip which exceeds the width of main bulk of the pillar. This was also observed with the results from coated inlays and is discussed during the analysis of those results below.
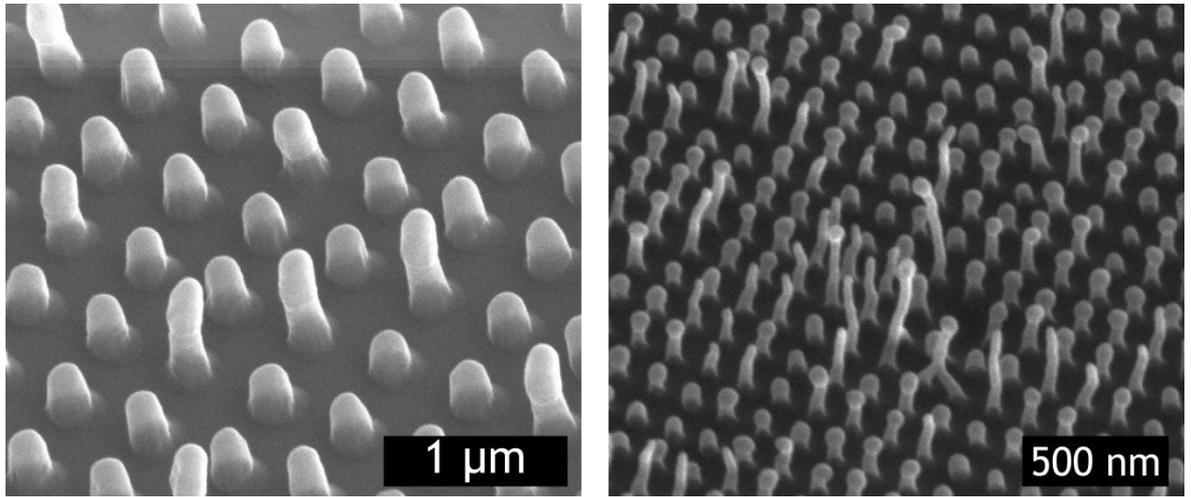
Figure 4.6 - Injection moulding attempts at HAR PS nanopillars. Inconsistant filling is common to larger (200 nm diameter, left) and smaller (60-70 nm diameter, right) features. T_m=260˚C, T_w=50ºC.

4.2.6 Durability of inlay coatings

To obtain a measure of the durability of the inlay surface coatings two types of measurement were made before and after injection moulding: water contact angle (WCA) using the sessile drop method and X-ray photon spectroscopy (XPS). WCA is related to the surface energy where a higher value corresponds to greater hydrophobicity and generally indicative of good stamp-replica release properties in replication based fabrication processes. For this metric a bar graph is provided in Figure 4.7 showing mean static droplet WCA on unpatterned regions of pristine Cirlex/SU-8 inlays and after 16 cycles for ten different inlay coatings (including uncoated) and 100 cycles for 3 different inlay coatings. These two data sets are the results of separate experiments with different inlays, but are shown together for comparison. An important reason to include the 100 cycle data is because 16 is a very low number for a mass production technique and for this type of tooling to be worth using for large volume production it would need to endure hundreds, if not thousands, of cycles. However, for most experimental purposes, 100 cycles was thought to be representative for continuous use as 1000 cycles was not achievable within the timeframe of this study. By comparing the two it is possible to shed some light in the immediacy of any observed change in surface characteristics and hypothesise how these characteristics may pan out over a longer production run.
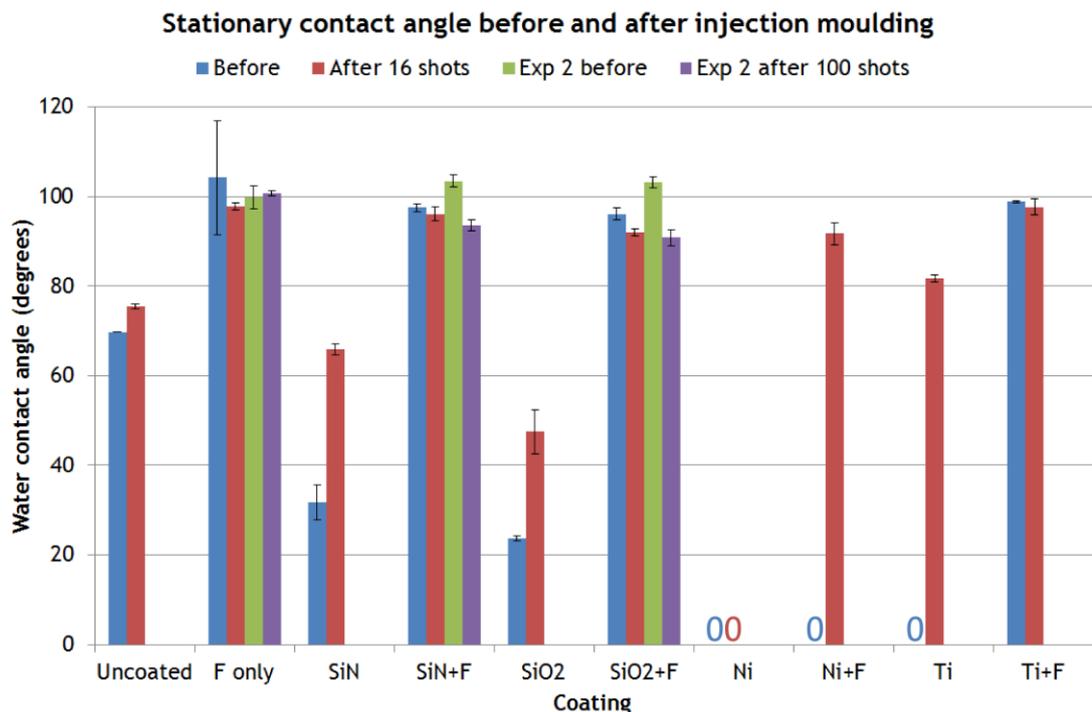
Figure 4.7 - Static water contact angle for ten (experiment 1) and three (experiment 2) inlay surface coatings before and after injection moulding. Zeros are provided to indicate that the drop formed a WCA so low that it was not possible to measure. TPFS is further abbreviated to F to save space.

For fluorinated coatings (with the exception of nickel) we see small or insignificant changes over 16 shots and relatively small (~10°) changes over 100 shots for fluorinated nitride and oxide with no significant change to the TPFS-only surface. This indicates that these surfaces are likely to

yield high quality nanopillar replication compared to other coatings which, despite showing WCA increases, retain lower absolute values. Notable exceptions to this are the fluorinated nickel coating and titanium coating which exhibit drastic change that may be the result of an accumulation of PC residue during the injection moulding process, potentially indicative of the type of inlay filling associated with traditional nickel tooling.

To accompany the stationary WCA, measurements of the advancing and receding contact angles were also made. The difference between these angles is known as contact angle hysteresis (CAH) and is a measure of the stability of wetting states, with a lower value being preferable for replication based processing. Characteristic of these results (Figure 4.8) is a greater degree of variability as well as some inconsistencies between the two experiments and some contradictory implications to those suggested by the stationary WCA data. However, on the whole the results are encouraging given that most CAH values decrease or remain the same, except in the case of the non-fluorinated metal coatings which continue to buck the trend.
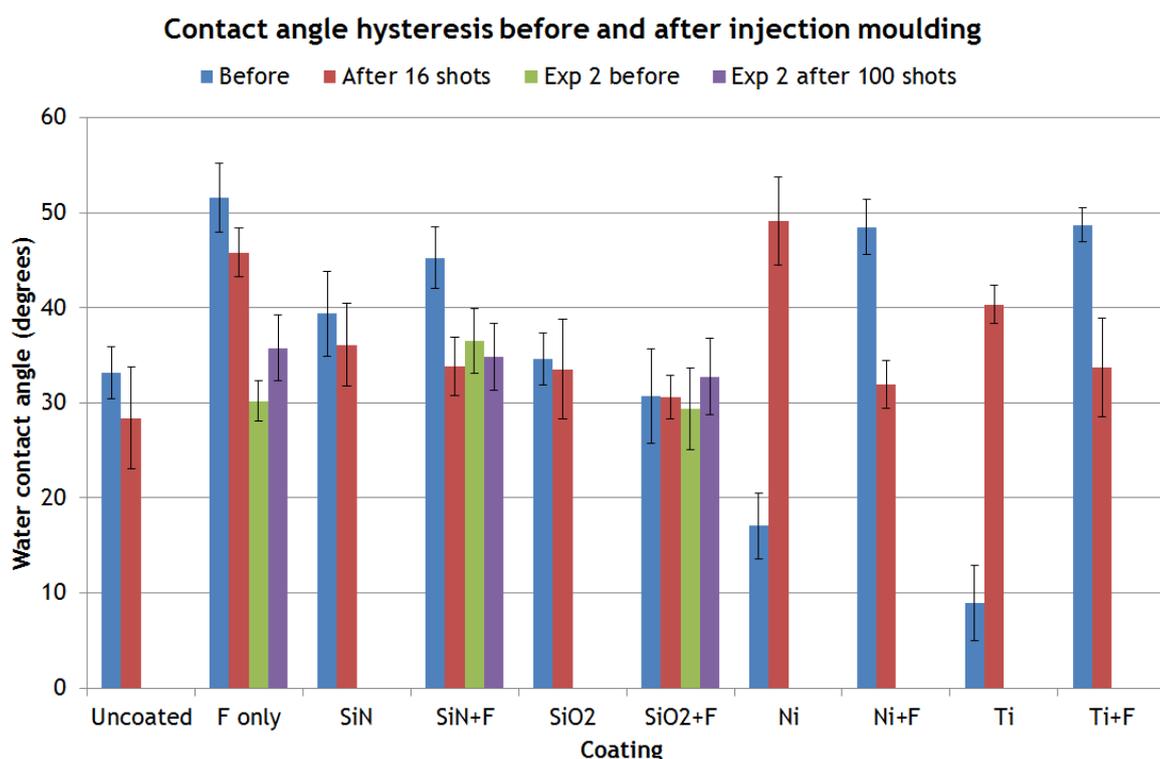
Figure 4.8 - Water contact angle hysteresis for ten (experiment 1) and three (experiment 2) inlay surface coatings before and after injection moulding. TPFS is further abbreviated to F to save space.

Taken together with the stationary WCA data one would probably expect the fluorinated oxide coating to perform most effectively as an inlay coating (or indeed any replication based nanofabrication situation) due to its combination of relatively high stationary angle (~90°) and low hysteresis (~30°) although all of the fluorinated coatings show promise in this regard. The fluorinated oxide coating also shows the greatest consistency between the two experiments and it is

therefore encouraging that these desirable surface characteristics may endure a longer production run.

Data from XPS analysis performed before and after injection moulding is presented in Figure 4.9 and shows the elemental content of the first few nanometres of ten inlays as a percentage of the total element content from each sample. Common to all samples is an increase in carbon content (blue) which is a likely indicator of PC residue present on the surface after injection moulding. Where this increase is most profound, such as with the titanium and non-fluorinated nitride, one might expect a lower quality of nanopattern replication, especially given that both of these exhibit stationary WCAs of less than 90°. Also evident here is a decrease in fluorine content for all TPFS coated inlays which may explain the slight WCA decrease generally observed for these samples, but could also just be the result of excess unbound TPFS being removed from the surface of an otherwise conformal monolayer.
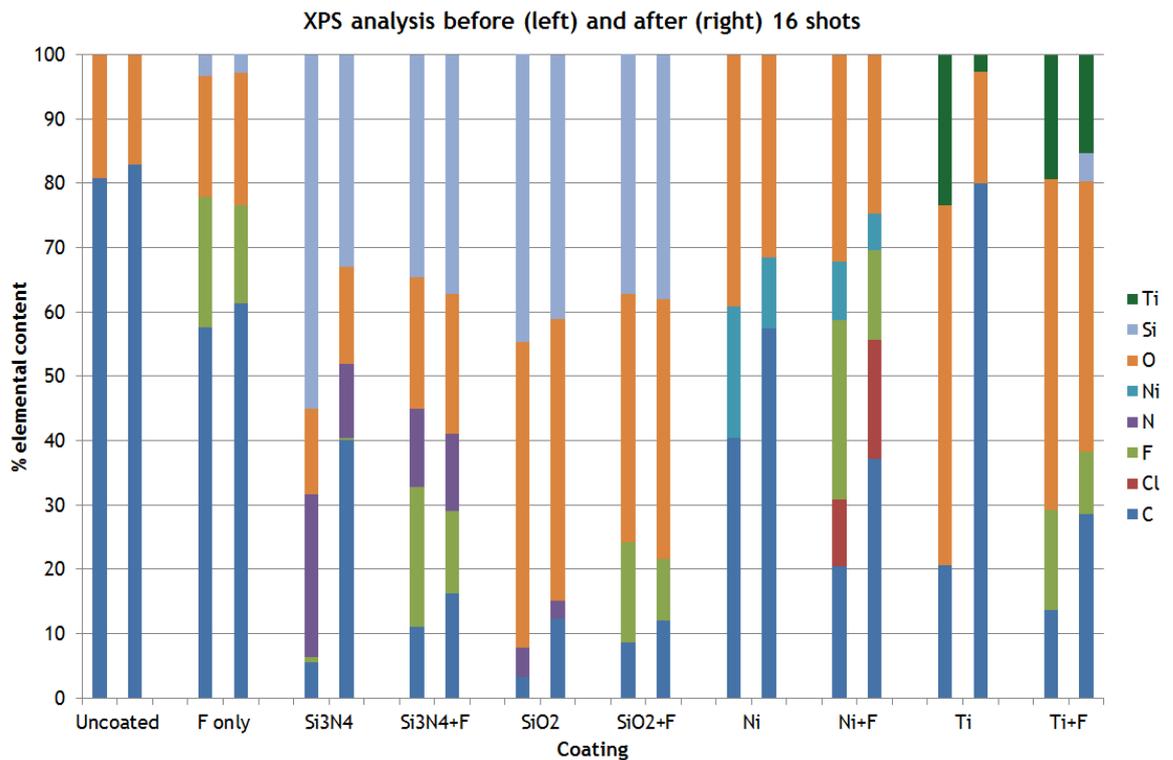
Figure 4.9 - Elemental content of inlay surfaces with ten different coatings before and after injection moulding with PC. TPFS is further abbreviated to F to save space.

Visual observation of inlays showed no obvious signs of wear or damage except in the case of non-fluorinated nickel and titanium. As shown in Figure 4.10, both of these samples show signs of surface alteration which has been transferred to their corresponding moulded parts. On the nickel coated inlay it is not immediately obvious whether the defect (positioned bottom centre) is damage to the coating or polymer residue, but the carbon increase revealed by XPS would suggest the latter. The damage to the titanium coated inlay is much more severe, and probably sufficient to

deem it unsuitable for any production purpose. It too could be polymer residue, coating removal, or both, but again the XPS data denotes an increase in carbon. This could explain either option, but it seems more likely to be primarily due to residue as a quick glance reveals that there has not been an 80% removal of titanium from the surface as suggested by the XPS data, but rather the PC residue is preventing the photons from penetrating through to the the titanium layer.
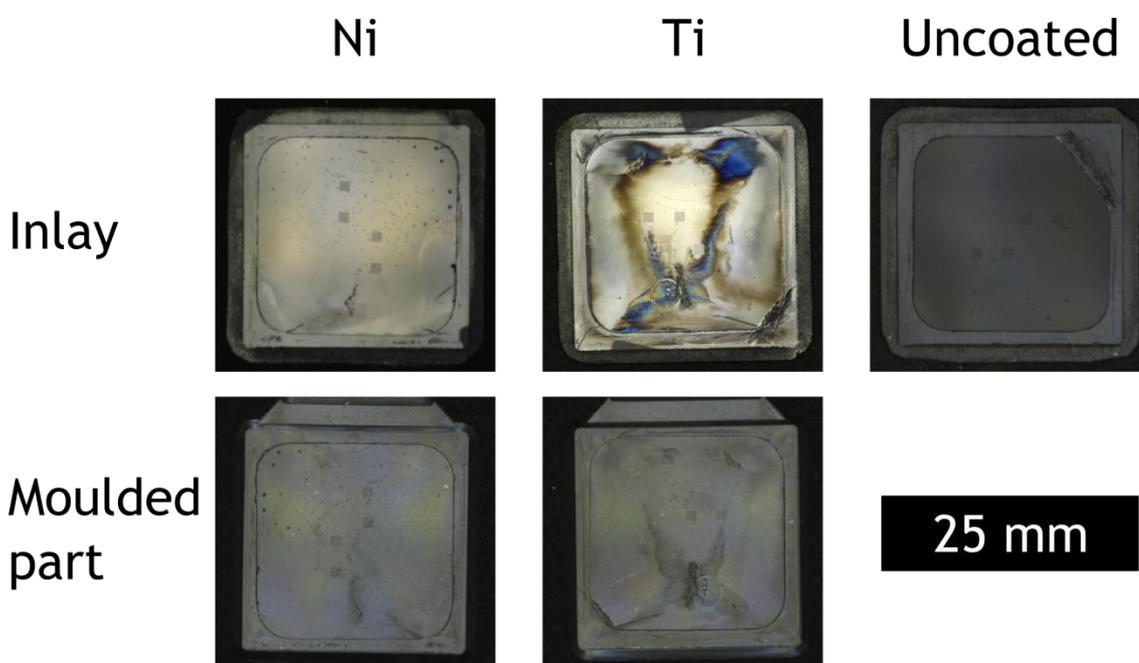
Figure 4.10 - Visible damage to nanopatterned nickel and titanium inlays sustained during injection moulding and replication of these defects in moulded parts. An undamaged uncoated inlay is shown for comparison.

This residue/damage on the titanium might also explain the corresponding jump in stationary WCA from 0° to 80° as being a reflection of significantly altered surface chemistry and/or concurrent topographical changes, something which may also explain the large jump in the value for fluorinated nickel even if the effect is not visible to the naked eye.

4.2.7 Replication of nanopillars - interpretation of results

Due to the quantity of the results presented in Figure 4.12 and Figure 4.13 a certain understanding of the methods used to gather the data is required so that it may be better interpreted. The technical implementation of the methods are discussed in Chapter 2 so here the discussion will focus on the implications of these methods and how they influence the meaningful interpretation of this dataset. The results presented consist of three data types presented together: pillar height, pillar replication success rate and pillar circularity. They are discussed below as is the sample layout.

Sample layout consisted of four identical square arrays of side length 500 μm containing 100 nm diameter pillars positioned in a square geometry with a pitch of 500 nm. Each array contained three linear grooves measuring 800 μm in length and 3, 5 or 10 μm in width which were included

to allow height analysis by AFM. The reasons for using multiple identical patterns were twofold. Firstly, it would allow ample points of measurement in the event that stamp damage would make some areas unfit for measurement, and secondly, earlier experiments had revealed high levels of inconsistency between patterned regions on a large (hundreds of μm) scale. It was hoped that this approach would both illustrate this and allow for good and bad results alike to be sufficiently illuminated; otherwise results may have become blurred by averaging. These four regions are labelled 1,2,3 and 4 on the x axis of the graphs in Figure 4.12 and Figure 4.13.

Pillar height was measured by AFM across 3 or 5 μm gaps in the pillar array and calculated as the difference between the height values of this gap region and the peaks of the surrounding pillars as described in section 2.6.3. During the NIL stage of fabrication stamp damage occurred which left some of these height measurement locations without any pillars within the region of the AFM scan. These areas were identified during SEM image capture and, as the defects were not a result of the injection moulding process and therefore not the process under direct scrutiny, were not measured by AFM. This left some areas of the figure without height data. Furthermore, as it was not feasible within a reasonable time frame to locate and take measurements of exclusively 100% defect free areas, a system was put in place to remove the contribution of stumps produced as replicas of failed pillars from the data set. This was done by ignoring the values of any pillars below 200 nm in height when the data was processed. It could be argued that this damages the purity of the data, but in terms of the development targets of this work a pillar height of only 200 nm is as good as zero as a measure of the process' success. The results do contain some data points below this threshold, but these will be an erroneous artefact of images with a small range of height values and can be ignored. Each of the four areas, if measured, was measured in at least four locations spread over two samples where possible (i.e. two measurements for each of the four identical patterns on two samples).

It is important to note that the height value of a pillar might not be the same as its actual length if it is the case that it is bent or leaning to one side.

Pillar replication success rate was calculated using SEM images of injection moulded samples taken perpendicular to the sample surface (i.e. top-down) which were processed using a method described in section 2.6.2. A feature was considered to be successful if it had sufficient contrast to its surroundings and was not touching or overlapping with any of its neighbours as illustrated by Figure 4.11. For each of the four patterned areas, at least three images on two samples (six total, but usually more) were captured. A value of success rate for each image was obtained by dividing the total number of features present by the ideal number that would be visible at that magnification. The mean value for each of the four areas was obtained by averaging the values extracted from each image.

raw SEM image   thresholded binary image   successful features only
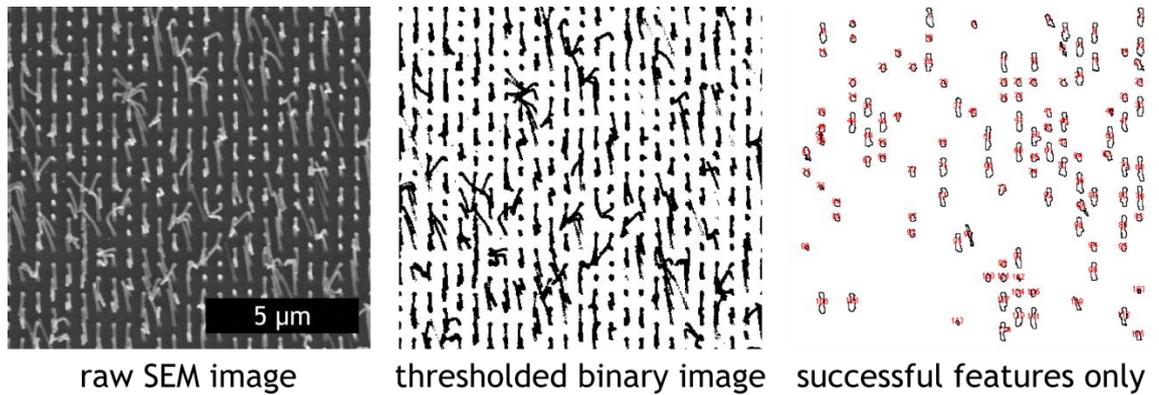
Figure 4.11 - SEM image (left) containing successful and unsuccessful (too large and/or touching a neighbour) features as interpreted by subsequent analysis (centre and right).

The important thing to consider with the success rate data is that the stumps produced by replication of broken pillars on the stamp or those of low height will usually appear to be just as successful as perfectly formed pillars provided there was sufficient contrast which was usually the case. In these instances it is important to cross reference success rate with height data.

Additionally, in the case of pillars leaning to one side, the difference between a success and a failure (a pillar not touching or touching its neighbour) may be the matter of only a few nanometres. Because of this a small amount of variability across one pattern area may lead to large variations in image to image success rate which may explain some of the large standard error bars in Figure 4.12 and Figure 4.13.

Circularity data was extracted from the same images as success rate data using results from the same analysis technique with the exception that averages were calculated using the values of all successful features across all images rather than on an image by image basis.

The fact that circularity data only exists for successful features means that it is more a measure of perfection than success and should be considered as a bonus to any strong combination of height and success rate.

4.2.8 Replication of nanopillars using inlay surface coatings

Nanopillared samples were replicated in PC by injection moulding with two melt/tool temperature combinations: $T_m = 280°C$, $T_w = 80°C$ and $T_m = 260°C$, $T_w = 65°C$. These are the temperatures which represented maximal and minimal stretching respectively in the results obtained in Chapter 3. Injection speed (v_i) and cooling time (t_c) were kept constant at $50cm^3s^{-1}$ and 15 s respectively. The 15 s cooling time was chosen so that the PC should be well below T_g at the point of ejection, based on the simulation data from the previous chapter (Figure 3.2) which shows that nanopillars should be below T_g after 8 s and the bulk of the part should follow after about 10.5 s. Results

obtained from this large systematic study into the effects of inlay surface coating at two temperature conditions are summarised in Figure 4.12 and Figure 4.13.
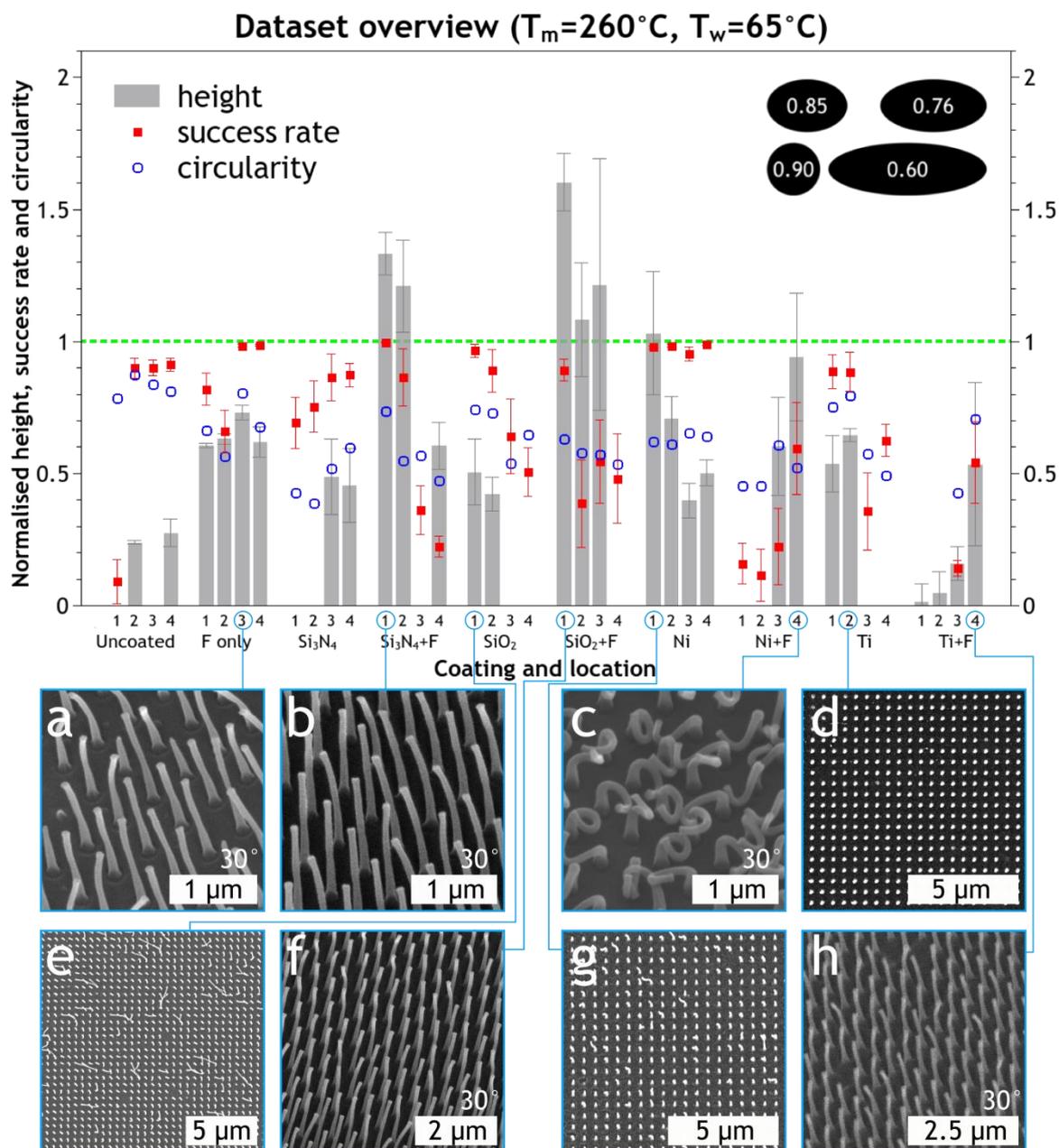
Figure 4.12 - Combined plots of mean modal pillar height (normalised to stamp height = 975 nm), mean pillar replication success rate and mean circularity of injection moulded nanopillars made with T_m=260°C and T_w=65°C. Accompanying SEM images are supplied which correspond to results as indicated. A reference by which to interpret circularity is given at the top right. TPFS is further abbreviated to F for the purposes of this figure.
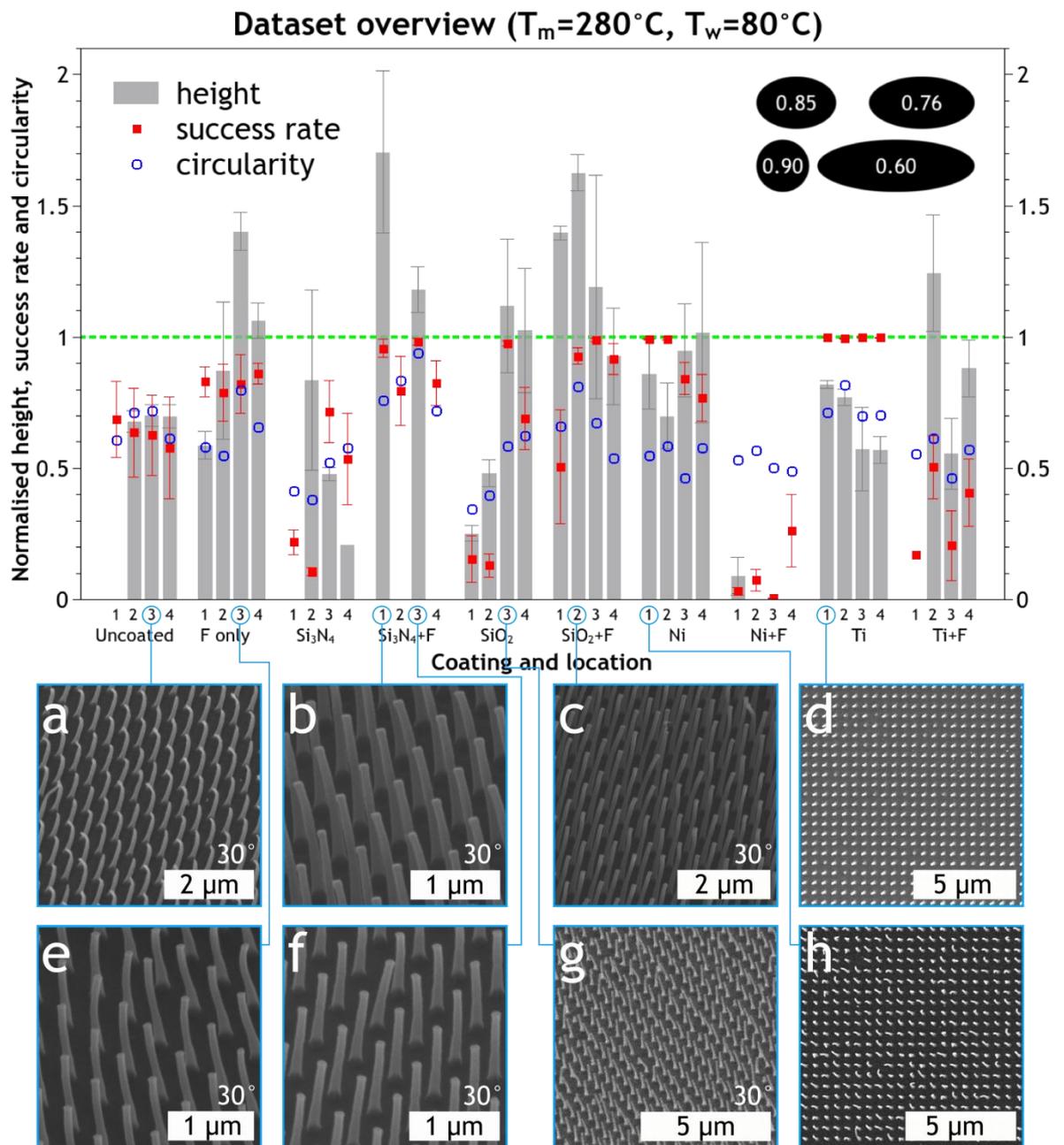
Figure 4.13 - Combined plots of mean modal pillar height (normalised to stamp height = 975 nm), mean pillar replication success rate and mean circularity of injection moulded nanopillars made with T_m=280°C and T_w=80°C. Accompanying SEM images are supplied which correspond to results as indicated. A reference by which to interpret circularity is given at the top right. TPFS is further abbreviated to F for the purposes of this figure.

Looking firstly at the SEM images some excellent results have been obtained in terms of the formation of HAR nanopillars, but what is not present is anything that closely resembles the pillars on the stamp (Figure 4.3). Injection moulded pillars often appear to be stretched and most appear to be at least slightly bent in some way. Apparently stretched pillars, such as those in Figure 4.12 a, b, f and h and Figure 4.13 b, c, e, f and g, tend to have a well-defined tip which is presumably the location where the base of the mould cavity "*grips*" the polymer, causing stretching of the main bulk of the pillar to stretch as the part is ejected. This effect was previously observed in the experiments documented in Chapter 3. Possible causes of this gripping action are illustrated in

Figure 4.14 and further discussed throughout this section but are probably the result of increased friction due either a lack of non-adhesive coating at the base of the inlay's HAR nanopits or some sort of physical widening at the base of the pit, perhaps caused by the displacement of air during NIL. It may also be due to differences in the rate of pillar cooling as illustrated in the lower half of Figure 4.14.
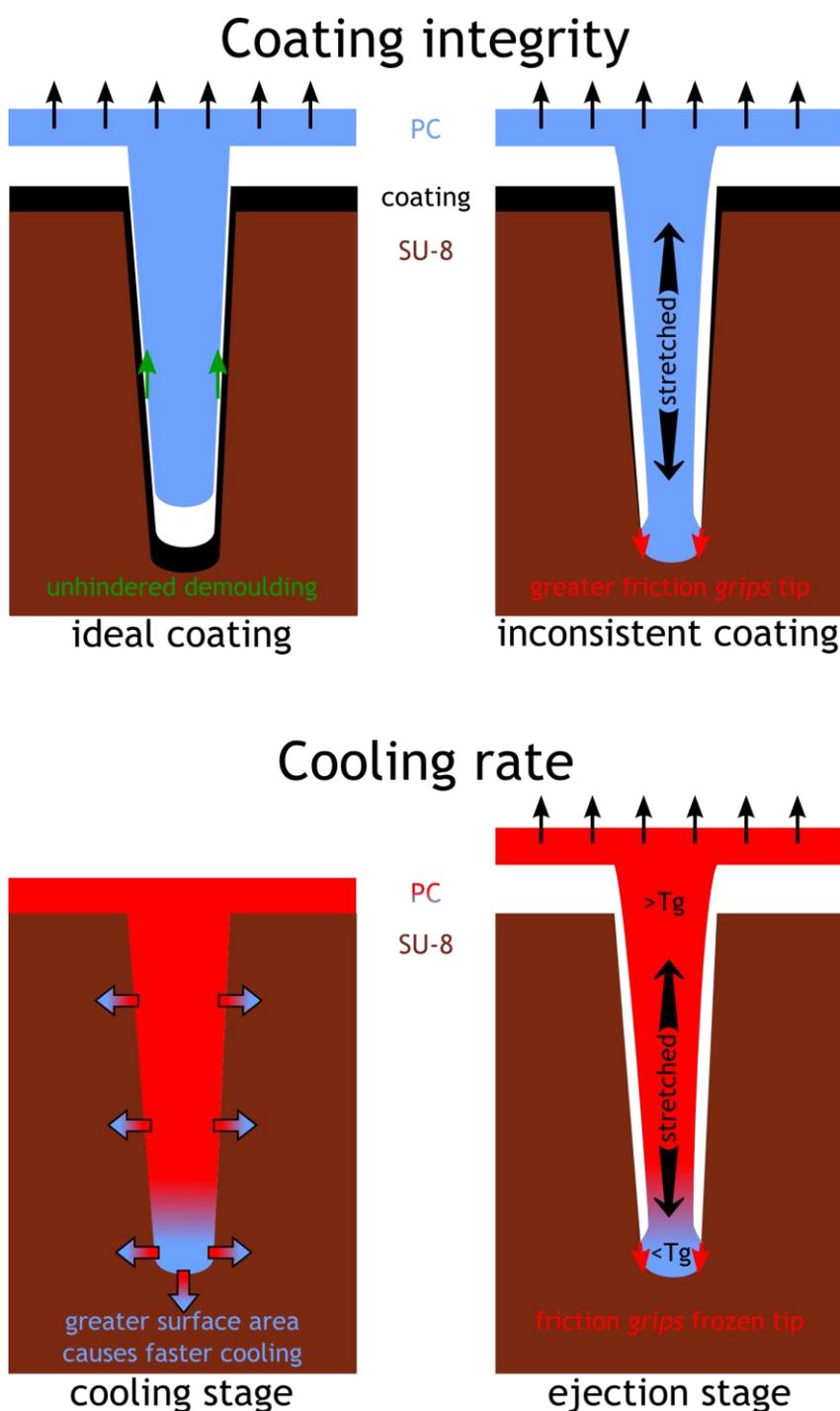
Figure 4.14 - Schematic illustration of possible causes of pillar stretching and tipped morphology.

Turning the attention to the graphical data, perhaps the most immediately striking observation that can be taken from these results is the large degree of variation within each coating condition.

These variations exist at different lengths scales, but may be related. Millimetre scale variation is shown by the differences across areas 1,2,3 and 4 while micrometre scale variation within each area (on an image to image basis – where an image is equivalent to a measurement) is indicated by the large standard error bars present at many of the data points. For coatings where variation across the four areas lies within the range of vertical error bars these variations can be attributed to the same image to image micron scale variation and the results considered as relatively consistent at the millimetre scale. This viewpoint immediately makes thing appear more consistent, particularly at the higher temperature combination and for the metal and fluorinated oxide and nitride coatings.

It is tempting to dismiss locations without height measurements or with values below 200 nm (~ 0.2 normalised) as a direct effect of stamp failure alone, but knowledge of the order in which inlays were fabricated by NIL dismisses this. While the precise order of inlay patterning was lost in the practical realities of sample management, certain physical characteristics allow for verification that the uncoated and TPFS-only inlays were the last two to be patterned so, given that the TPFS-only inlay produced normalised feature heights of over 0.5 for both conditions at all locations, stamp failure does not appear to be a valid reason for the occurrence of low/absent heights elsewhere. However, in situations where an absence of height is surrounded by large heights and high success rate (such as Si_3N_4+TPFS at 280/80°C) the absence of a measurement does not necessarily imply a low height. This is because some regions were chosen not to be measured after SEM imaging had revealed what appeared to be localised stamp failure at the height measurement locations of certain samples. In this light it is probably best to ignore absent height data from the formation of conclusions about the success of coatings to replicate nanopillars effectively.

If absent height data is ignored and variations in success rate considered consistent within the range of error bars the picture looks a bit better, but there is still considerable variation, particularly at the lower temperature combination and for the non-fluorinated oxide and nitride at the higher temperatures. It is now worth considering non-uniformities in the coatings on the millimetre scale as a cause of this. Although metal evaporation, CVD and ICP deposition are specifically designed to deliver highly uniform layers, the layers they provide are not designed to for the large physical forces subjected to injection moulder tooling.. With layers as thin as 10 nm it is not unreasonable to suggest that under injection moulding conditions any weakness in integrity could be readily exacerbated. Although significant coating degradation was not evidenced by WCA analysis (Figure 4.7 and Figure 4.8), there does appear to be the suggestion of a relationship between the post injection moulding static contact angle and pillar height (and to some extent success rate and circularity at the higher temperature combination) as shown in Figure 4.15. A hypothetical trend line has been added to each scatterplot to highlight the way that mean height increases with WCA up to a normalised value of around 1, above which a height increase seems to be accompanied by a lower contact angle. This indicates that there may be an optimum angle associated with perfect (normalised height = 1) replication at the point where the speculative trend line doubles back

(~100°), although there must be other factors which dictate whether a point will lie above or below the height value of 1 that are independent of WCA. As WCA is an analogue of surface energy, this trend also suggests that pillar stretching is caused, at least in part, by an enhanced interfacial interaction between the injected polymer and the tooling that is detectable on a macroscopic scale through WCA measurements.
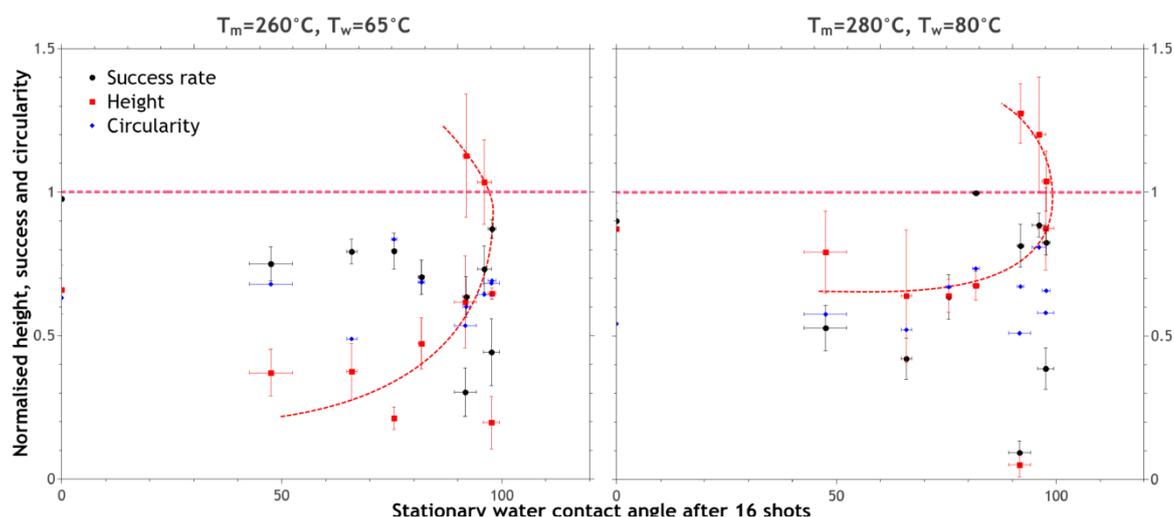
Figure 4.15 - Scatterplot illustrating the relationship between post injection moulding WCA and pillar height, success rate and circularity. A possible trend line for height has been added to each plot.

Further to the WCA data, the consistent increase in carbon concentration across all samples revealed by XPS (Figure 4.9) indicates a surface change of some form, most probably a build-up of PC, that may or may not be uniform across the sample (the spatial resolution of XPS is not sufficient to reveal coating inconsistencies on this length scale). The scatterplot in Figure 4.16 appears to indicate some correlation between this change of surface carbon content and all three markers of replication performance (averaged across all four locations for each coating – ignoring absent height values). With titanium as a notable outlier, these plots seem to indicate that the tendency for a surface to accumulate carbon during injection moulding is accompanied by a significant reduction in success rate, pillar height and circularity.
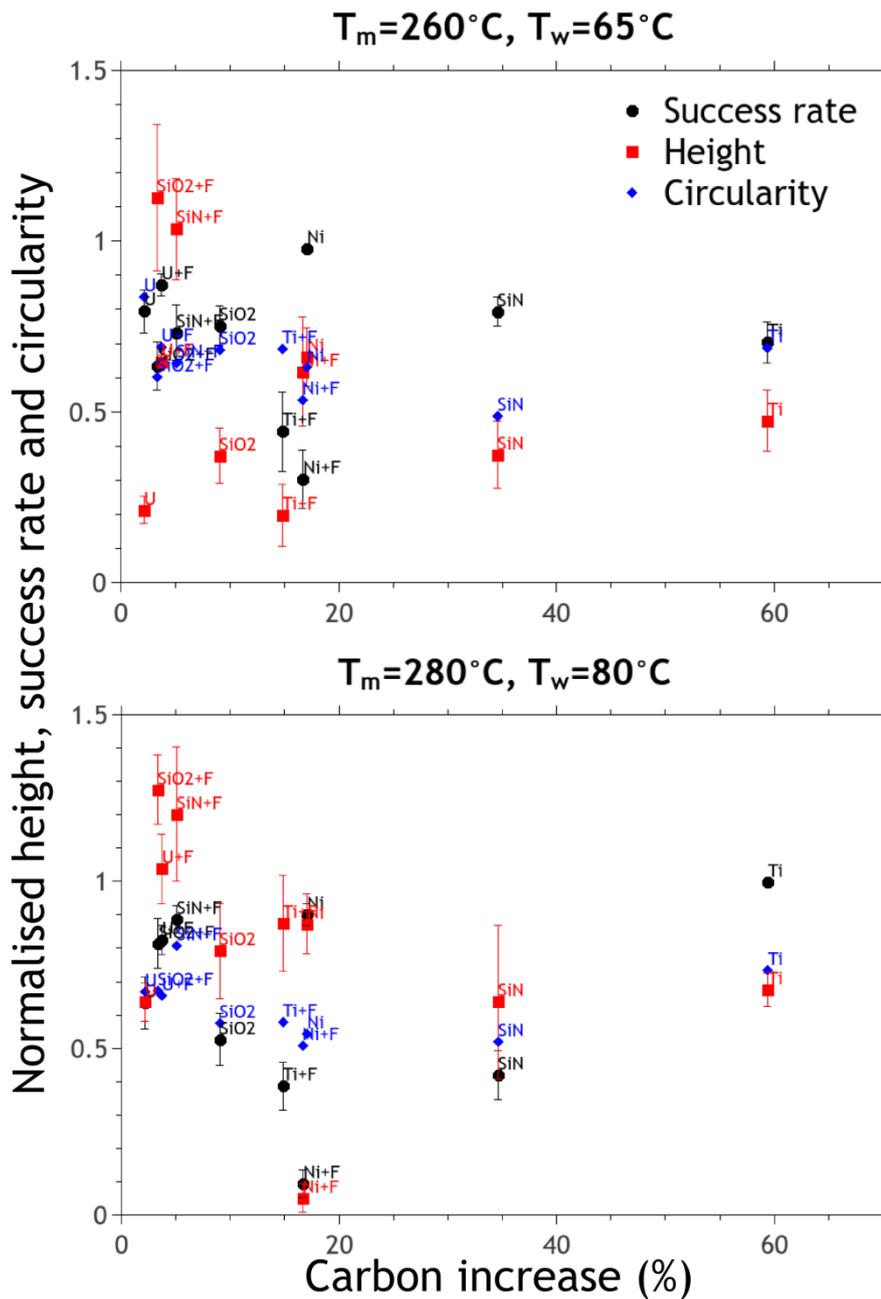
Figure 4.16 - Scatterplot showing how the increase in surface carbon content after injection moulding relates to the replication performance indicators of height, success rate and circularity.

The method of storage for these samples presents another possible source of variability. Due to the large quantities of samples produced and their non-standard form factor it was not practical to store them in individual containers. Instead they were stored loosely in bags containing around five samples each where they can move freely and potentially cause physical damage to one another's nanopatterns. It was not uncommon to find areas which resemble scratches where pillars appeared to have been flattened and while care was taken not to capture such areas in SEM images for analysis, it was not always possible to identify these areas for what they were, particularly through the navigation microscope of the AFM.

The method by which success rate was measured highlights image to image variability on samples where pillar bending was near the success/failure threshold of a pillar touching its neighbour. Due to the method of characterisation a small yet critical difference in pillar bending between two images could see one have a close to maximal success rate and the other obtain one of zero. Locations on the dataset overview figures with relatively large error bars for success rate may be candidates for this type of variation if they are accompanied by a relatively low value for circularity such as in region 1 of the SiO_2+TPFS coating at 280/80°C. Here the success rate error bars are almost as great in magnitude as the data point, the circularity is below 0.7 and the height is greater than that of the stamp. The raw data reveals that in this case it is more a case of sample to sample variability with the image on the left of Figure 4.17 being typical for region 1 on the first sample measured and the image on the right typical of the same region on the second. Nonetheless, this type of image to image variation is a likely cause of much of the local variability in success rate and the images in Figure 4.17 illustrative of yet another degree of variation in the dataset.
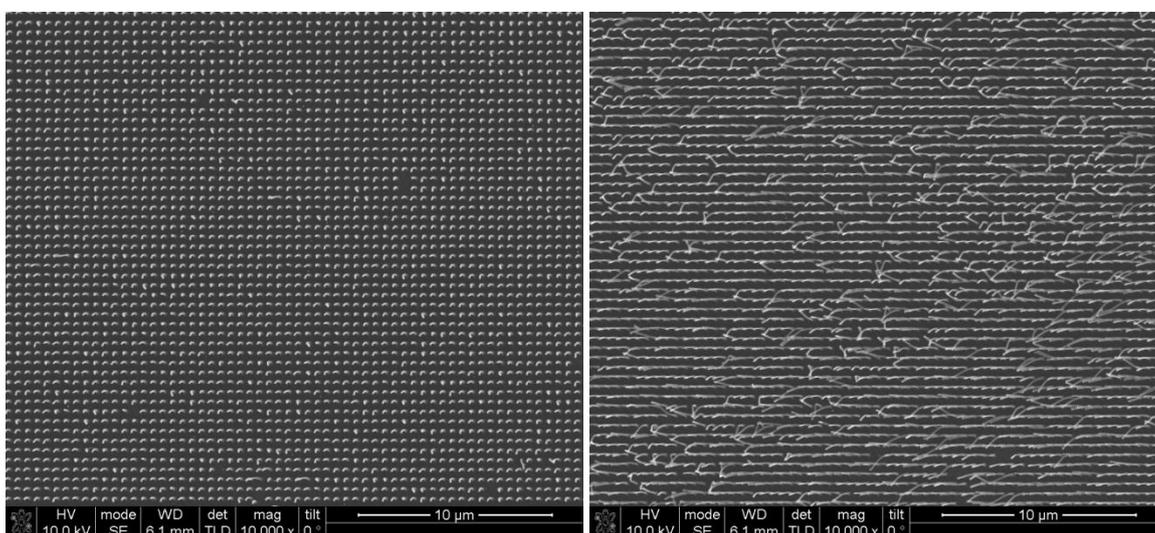
Figure 4.17 – Sample to sample variation for the same injection moulding conditions and inlay coating in the same inlay region.

Variation also exists on a third length scale: the pillar to pillar variation. The SEM images provided for the SiO_2 coating in the 260/65°C data (Figure 4.12 e) and in Figure 4.18 reveal that a significant minority of pillars are elongated substantially more than the rest. This was a common sight during SEM analysis.
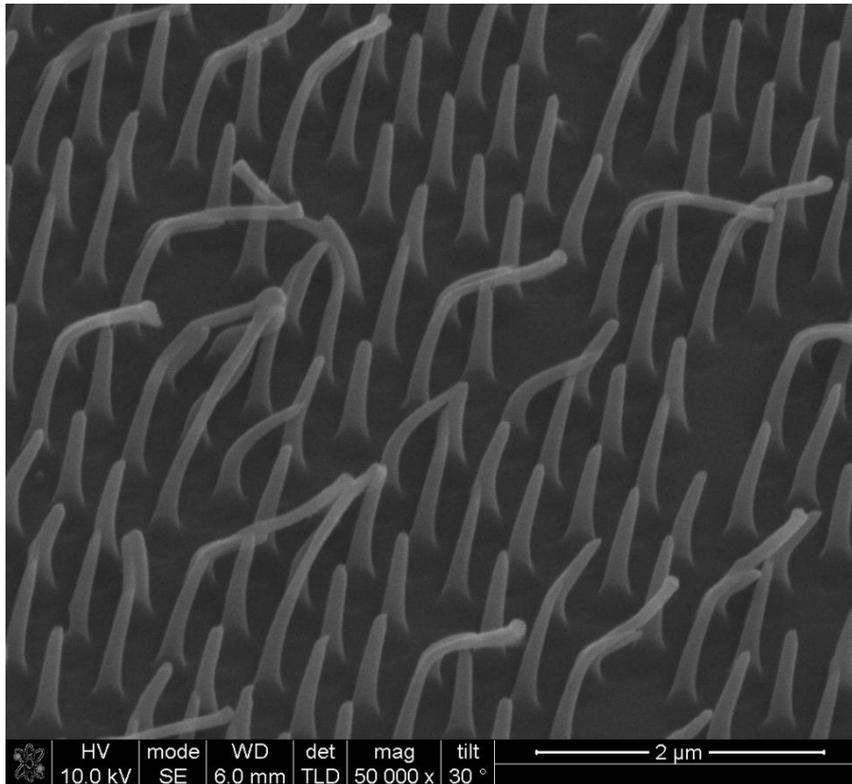
Figure 4.18 - Occasional excessive stretching of nanopillars in an otherwise uniform field. Coating = TPFS-only, T_m = 280˚C, T_w = 80˚C.

Variation on this scale is difficult to quantify due to the vast amounts of images that would have to be captured in a systematic way and the many parameters that would have to be interpreted by computer analysis. Large volume image processing and machine learning techniques such as those used in, for example, cell biology[129] could be incorporated here, but the amount of SEM time and difficulty of automating an SEM to perform the necessary measurements make such analysis beyond the scope of this project. A likely cause of this type of variation is the consistency of surface coatings on the sub feature size scale, particularly towards the bottom of high aspect ratio cavities in the inlays. This, or a physical deformation at the same location, could increase the friction between the polymer and tooling at the pillar tip, causing it to be stretched more than its neighbours when the part is demoulded.   Indeed, it may be a consistent occurrence of such physical inconsistencies that cause the more uniform formation of pillars which exceed the height of those on the stamp.

Despite all the inconsistencies there are some encouragingly high and consistent success rates at a local level which accompany heights greater than or equal to that of the stamp. These are particularly prevalent with the warmer temperature combination with the fluorinated oxide and nitride coatings and, to a lesser extent in terms of height, the non-fluorinated metal coatings. The fluorinated oxide and nitride do not surprise in this regard in light of the promising WCA and XPS results discussed above, but the metals throw up some questions, particularly given the residue/damage observed on both of these inlays. Nickel is well established as a successful tooling

material for injection moulding nanopatterns when the features are holes and titanium has been the basis of a recent patent on similar hybrid tooling to that developed in this project.[90] Perhaps these mateials require a base level of polymer residue accumulation to provide a favourable surface interaction and may be less prone to damage and bulk residue build up if they existed as something more substantial than a 10 nm layer. It is clearly evident that attempts to apply fluorosilane coatings to either of them have a negative effect on their ability to replicate nanostructures so there may well be a chemistry component to this which has not been considered. Whatever the case may be, the residue/damage shown in Figure 4.10 makes them unfit to be applied to this particular tooling solution where they could not exist as anything other than a thin (< 20 nm) film without obscuring the nanopattern.

Having considered the results in the context of the variation across each sample, it is helpful to take a step back in order to further ascertain which inlay coating shows the most promise as a means to facilitate the replication of high aspect ratio nanopillars. This will also help in comparing the two temperature conditions. Figure 4.19 shows bars representing the three pillar characterisation metrics averaged across all locations for each condition rather than being split into four regions as before and ignoring absent height values.
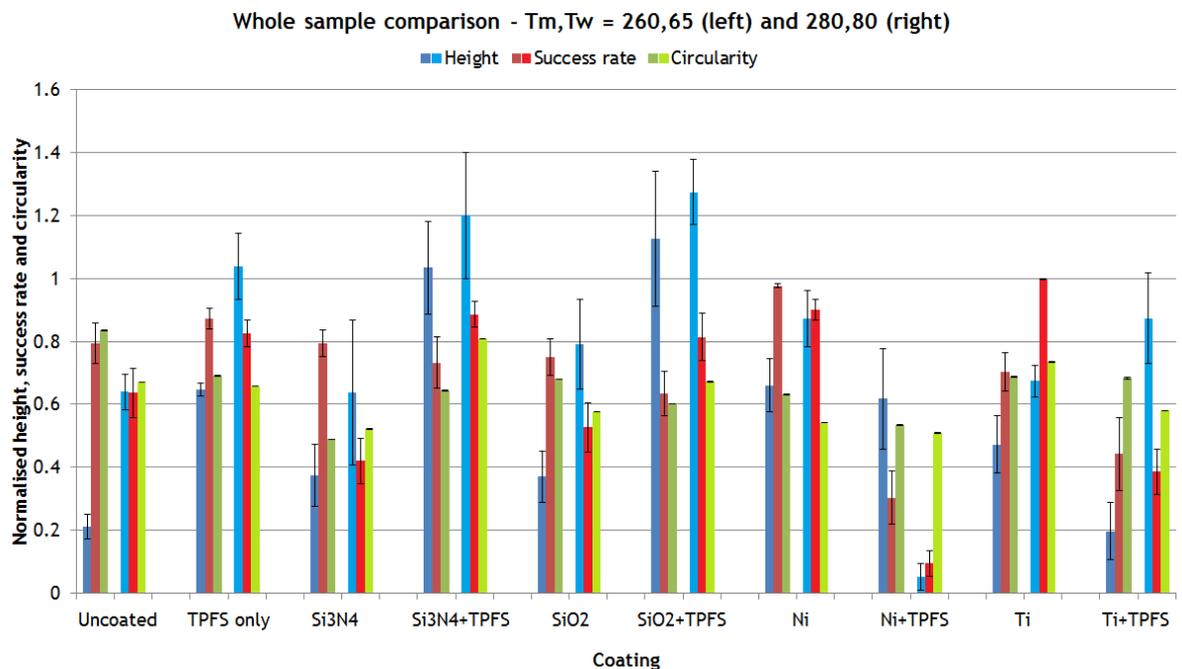
Figure 4.19 - Dataset overview, averaged over all pattern locations, of injection moulded nanopillar characteristics made with ten differently coated inlays at two temperature conditions T_m, T_w (°C) = 260,65 (left bars, dull colours) & 280,80 (right bars, bright colours). v_i = 50 cm^{3}s^{-1}, t_c = 15 s.

Observation of the data in this format makes it easy to see the effect of temperature. As was the case with the low aspect ratio pillars in Chapter 3 the increased temperatures made it possible for injection moulded nanopillars to exceed the height of the original quartz stamp by a controlled stretching process. In contrast to those lower aspect ratio pillars (~1:1) which would be fully filled

using an uncoated inlay at 260/65°C, these high aspect ratio structures will not fill beyond around 200 nm at that temperature combination nor much above 600 nm with the higher temperatures without the presence of a non-adhesive surface coating. Whether this is due to polymer build-up at the base of holes or just incomplete filling, it is clear that non-adhesive surface coatings are required to fully replicate HAR nanopillars. However, what remains elusive is a means to make uniform replicas of HAR nanopillars, stretched or otherwise. Results for TPFS-only and Si_3N_4+TPFS coatings have means close to unity, but with standard errors of around 20% this is far from ideal. This variability and the tipped morphology of these and more stretched pillars almost certainly suggests that the surface coatings used are either ineffective at, or do not consistently reach, the base of the HAR holes in the inlay.

In terms of success rate, perhaps more important than height, values above 90% are only seen for the non-fluorinated metal coatings, but not only do both of these fail to facilitate full replication of pillars heights, but they have displayed problems of polymer build-up and/or surface damage which make them unsuitable for the fabrication of usable devices.

In general it seems as though TPFS-only and the fluorinated oxide and nitride coatings are the most promising, but substantial refinement would be required to achieve a near 100% success rate and uniform height, before even beginning to worry about perfectionisms like circularity.

4.2.9 Results from other experiments into the effects of surface coatings, temperature, pillar size and pillar density

In addition to the systematic study of surface coatings described above, some additional data obtained from injection moulding HAR nanopillars with inlay surface coatings was performed. In an initial exploration into the effects of some surface coatings (SiO_2 + TPFS, Si_3N_4 + TPFS and TPFS only) and processing temperatures (T_m/T_w (°C) = 270/80, 270/90, 280/80, 280/90) using pillars of the same dimensions as the large coating study (pillars on stamp had 100 nm diameter, ~1000 nm height), data for success rate was obtained. Data was collected and analysed using the same method as in the large coating study except only one sample was measured for each condition. These results are presented in Figure 4.20.
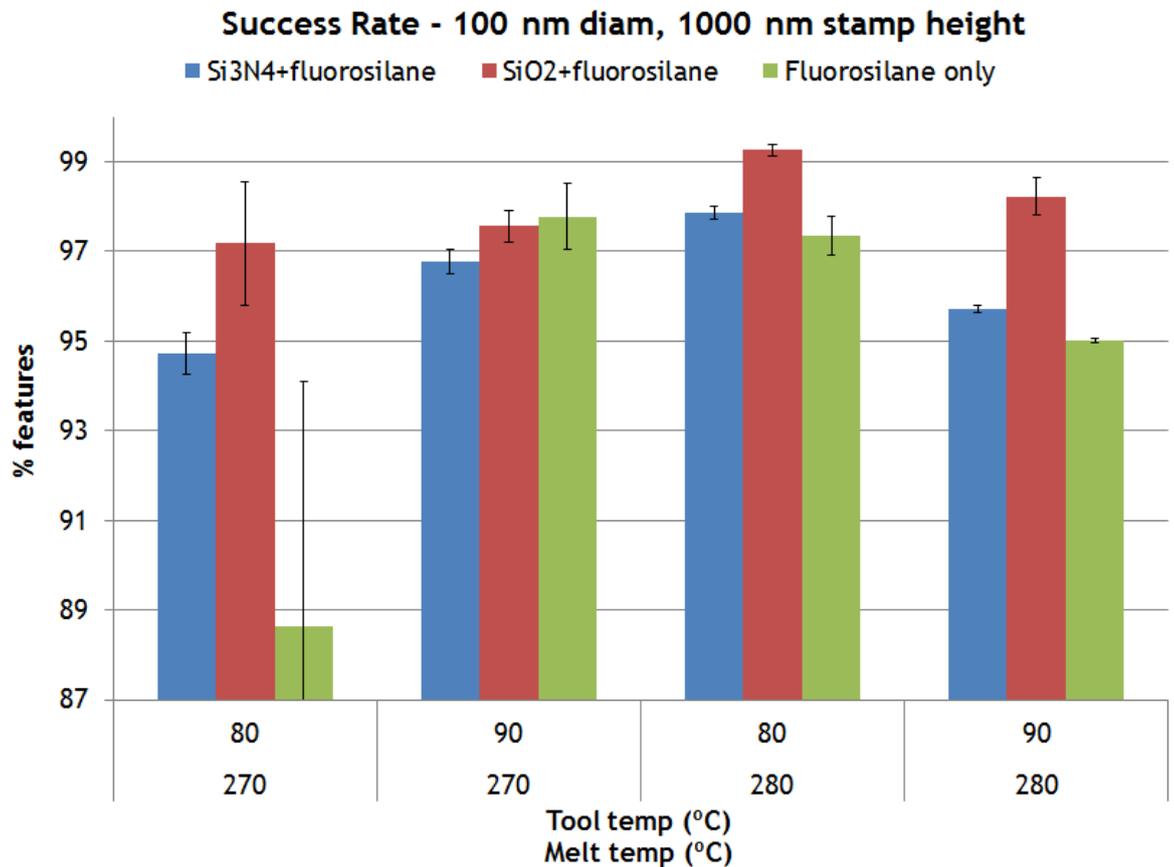
Figure 4.20 - Success rate of injection moulded PC nanopillars made with three differently coated inlays at four different temperature conditions. v_i = 50 cm^{3}s^{-1}, t_c = 5 s.

The results presented here indicate noticeably superior replication success and consistency than the data obtained in the main coating study (notice the y axis starts at 87%). Unfortunately, it was not possible to obtain height data to accompany these results as the patterns did not contain the gaps required for AFM analysis, but during SEM inspection pillars did appear to have heights greater than those on the stamp. The high success rates and consistency are quite startling in light of the results from the larger study and indeed, it was these initial results that indicated the need to perform a systematic study into the effect of different surface coatings.

In further addition to the results already presented, during a production run of HAR pillared samples to be used by biologists, some samples were retained from which success rate data was obtained. These results are presented in Figure 4.21 which compares the success rate of nanopillars of different sizes on the 105th and 249th parts produced during the production run. The original stamp for these parts contained pillars of two different diameters etched to two distinct heights which relate to the four size combinations indicated on the x axis of the figure. The inlay coating used was SiO$_2$+TPFS and the process conditions were: T_m = 270°C, T_w = 90°C, t_c = 5 s. These results show an even higher success rate and level of consistency across the board and while it was not possible to obtain accurate height data, SEM inspection revealed pillar height to be generally

greater than pillar height on the stamp along with the hallmarks of stretching. It also did not reveal any signs of poor filling, pillar breakage or widespread flattening.
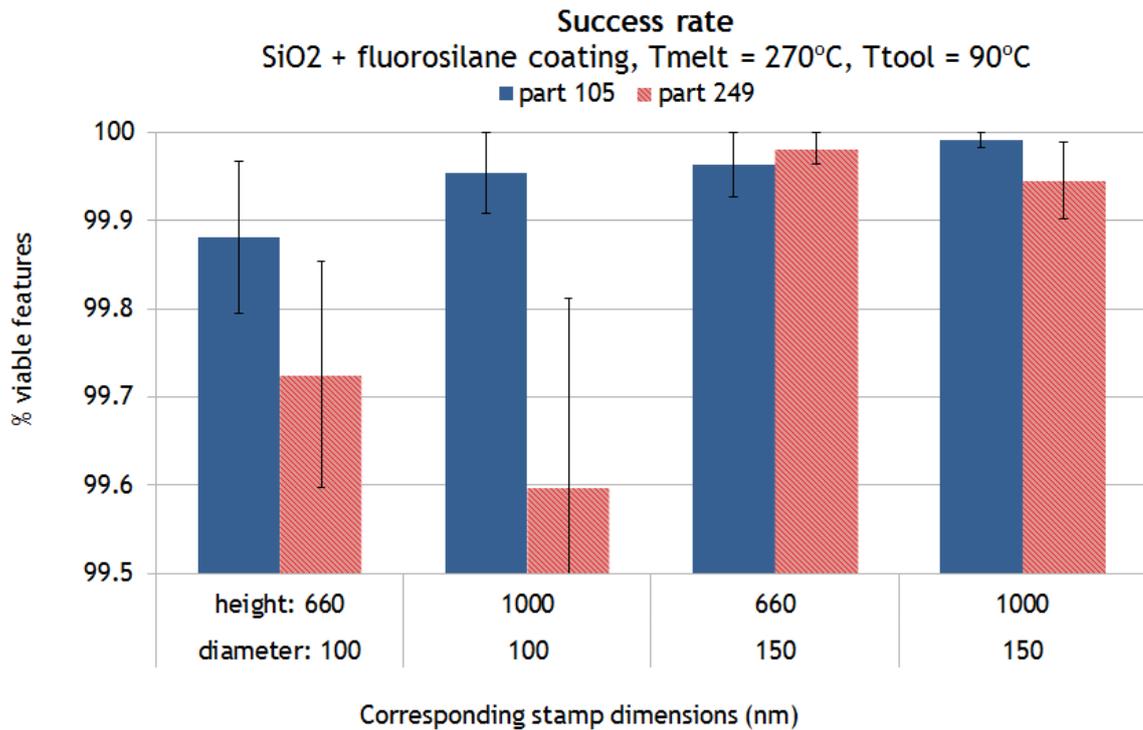
Figure 4.21 - Success rate of HAR nanopillars of different sizes for the 105th and 249th parts produced in the same production run. Tm = 270°C, Tw = 90°C, v_i = 50 cm³s⁻¹, t_c = 5 s.

A slight reduction in success rate is observed for both heights of 100 nm diameter pillars over the 144 cycles between the production of the two parts measured. It is interesting that no significant reduction is observed for the wider pillars of either height, suggesting that replication quality over a large production run might be more dependent upon lateral feature dimensions than aspect ratio. This and the results from the uncoated inlays presented earlier (section 4.2.5, page 95) indicate that there may be a critical dimension of around 100 nm where feature replication of PC becomes more difficult although is greatly enhanced by the addition of non-adhesive coatings.

A factor that may be very important in explaining the discrepancies between the above two sets of results (Figure 4.20 and Figure 4.21) and the large coating study (Figure 4.19) is cooling time (t_c). For the two datasets immediately above, t_c was set to 5 s, but in the large study t_c was set to 15 s to ensure that the PC would definitely be below T_g. This was based on the simulations in Chapter 3 (Figure 3.2, page 70) which state that a 1μm tall 100 nm diameter pillar should reach T_g about 8 s after injection. Despite the fact that cooling time did not appear to play a significant role in Chapter 3 (Figure 3.7, page 74), it may be that it does here and/or that the simulation is providing false information about the time at which the PC comprising the newly formed pillars solidifies. Indeed it is hard to think of a way that the pillars could stretch without being above T_g, because in their solid state a pulling force at the tip would most likely cause them to snap. If the simulation is

incorrect, then the consistency of the two small studies conducted with t_c = 5 s could be attributed to uniform pillar stretching, while the large study could be displaying its inconsistencies because t_c = 15 s is a critical time point in the cooling process where pillar temperatures are very close to T_g and small local variations could cause adjacent pillars/regions to be slightly above and below T_g at the point of ejection. Unfortunately, time did not permit a systematic study of cooling time for these structures, but it would certainly be an important factor to explore in a future extension of this work.

One further interesting result is that provided by more densely packed pillars. Not only did these dense patterns exhibit greater resilience than pillars on a larger pitch during the patterning of inlays by UV-NIL, but they also fared well in the injection moulding process. Figure 4.22 shows two examples of these dense pillars replicated in PC. Although there appears to be some variation in the amount of stretching, particularly in the image on the left, the overall consistency across the patterned area was very high with no noticeable evidence of poor filling or damaged regions encountered during SEM inspection. There appears to be some tendency for the tips of pillars to stick together, indicating adhesive forces, which suggests that this type of patterning may be applied to the development of dry adhesive surfaces that are mimetic of gecko feet. Indeed, they do appear similar in morphology to some of the synthetic gecko foot structures reported in the literature.[20, 130]
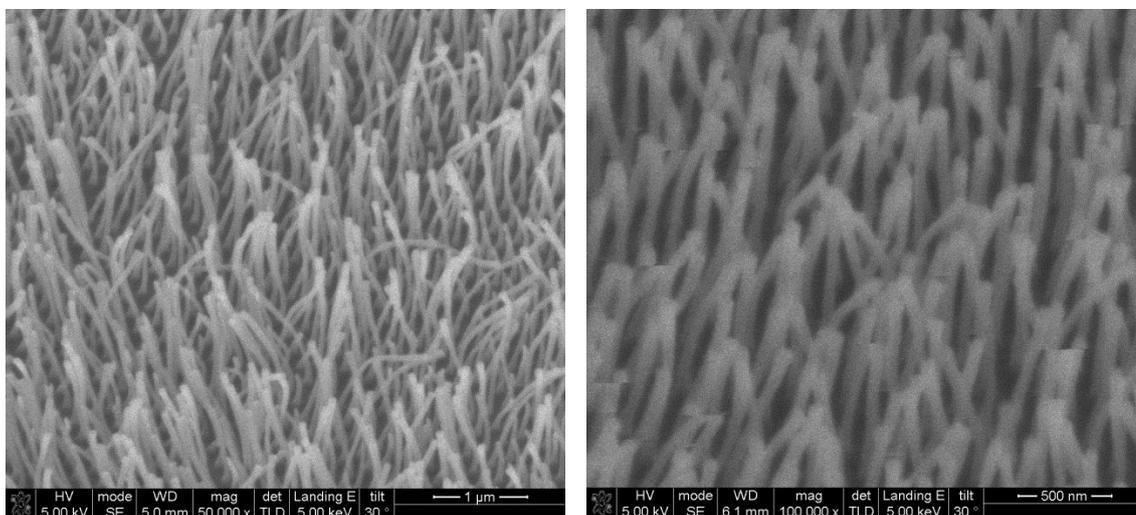
Figure 4.22 – SEM images of injection moulded dense HAR PC nanopillars nade with (left) Si_3N_4+TPFS and (right) SiO_2+TPFS inlay coatings. Tm = 280ºC, Tw = 80˚C, vi = 5 s.

4.2.10 Using coated tooling to eliminate stretching of low aspect ratio nanopillars

To assess the impact of a non-adhesive coating on low aspect ratio pillars (~1.2:1) a nanopillared inlay (hole diameter ~100 nm, hole depth = 121.9 nm mean with standard error: 3.2 nm) of the type used for the study in Chapter 3 was coated with Si_3N_4 by ICP deposition followed by vapour

fluorosilane deposition. It was then used to fabricate PC replicas by injection moulding with v_i = 50 cm^{3}s^{-1}, t_c = 15 s and the two temperature combinations used in the main study of this chapter: T_m = 260°C, T_w = 65°C and T_m = 280°C, T_w = 80°C. Under these conditions the evidence obtained in Chapter 3 would predict that, for an uncoated inlay, the heights of replicated pillars would have normalised values of around 1 and 1.4 respectively. It was expected that the addition of a non-adhesive coating to the equation might mitigate the stretching of pillars at the higher temperature combination.

The results measured by AFM did indeed show that injection moulded pillars made with the coated version of this inlay did not exhibit stretching and actually gave normalised values of lower than 1 for both temperature combinations, with the warmer 280/80°C actually producing shorter pillars, 74.2% (90.5 nm) of the inlay depth compared to 260/65°C which gave a mean value of 82.0% (100.0 nm). These mean values were calculated from six measurements over three samples and had standard errors of around 5 nm (~4%) for both temperature conditions. This reduction of filling at higher temperatures is unusual, but could be explained if the hydrophobic surface coating was responsible for a dewetting which impeded the filling of structures, although this seems unlikely given the results for HAR pillars which generally fill well beyond 120 nm.

4.3 Conclusions

4.3.1 Success in achieving the aims of the chapter

Some interesting results were seen and insight gained through the work described in this chapter. What follows is a point by point assessment of success in terms of the aims stated at the beginning of the chapter.

- The tooling solution developed in the previous chapter has been successfully translated to enable the fabrication of HAR PC nanopillars with diameters of 100 nm and aspect ratios of 10:1 and higher. The realisation of these features does however fall sort of true *replication* given the stretched morphologies of the injection moulded pillars which do not really resemble those on the stamp. This translation process encountered problems at the NIL stage, but these were solved by refining the stamp fabrication process. The consistency of pillar height, success rate and circularity seems to be a major issue as shown by the large dataset, but the two smaller studies towards the end of the chapter indicate a much higher consistency for success rate (> 99.5%). These discrepancies may be attributable to differences in cooling time, but further investigation would be required to confirm this.

- The lower boundaries of achievable feature size were not pushed to the limit as intended, but there is no reason to suggest that HAR pillars much thinner than 100 nm could not be obtained if non-adhesive inlay coatings are employed.

- Inlay coatings have been shown to affect height, success rate and circularity of HAR PC nanopillars. While there were inconsistencies across the entire coating study there were clearly coatings which outperformed the others; namely: TPFS-only, SiO_2+TPFS, Si_3N_4+TPFS, Ni-only and Ti-only (Figure 4.12,Figure 4.13 and Figure 4.19). Of these five the fluorinated coatings seemed to excel more at stretching at the expense of success rate (although this was still generally above 80% at the higher temperature conditions), while the metal coatings might not fully fill HAR structures, but they tended to have close to 100% success rate. In light of this and the > 93% success rates obtained for fluorinated oxide and nitride and the TPFS-only inlays, it would seem that all five have good potential, but the three fluorinated coatings may offer the greatest potential for achieving higher aspect ratios if the heights can be made more consistent. These three also seemed to show promise in terms of the durability metrics of WCA and XPS, but this has not been tested over enough cycles (~100) to be conclusive, although the consistent success rate of SiO_2+TPFS up to 249 shots is encouraging. Furthermore a speculative trend has been proposed where perfect height replication may be characterised by a certain contact angle value (Figure 4.15) and links have been proposed between all three metrics and the tendency for a surface to accrue carbon residue (Figure 4.16)

- A non-adhesive Si_3N_4+TPFS coating was shown to prevent the stretching of low aspect ratio nanopillars. The results were unusual in that the higher temperatures produced less well filled pillars (74.2%) than the cooler combination (82%),and the general effect of the coating contrasts behaviour at high aspect ratios where it does not seem to mitigate stretching.

- Functional surfaces for cell-substrate interactions have been produced and the > 95% success rate retained by them over 249 shots is impressive (Figure 4.21). Figure 4.23 shows an example of an LE2 epithelial cell on HAR PC nanopillars injection moulded in that production run. It can clearly be seen to be bending nanopillars at its periphery. Two other cell types were imaged on the same occasion and all showed extensive interaction with the pillared surface. This was only a preliminary test, but further studies are now underway using these nanopillared surfaces.
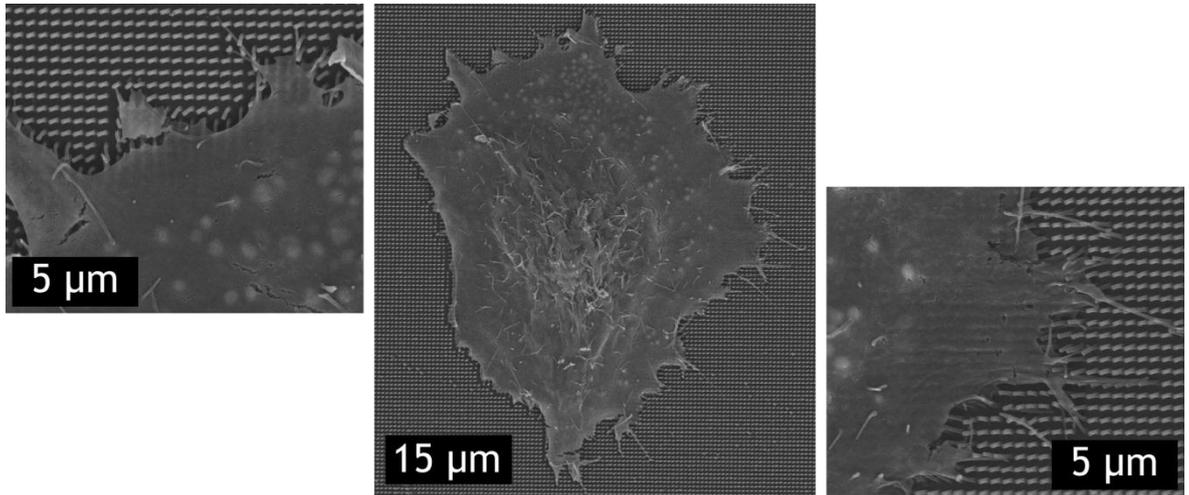
Figure 4.23 - SEM images of an LE2 cell interacting with HAR PC nanopillars fabricated by injection moulding.

Other applications of HAR nanostructures were not directly implemented, although it is likely that most of the structures produced would exhibit hydrophobic properties if water droplets remain in the heterogeneous wetting state (illustrated in Figure 2.19, page 60) where it only touches the tips of nanopillars. Possible gecko toe-hair-like structures were also demonstrated (Figure 4.22) and the process could well be used to form non-reflective pyramidal structures (like those in Figure 1.1, page16) if a suitable stamp can be fabricated and HAR pillar stretching can be prevented (the pointed structure itself may not be conducive to stretching if the tip region provides insufficient *gripping* as discussed above).

4.3.2 Outlook

Overall, the work in this chapter can be considered a success, not only in terms of the successful fabrication of HAR nanopillars, but from the valuable insight and discussion that the many observations made have led to. There are clear needs to investigate the source of inconsistencies on multiple length scales, but cooling time and coating uniformity have been identified as avenues for future investigation and the methods with which to analyse future results are now in place and thoroughly tested. If the kinks are ironed out this successful adaptation of the process developed in Chapter 3 certainly offers a lot of scope for the future of high throughput replication based nanofabrication.

Chapter 5 Injection moulding of microstructures using thermoplastic elastomers

5.1 Outline

5.1.1 Background

Elastomers are a family of polymers which exhibit greater mechanical flexibility than other types of polymer due to the fact that their glass transition temperatures lie below room temperature. Their flexible and elastic properties see them find use in many commercial applications, including clothing, cabling and automotive parts. Thermoplastic elastomers (TPE) form a subset of the group and are useful in situations where the combination of rubber-like properties and application to thermoplastic processing techniques is advantageous. The interest in TPEs in the context of this project stems from the use of other soft materials such as PDMS and hydrogels in the field of cell biology.[43, 126, 131] As described in Chapter 4, elastomeric pillars offer a model for *in vivo* substrate rigidity that can be tuned by the height of the pillars and mechanical properties of the elastomer. [127] When cells adhere to these pillars they exert sufficient force to bend them as shown in Figure 5.1. By measuring the extent of the bending it is possible to determine the magnitude of the forces exerted by the cells if the height and mechanical properties of the pillars are known. As well as being a measurement tool, these pillars cause changes in cell morphology and spreading which correlate strongly with the forces measured as well as influencing and the lineage commitment of stem cells in a predictable way.
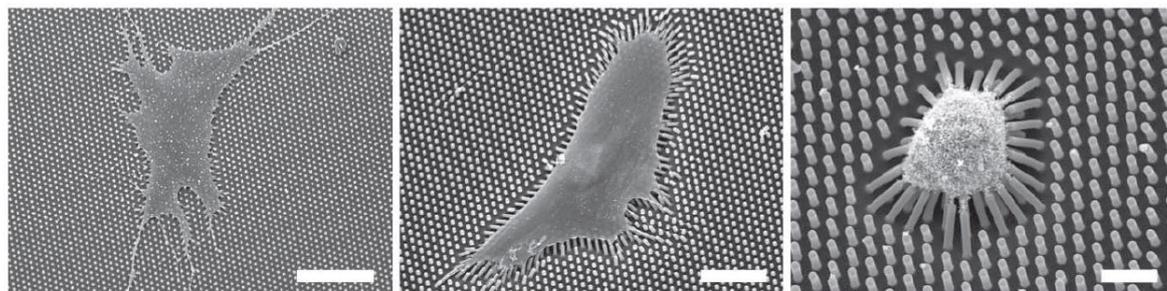
Figure 5.1 - SEM images of human mesenchymal stem cells on PDMS pillars with height (left to right) 0.97, 6.10 and 12.9 μm. Pillar diameter ~2 μm , centre-to-centre spacing = 4 μm. Scale bars = (left to right) 50 μm, 30 μm and 10 μm.. Image taken from [127].

If experiments such as these are to be up-scaled it is desirable to use a high throughput technique like injection moulding that can produce hundreds of samples in one day rather than PDMS casting which can take several hours to from one replica. When the mechanical properties of TPEs are similar to these currently used materials (as in the example above where the Young's Modulus of PDMS was 2.5 MPa) then injection moulding may offer a route to high throughput production of samples that will enable this type of work to be done on a larger scale.

The elastic nature of TPEs, whilst a desirable property in many situations, is also a limitation when it comes to trying to manipulate their shape in a permanent way. Any externally applied deformation, be it a simple prodding or a stretch, will cause stress in the material which will result in a return towards its original shape when the external influence is removed. In the case of a replication based process like embossing or injection moulding this behaviour is manifested in a tendency for newly formed structures to relax and lose some or all of their applied shape to this elastic stress.

In his doctoral thesis,[121] Henrik Pranov compared the success of replicating microstructures by hot embossing and injection moulding with the elastomer Tecoflex (Thermedics Inc. – now Lubrizol), a thermoplastic polyurethane (TPU). The embossing results were more successful than those achieved with injection moulding, leading him to hypothesise that the injection moulded features were subject to greater relaxation after demoulding than those on the embossed products due to the fact the injection moulding process induced a greater stress in the material. To test this he attempted to reduce the stress by lowering the injection speed and found that this did indeed improve results, though not to the extent that the results matched the quality of those made by embossing. He also found that the addition of a non-adhesive coating to the tooling surface to be beneficial to replication, consistent with my own (see Chapter 4) and other results,[108] including those reported by Yoon *et al* [107]. Yoon *et al* also identified increasing tool temperature as a means to improve microstructure formation with a TPU (Texin 990, Bayer). This work, however, found a contradictory relationship with injection speed to that reported by Pranov where faster speeds would slightly enhance replication, an effect which they explained by sheer thinning. In the case of sheer thinning, viscosity is decreased by an increase in sheer stress (applied here by increased injection speed) which may improve filling, but it would be expected that this increased stress would induce greater elastic relaxation after removal from the mould. Perhaps the increased mould temperature (Yoon used 66°C vs. the manufacturer's recommended 16-43°C – Pranov's Tecolflex was moulded with a T_w of 25°C) was sufficient to counteract such effects by inducing a viscosity reduction independent of sheer thinning. Looking at the schematic in Figure 5.2, injected polymer fills a micropatterned mould there will be occasions where regions of polymer which are touching the inlay surface (A & C) are adjacent to regions which are not (B). The differing cooling rates experienced by these neighbouring regions can also induce stress, but Yoon's higher tool temperature could have mitigated this effect (as could the slower cooling rates provided by heat retardant tooling).
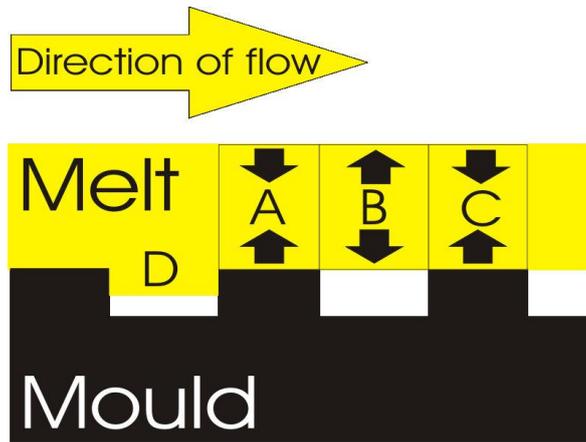
Figure 5.2 - Schematic showing regions of differential cooling as polymer flows over the inlay surface during the filling of a microstructured mould. Image taken from reference [121].

It is not possible to draw direct comparisons between these two works as they used different polymers, equipment and tooling, but they offer a guide to further investigations and a context in which to evaluate future results. They both agree on the widely accepted benefit of non-adhesive surface coatings and point to injection speed as a key parameter for the success of injection moulding microstructures with TPU, while Yoon points to tool temperature as another variable worth considering.

5.1.2 Aims of this chapter

The aims of this chapter are as follows:

- Apply the tooling solution developed in Chapter 3 to the replication of micro- and nanopatterned surfaces with elastomeric materials.

- Establish the minimum feature size that can be replicated with the thermoplastic elastomers under investigation by exploring the effects of specific factors known to affect this such as injection speed, temperature conditions and inlay surface coatings.

- Investigate the conflicting evidence of the effect of injection speed on the replication fidelity of microstructures with TPEs.

- Produce samples containing usable structures equivalent to the PDMS pillars used to modulate substrate rigidity and measure the forces exerted by cells as described above.

- Quantify, analyse and document successes and failures in these pursuits.

5.1.3 Chapter overview

This chapter is primarily concerned with an assessment of the ability of certain TPUs to replicate micro- and nanostructures by injection moulding. It begins with an assessment of the mechanical properties and biocompatibility of three materials, one of which is chosen to be the subject of a systematic study into the effects of injection speed and inlay surface coatings on the replication fidelity of this polymer. Before the results of this study are presented, matters arising from the fabrication of stamps and inlays are discussed and polycarbonate (PC) is introduced as a benchmark for replication fidelity against which to compare the performance of the elastomer. Issues relating to the durability of inlay coatings are also discussed before the study into the effects of injection speed and inlay coatings is finally presented. After this, some attempts to fabricate elastomeric pillars are shown with some consideration given to the effects of melt temperature at this stage. Tool temperature was not assessed in this chapter except to establish that there were practical limitations that prevented it from being altered by any significant amount. The chapter finishes by drawing conclusions about the performance of the TPU and if it can be used, in conjunction with the Cirlex/SU-8/coating tooling, to fabricate elastomeric microstructures for cell engineering and other applications.

5.2 Results and discussion

5.2.1 Evaluation of materials

Three different types of TPU were obtained as a gift from Lubrizol for this investigation. They were Tecoflex EG80A, Estane 58300 and Estane X1393-021 (an experimental grade). For industrial applications the hardness of an elastomer is characterised by a metric known as the Shore hardness which measures the material's resistance to indentation. A rough conversion from Shore hardness to Young's modulus is given by the equation:[132]

$$E = \frac{0.0981(56 + 7.62336S_A)}{0.137505(254 - 2.54S_A)}$$

where E is the Young's modulus in MPa and S_A is the Shore A hardness (the A denotes one of several different Shore scales). This equation was used to compare the mechanical properties of the three TPUs to the type of PDMS used in the instructive biology papers with the flexible pillars (Young's Modulus ~2.5 MPa),[127] the results of which are summarised in Table 5.1.

Polymer	Shore hardness	Approx. Young's modulus (MPa)
Tecoflex EG80A	72 A	6.07
Estane 58300	82 A	10.63
Estane X1393-021	62 A	3.91
PDMS in reference [127]	N/A	2.5

Table 5.1 - Conversion of Shore A hardness to Young's Modulus for three TPUs.

These calculations revealed that Estane X1393 and Tecoflex EG80A were the closest match to the PDMS and, after both performed similarly well in an initial injection moulding test with a micropatterned bulk nickel inlay, a brief test of their suitability for cell culture was performed. Cells were cultured on both substrates by colleagues to assess their biocompatibility, the results of which are shown in Figure 5.3 where the presence of cells is indicated by the blue-purple stain. These results clearly show that for both cell types (labelled *hTERT* and *LE2*), with or without plasma treatment (air, 30 W, 30 s) the Tecoflex did not support cell proliferation and the Estane did. From this it was concluded that Tecoflex EG80A was a less viable material for cell culture than Estane X1393 which would henceforth be used exclusively for the duration of this investigation.
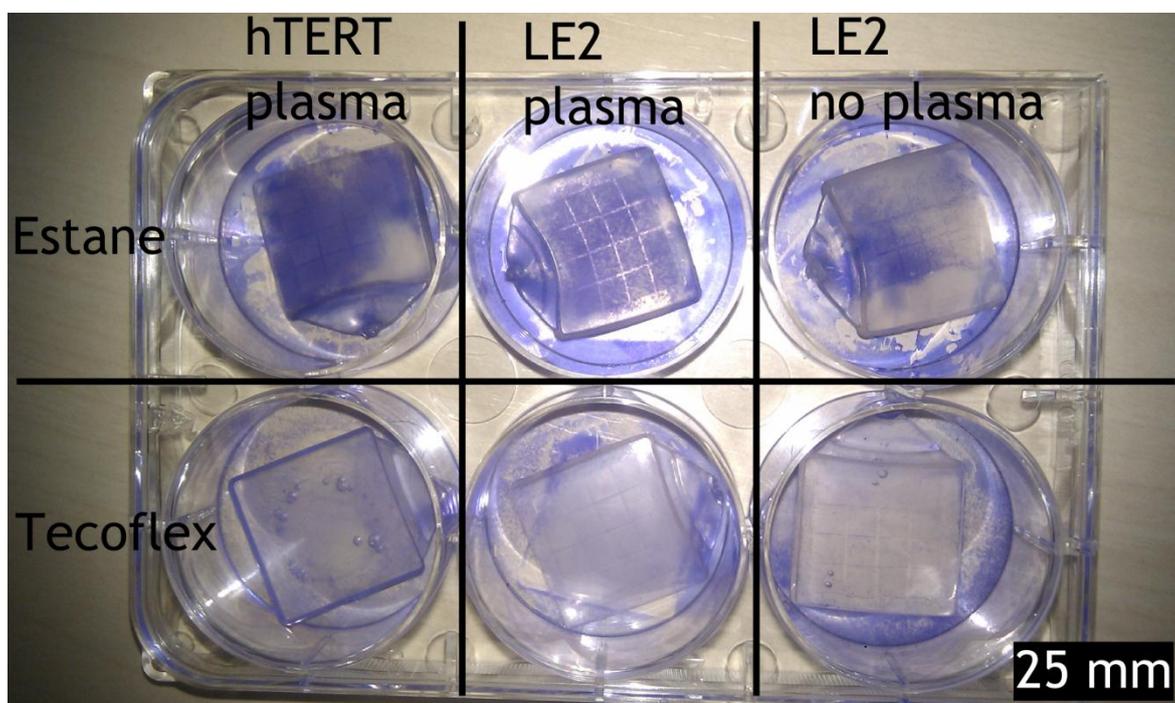
Figure 5.3 - Coomassie (blue) stained cells cutured on TPU substrates after 96 hours. Cell type and surface treatment are indicated along the top, substrate material is indicated to the left.

A further initial injection moulding test was performed with a nanopatterned polymeric inlay containing nanopits to form pillars such as those used for the work described in Chapter 3. Upon ejection, it was possible to observe the nanopattern mediated optical refraction that would be expected from a conventional thermoplastic like PC. Sadly, this effect disappeared within a few seconds, presumably due to the polymer relaxing to a more energetically stable conformation. Subsequent inspection by AFM and SEM showed no evidence that nanostructures had ever been present, leading to the initial conclusion that it was not possible to produce long-lived structures of around 100 nm in size with this polymer. A systematic investigation was then undertaken to establish what is the minimum feature size that can be reliably produced with the TPU. The primary variables for consideration in pursuit of this minimum feature size were chosen to be **injection speed** and **inlay surface coating** due to the apparent importance of these parameters as discussed above. Although the effects of **temperature conditions** were also likely to be important, it was decided that injection speed and surface coating provided enough variables for the first systematic study into this material. Alternate melt temperatures were explored to some degree as will be seen, but certain practicalities, which are discussed in due course, prevented the tool temperature from being altered by any significant amount.

5.2.2 Stamp fabrication

A stamp was fabricated in quartz by EBL (dose = 450 μC/cm^2), metal lift-off (120 nm NiCr) and dry etch (CHF$_3$/Ar, 28 minutes, see section 2.4.3 for recipe) and coated with a non-adhesive fluorosilane layer applied by vapour deposition using the same process as in the previous two chapters and detailed in the methods chapter (section 2.4). The stamp contained a series of ridged patterns all measuring 500 μm in length with widths of 100, 250, 500, 1000, 2500, 5000 and 10000 nm and gap:ridge ratios of 4:1, 3:1, 2:1 and 1:1. The etch depth was 1045 $\pm$ 40 nm as measured by AFM in at least three locations for each line/gap combination. Four Cirlex/SU-8 inlays were created from this stamp by UV-NIL and each was given a different surface coating: trichloro(1H,1H,2H,2H-perfluorooctyl)silane (TPFS) only, 15 nm CVD Si$_3$N$_4$ + TPFS, 15 nm CVD SiO$_2$ + TPFS and 15 nm evaporated Ni + TPFS. These choices were based on emerging evidence from work being conducted for the previous chapter and applied by methods discussed in Chapter 2, section 2.3.

5.2.3 Pattern transfer to inlays

The grating patterns were transferred from the quartz stamp to SU-8 on Cirlex by UV-NIL using pocket imprinter version 3.1 as per the method described in section 2.3.3. During the nanoimprint process features of 500 nm width and below sustained considerable damage (see Figure 5.4), but fortunately a sufficiently large area was successfully transferred to each inlay to allow the experiments to continue. This failing in the imprint process would need to be addressed for any further development of the process. The fact that these failures are concentrated in regions with smaller and more densely packed features suggests that a slightly undercut sidewall profile

unfavourable to demoulding was obtained due to the NiCr mask being too thick, the effects of RIE lag or a combination of the two, but evidence in support of these hypotheses was not sought due to time constrains. Figure 5.4 also indicates evidence of surface cracking of inlays, something which had not been observed previously with this tooling solution. Due to time constraints during preparation it was the case that these inlays were not given the180°C oven bake as directed by the process description in Chapter 2 (section 2.3.3), an omission which may be the cause of these observations.
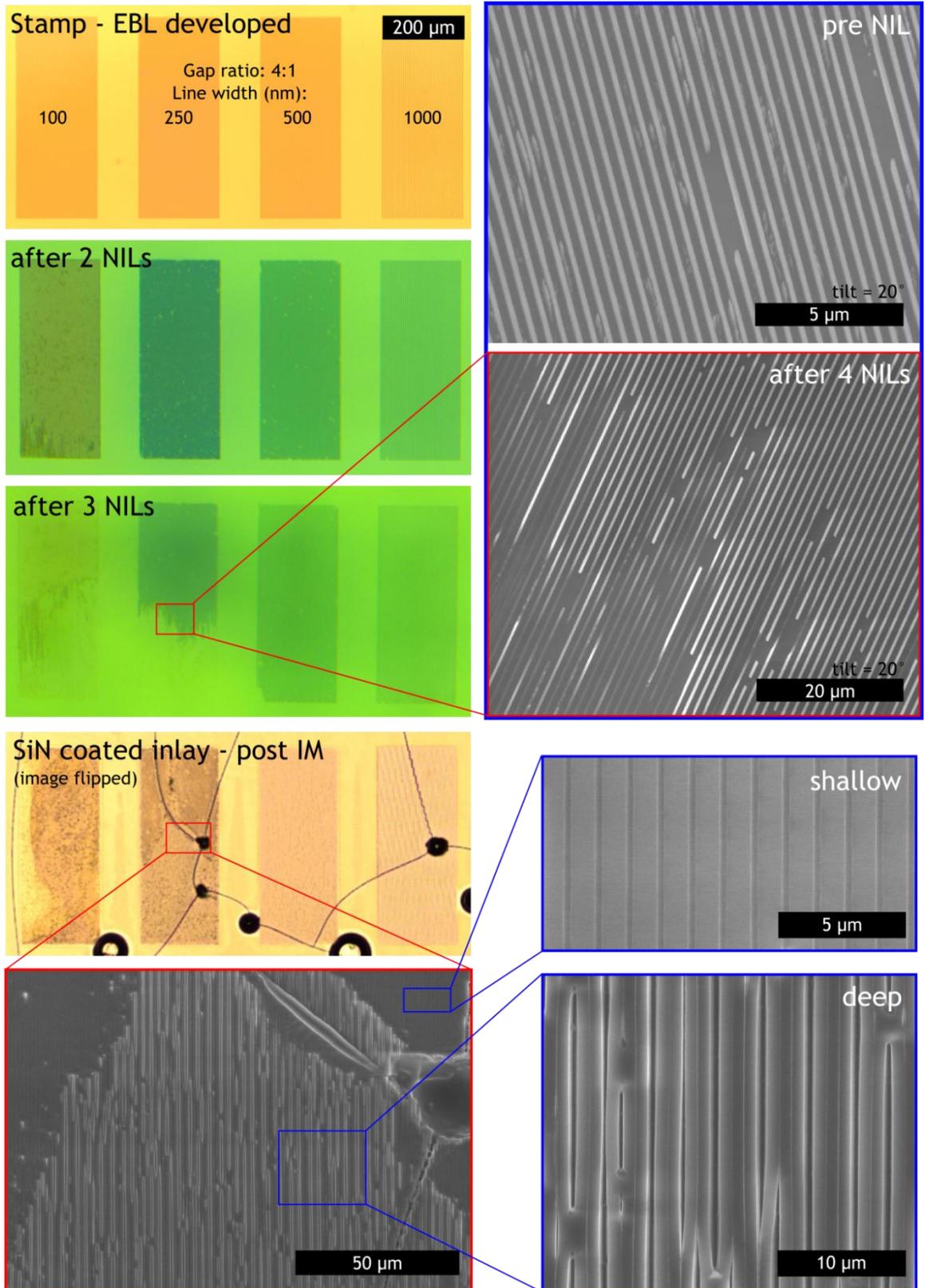
Figure 5.4 - Stamp degradation and pattern transfer to inlay. Optical microscope images showing (top to bottom) the stamp after EBL and development, after the second and third NIL replication, one inlay after injection moulding. Corresponding detail provided by SEM images as indicated.

5.2.4 Polycarbonate as a benchmark material

Due to the high aspect ratio of the narrower features it was not possible to asses imprint depth by AFM. Additionally it was deemed desirable to have results from an exemplary polymer against which to compare the performance of the TPU which could also double as an indirect way to measure inlay depth. Polycarbonate (PC) was chosen for this due to its proven ability to fill nanostructures, even at high aspect ratios, (see Chapter 3 and Chapter 4) and, although it has a tendency to stretch the features under certain conditions, it was the best available option for the task at hand. PC was injection moulded (subsequent to TPU processing) against the three differently coated inlays (Ni coating not used for reasons given in the next section) and the resulting parts measured by AFM to obtain the plots in Figure 5.5. For all inlays height and lateral periodicity were close to that of the stamp for lines of 500 nm width and above. Discrepancies below this value are likely a result of the flawed pattern transfer discussed above and potentially slightly exacerbated by the narrowing of features by the application of the surface coatings. Images of AFM scans are included at the bottom of Figure 5.5 to provide a qualitative appreciation of the typical morphologies of the injection moulded structures compared to the quartz stamp.
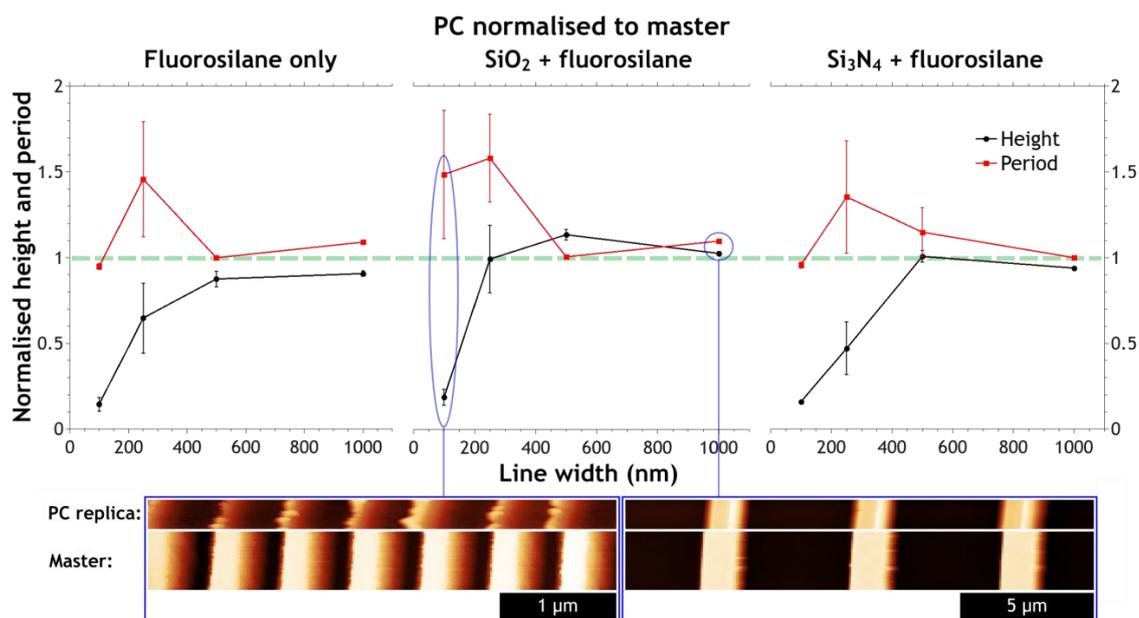
Figure 5.5 – Normalised heights and period of PC lines of various widths injection moulded with three differently coated inlays. Gap ratio = 4:1, heights normalised to master stamp (1045 nm), period = 5 x line width. Tm = 280°C, Tw = 80°C, vi = 50 cm^{3}s^{-1}. AFM scan images provided to give an impression of the shape of features.

5.2.5 Durability of coatings – observations during injection moulding

Perhaps the most important thing to note from a practical operation standpoint is that when injection moulding with Estane X1393 parts do not eject properly. Instead of remaining on the moving platen when the mould opens, the part remains stuck to the fixed side of the tool and

requires manual intervention to remove it. This seems to be primarily due to the end of the sprue not fully detaching from the polymer in the nozzle, but there may also be an element of adhesion to the sprue's internal sidewalls at play. Nonetheless it is a trivial matter to pull them out and, while this reduces throughput and prevents continuous automatic operation, it still only takes around 90 s to produce a part and the majority of that (80 s) is cooling time, which may itself be longer than strictly necessary.

During the injection moulding session a number of important observations were made which have some bearing on the results obtained. Firstly, and most profoundly, the nickel coated inlay suffered immediate catastrophic failure during the first shot, with the majority of the nickel layer delaminating and adhering to the part as the tool was opened. A small amount around the actual features remained on the inlay as did all of that which lay upon the bare Cirlex around the edges, but the entire unpatterned SU-8 covered area lost its coating as shown in Figure 5.6. Clearly, if the adhesion between the polymer and the so called non-adhesive coating is stronger than that between the coating and the mould then the coating material is unsuitable for the task. Because of this, no results with the nickel coated inlays are reported.
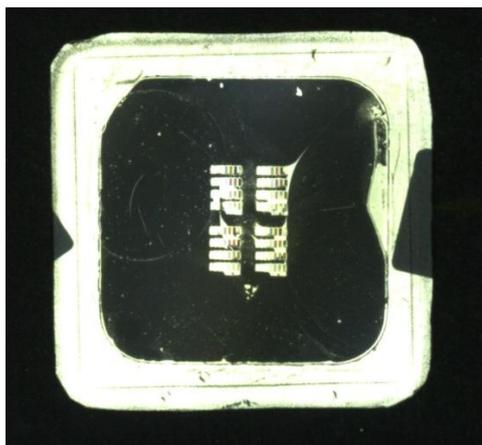
Figure 5.6 - Ni coated inlay after injection moulding attempt. Note the distinct lack of nickel on the SU-8 covered portion of the surface.

Variations in whether the part stuck to the fixed platen or the inlay were also observed for other inlays and are summarised in Table 5.2. In the case of the oxide coated inlay, a residue was observed on the first three parts produced which may have been the oxide coating or just residual unbound fluorosilane being removed from the surface. Parts were also observed to stick to this inlay at all injection speeds in excess of the minimum value of 0.9 cm^3s^{-1}, even at the closest obtainable value of 1.1 cm^3s^{-1}. The inlay where the TPFS was directly applied to the SU-8 also exhibited a change in behaviour where it began to stick to the inlay rather than the fixed platen, although in this case the change was permanent and occurred after 8 shots. The reasons for this change could have been explained by the loss of the non-adhesive coating, but subsequent XPS analysis of the inlay revealed that quantities of fluorine (17.1%) remained on the surface which

were comparable to that on the nitride coated inlay (16.7%) for which parts did not adhere to the inlay under any conditions.

Inlay coating	Adhesion to inlay	Comments
Nickel + TPFS	Always	Coating removed
SiO$_2$ + TPFS	At $v_i > 0.9$ cm^{3}s^{-1}	Residue observed on parts during first three shots
TPFS only	After 8 shots	
Si$_3$N$_4$ + TPFS	Never	

Table 5.2 - Observations relating to inlay performance when injection moulding with Estane X1393

Observation of the bulk shape of injection moulded TPU parts reveals a significant amount of bending in their resting states (see Figure 5.7.) which is indicative of the elastic stress built up within the material. This could impede their usefulness as substrates for cell biology by making microscopy difficult, although it should be possible to devise a way to force them into a flat position for the duration of an experiment. No attempt was made to quantify this bending or relate it to processing parameters.
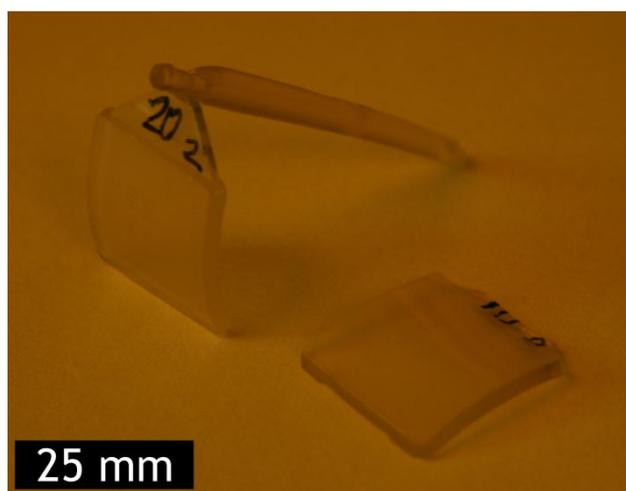
Figure 5.7 - Injection moulded parts made from Estane X1393 with and without sprue.

5.2.6 Minimum feature size assessment

SEM imaging of injection moulded TPU parts revealed that reproduction of the microstructures was achieved, but all features displayed significant rounding at the corners compared to the stamp and PC replicas. Furthermore all ridges below 500 nm were poorly defined and showed signs of lateral relaxation (see Figure 5.8). As discussed above, the inlays are imperfectly fabricated and do not exhibit regular uniform grating patterns as intended, but there is still a stark difference between the ways both the good and bad elements of these patterns are replicated in TPU and PC.
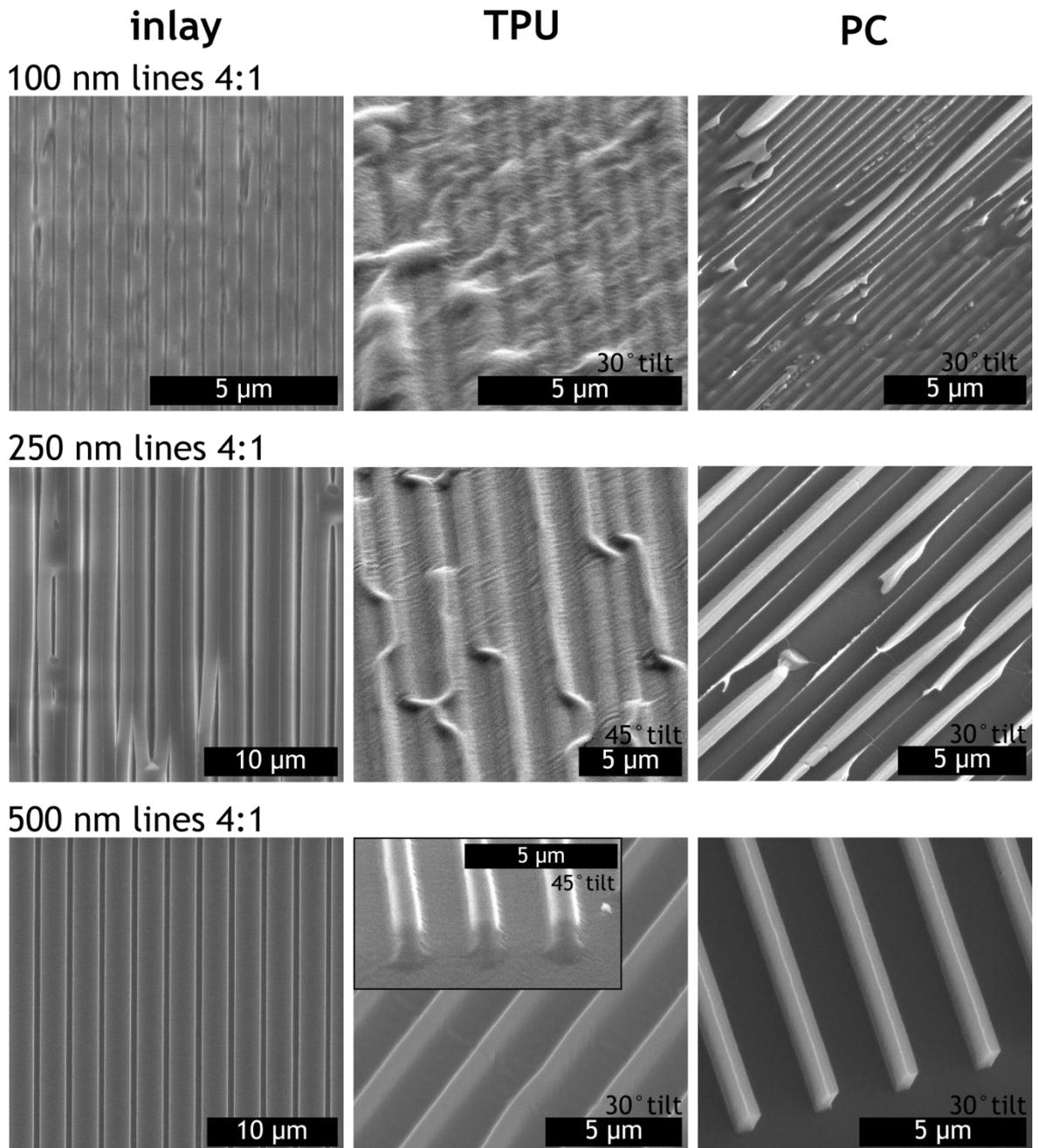
Figure 5.8 - SEM images of inlays and corresponding replicas made of TPU and PC with gap ratio 4:1.

AFM measurements were used to characterise injection moulded TPU parts in terms of the heights and lateral periodicity of the structures produced. Figure 5.9 shows how these dimensional quantities, normalised to both the stamp and the corresponding PC replicas, are affected by diminishing feature size. It is thought that normalisation provides the fairest and neatest way to compare to compare dimensions given the variation in height for low line widths and intrinsic differences in period for different line widths. As is to be expected in light of the SEM evidence presented in Figure 5.8, serious discrepancies begin to arise at line widths below 500 nm with normalised heights severely reduced and both quantities becoming increasingly variable as indicated by the standard error bars. These variations can be partly explained by the irregularities in the inlay, but the fact that there is also significant deviation from the PC replicas in addition to

the clumping evident in the SEM images (which will affect both height and periodicity) suggest a definite threshold of somewhere just below 500 nm as the minimum size limit for the fabrication of these type of structures with this material under these conditions.
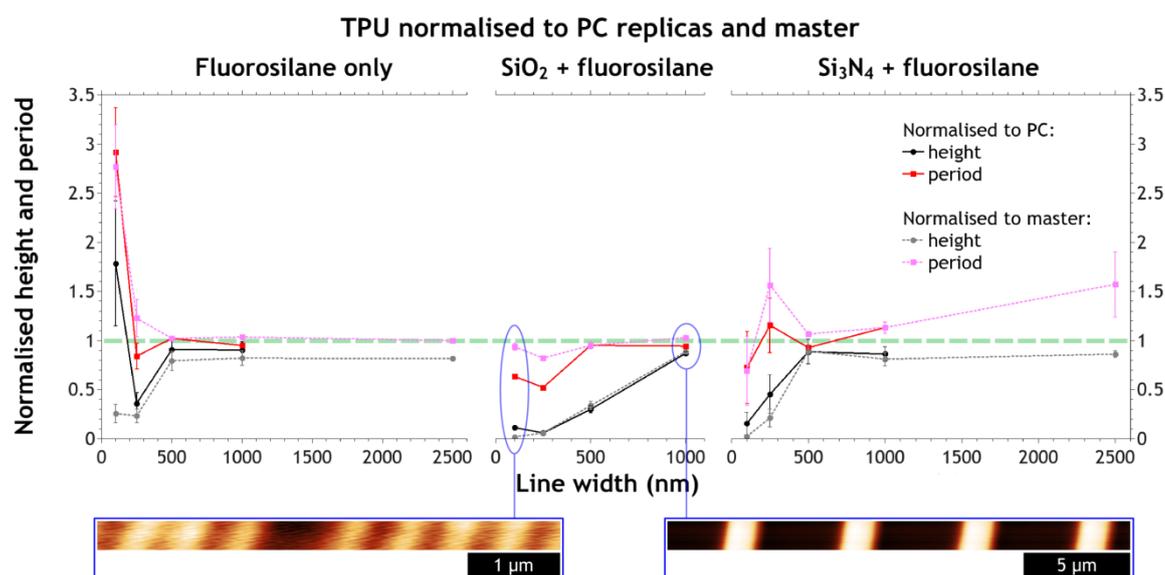
Figure 5.9 – Heights and periodicity (normalised to stamp and PC replicas) of features of different line widths produced in TPU using inlays with 3 different surface coatings. T_m = 190ºC, T_w = 20-25˚C, v_i = 0.9 cm^{3}s^{-1}, gap:ridge ratio = 4:1. AFM scan images provided to give an impression of the shape of features.

In comparing the inlays, it is evident that the Si_3N_4 and silane-only inlays perform significantly better than the SiO_2 inlay overall, a result that might be expected if the residue observed on the first few moulded parts was indeed the oxide coating being removed. The notably smaller error bars produced by this inlay are perhaps suggestive of a uniformly poor filling, compared to the other two which may have allowed their deeper features to be filled when the opportunity presented itself - implying that larger error bars at low line widths indicate improved polymer performance.

The other important dimensional variable to consider is the gap between the features. Due to the apparent relaxing of TPU, it seemed likely that features spaced closer together might be less well defined compared to those spaced further apart. Figure 5.10 shows comparative SEM images of the nitride coated inlay alongside TPU and PC replicas at two line widths: 1 μm, where the replication at a gap ratio of 4:1 is reliable, and 500 nm, a value at or near the accurate replication limit of the TPU. Again, there are signs of inlay damage and evidence that the ridged structures are having trouble supporting themselves at 500 nm line width. In addition to rounded corners, TPU replicas show signs of ridges clumping together with their neighbours, even at 1 μm on occasion, and PC replicas indicate that line widths may be substantially thinner than intended at the base of the 500 nm pattern in the inlay. There is also evidence of 1 μm PC lines leaning over in a similar way to the pictured 500 nm lines on the inlay.

inlay   TPU   PC

500 nm lines 1:1

30°tilt   5 µm   30°tilt   20 µm   30°tilt   5 µm

1000 nm lines 1:1

30°tilt   5 µm   15 µm   45°tilt   45°tilt   50 µm   30°tilt   10 µm
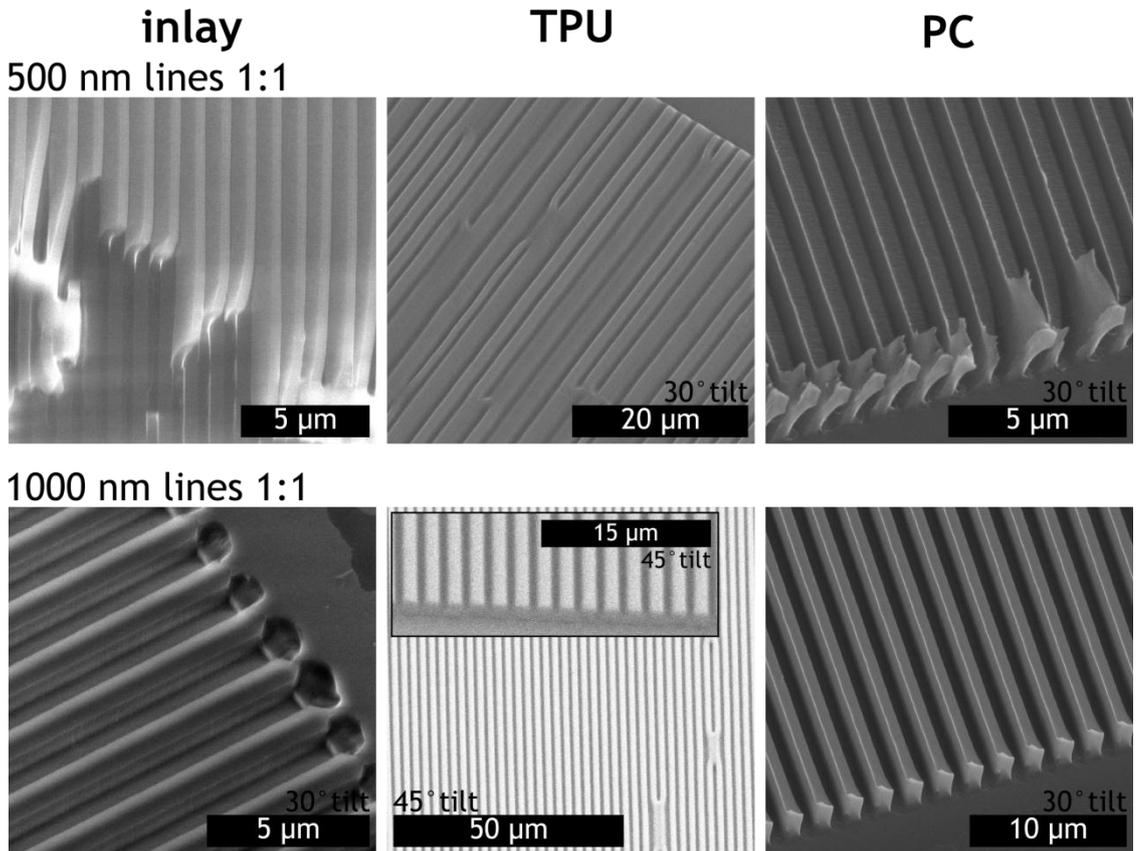
Figure 5.10 - SEM images of inlays and corresponding TPU and PC replicas with gap ratio 1:1.
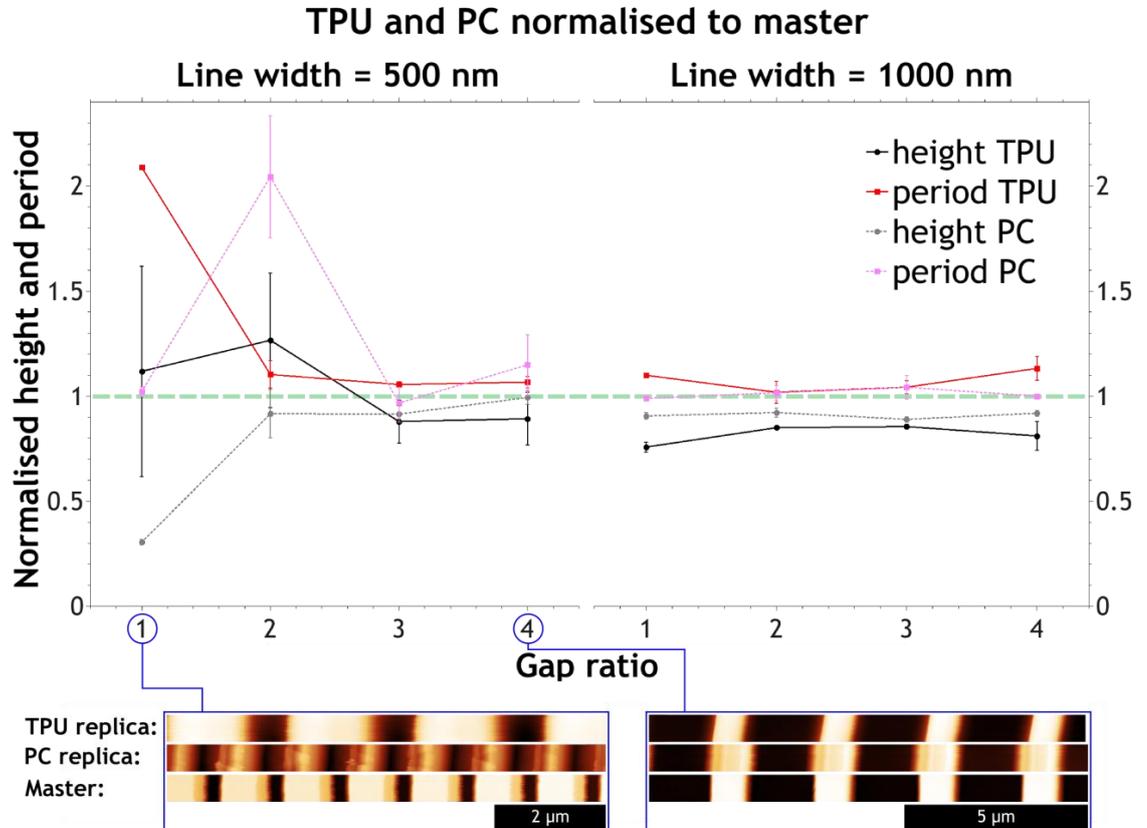
Figure 5.11 - Effect of diminishing gap ratio for on coating at 500 nm and 1000 nm line widths. T_m = 190°C, T_w = 20-25°C, v_i = 0.9 cm³s⁻¹. AFM scan images provided to give an impression of the shape of features.

Figure 5.11 compares the normalised height and periodicity of TPU ridges across the range of gap: ridge ratios with PC results provided for comparison as are AFM scans relating to certain conditions. Both polymers appear to perform fairly well and consistently across all gap ratios for 1 µm line width, but in line with the SEM evidence the diminishing gap ratio has detrimental consequences at 500 nm line width. The roughly doubled periodicity at 1:1, clearly observable in the corresponding AFM scan, is a result of neighbouring ridges sticking to each other as seen in the SEMs of Figure 5.10. The very low value for PC replica height at 1:1 and the corresponding highly variable value for the TPU may be due to the leaning over and/or breakage of ridges on the inlay. This is a strong indicator that, while the Cirlex/SU-8 tooling solution may work well for nanoscale pillars (see Chapter 3 and Chapter 4), it may require some considerable refinement to be applied to the fabrication of the type of grating structures used here.

In Chapter 3 it was observed that the injection speed had little effect on the formation of nanostructures in PC, but other works[107, 121] have shown this to be an important parameter with elastomers. The plots in Figure 5.12 show how injection speed affects feature heights and periodicity for the three differently coated inlays at line widths of 500 and 1000 nm (gap ratio 4:1). At the larger feature size, both height and periodicity appear to be quite independent of injection speed, but for 500 nm line width we do see results consistent with those observed by Pranov which indicate that the depth of filling is indeed improved by a reduction in injection speed. The results are different for the three inlay coatings, with the nitride achieving superior filling overall and the oxide showing no change whatsoever, lending further weight to the possibility that the coating was removed. However, it is clear that the minimisation of injection speed allows the nitride and TPFS-only inlays to facilitate almost the same depth of filling with TPU as with PC.
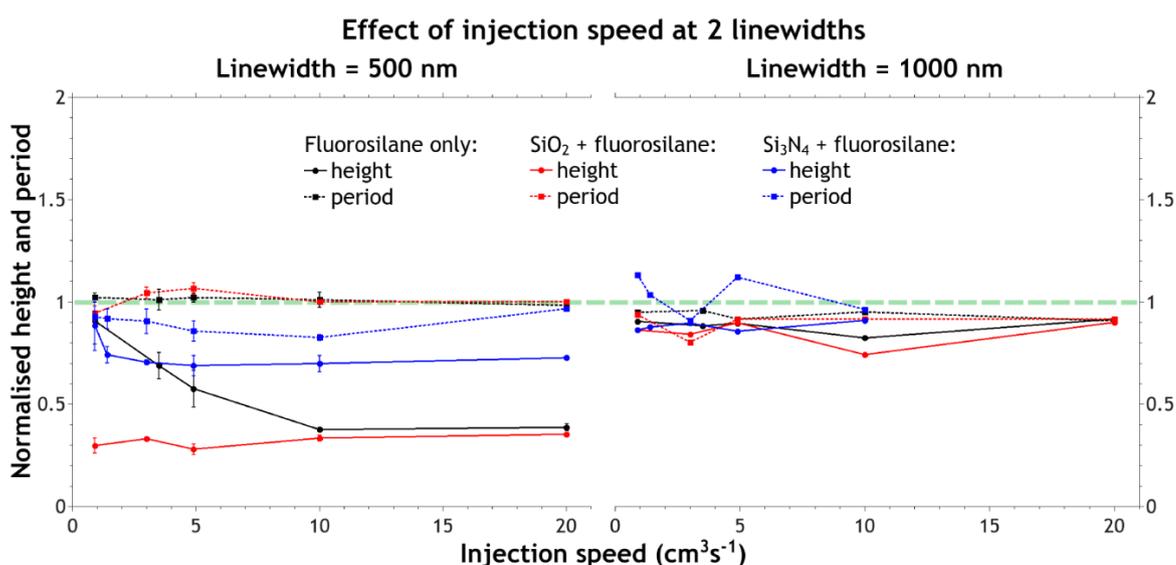
Figure 5.12 - Effect of injection speed on heights and periodicity (normalised to PC replicas) of TPU features for two feature sizes with three surface coatings. T_m = 190°C, T_w = 20-25°C, gap ratio = 4:1.

It was mentioned earlier that tool and melt temperatures may play a role in enhancing the replication quality of TPUs. In all of the above results the temperatures were set as per the manufacturer's guidelines with melt at 190°C and the tool water cooled to between 20 and 23°C. A set of results was obtained using the Si_3N_4+TPFS inlay with the melt temperature raised to 200°C, but this showed no significant variation from the results obtained at 190°C across all metrics studied above. Attempts were also made to use a raised tool temperature but upon heating from 30 - 50°C any attempt to run a shot resulted in the sprue breaking part of the way along its length during the normal manual part removal. Occurrences such as this require careful and time-consuming removal of polymer from the injection channel and so, whether it was a problem inherit to our injection moulding machine or the polymer itself, this avenue of inquiry was pursued no further.

5.2.7 Injection moulding of elastomeric pillars

Having established a lower limit to the size of straight lines that could be produced by injection moulding with Estane X1393, attempts were made to fabricate pillars at and near this size range (500 nm), as well as slightly larger ones that might serve a useful purpose in the type of biological experiments described at the beginning of the chapter. Two micropatterned inlays were used. They were fabricated by the same method as in the size limit experiment and coated with 15 nm of ICP deposited Si_3N_4 and a monolayer of vapour deposited TPFS.
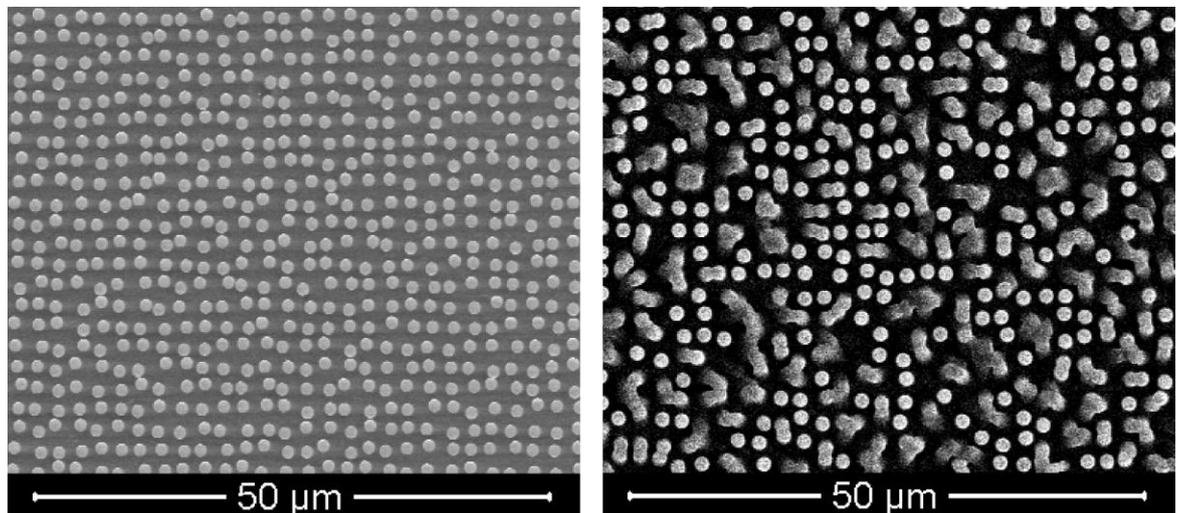
Figure 5.13- SEM image of the 1.2 μm circles on pattern 1 on (left) the quartz stamp and (right) TPU replica. The disordered pattern occasionally results in neighbouring circles making contact with each other, particularly in the TPU.

Pattern 1 consisted of arrays of circles with diameters of 2.1, 1.2 and 0.6 μm etched to a depth of 2 μm. The circles were placed slightly off centre from a regular square grid by a random amount for the purposes of a colleague's unrelated experiment which meant that some of the circles were

joined on the stamp and inlay (see Figure 5.13). Success rate (as described in Chapter 4 and methods section 2.6.2) was calculated and normalised to that of the stamp, the results of which are presented in Table 5.3. Injection moulding conditions for pattern 1 were constant at $T_m = 190$ºC, $T_w = 20\text{-}23$ºC, $v_i = 0.9$ cm^{3}s^{-1}. The height of replicated features was not measured, not even by tilted SEM, due to time constraints.

Pillar diameter (µm)	Success rate (%)
2.1	97.7
1.2	94.4
0.6	0

Table 5.3 - Success rate of injection moulded TPU micropillars (pattern 1) for different feature sizes.

Pattern 2 consisted of arrays of circles with diameters of 2, 1 and 0.5 µm positioned on a square grid with a gap:diameter ratio of 1:1 for all diameters and an additional gap:diameter ratio of 2:1 for the 0.5 µm pillars. The etch depth of the stamp was 5 µm. Having not yet investigated the effects of lowering temperature below the manufacturer's guideline value of 190ºC it was decided to use this opportunity to see if the reducing the value of the parameter would make any difference to replication. The results of this brief investigation are presented in Table 5.4 and pictorial examples of typical results are shown in Figure 5.14. For all temperatures injection speed was set to the minimum value which resulted in an actual value of 0.9 cm^{3}s^{-1} except at 180ºC where the actual value was 1.2 cm^{3}s^{-1}.

Pillar diameter (µm)	Melt temperature (ºC)	Pillar height (µm)	Comments
2	180	4 - 5 µm	Pillars occasionally lean and adhere to neighbours
2	190	4 - 5 µm	Pillars occasionally lean and adhere to neighbours
2	200	4 -5 µm	Most pillars not replicated
≤ 1	180,190 & 200	stumps	No successful pillars

Table 5.4 - Summary of physical characteristics of injection moulded TPU micropillars (pattern 2). Height measurements are rough values measured from tilted SEM images.
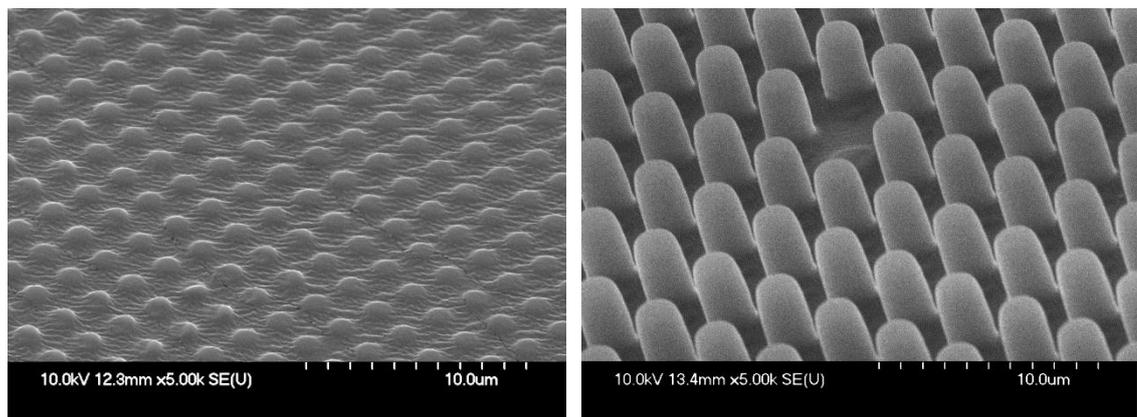
Figure 5.14 - SEM images of micropillars injection moulded with Estane X1393. Left: diameter = 1 µm, T_m = 180ºC. Right: diameter = 2 µm, T_m = 190ºC. Viewing angle ~ 45º.

The successful replication of 2 µm pillars with both patterns is encouraging, but not surprising in light of the results of the minimum feature size study in which 1:1 lines were replicated well down to 1 µm, although that test did not attempt to replicate structures as tall as these (only 1 µm height compared to 5 µm of pattern 2). The fact that 1 µm pillars were not replicated on pattern 2, but 1.2 µm pillars had 94.4% success rate on patter 1 is unusual, but without height data any analysis is speculative. It might, however, be worth speculating that there is a critical size limit intrinsic to the TPU between 1.0 and 1.2 µm below which it cannot fill, or will not retain the shape, of pillars in the same way that there appeared to be a critical dimension around 500 nm for lines. Circles

provide a more difficult shape to fill so it does make sense that if there is a minimum size limit then would be higher for circles than long grooves.

The effect of melt temperature is also interesting, despite the fact that the only evidence is qualitative. The fact that the majority of 2 μm pillars on pattern 2 failed to replicate at $T_m = 200$ºC, but the majority succeeded at 190ºC and 180°C lends weight to a phenomenon discussed in the introduction of this chapter (Figure 5.2). In that section it was postulated that an increase in feature filling[107] could have been attributed to an increase in the tool temperature well above the manufacturer's recommended conditions. This would have the effect of reducing the temperature difference between melt and tool, thereby reducing the stress induced between regions of the melt passing above cavities and adjacent regions passing over the flat inlay surface where the rate of cooling will be greater. If this is indeed the case then a reduction in the melt temperature would have a similar effect and raising it would result in the opposite: an increase in stress around features and therefore a greater elastic relaxation after part removal. Contrary to this hypothesis however, is that no noticeable difference was observed between replication with $T_m = 200$°C and 190ºC with the Si_3N_4+TPFS size-limit inlay (results not shown, but mentioned earlier), but as already stated, the structures are very different so the effects may not have been noticeable. It is also the case that the heat retardant Cirlex/SU-8 tooling would heavily mitigate these effects anyway just as it vastly increases the freezing time of PC. Whatever the case, it is possible to replicate 2 μm pillars with 4-5 μm height and 1.2 μm pillars with enough height to make for good contrast in a top-down SEM using Estane X1393, and if a way can be found to increase the tool temperature without inducing sprue breakage then the effects of temperature could be conclusively investigated.

5.3 Conclusions

5.3.1 Success in achieving the chapter's aims

The tooling solution developed in Chapter 3 has once again been adapted to a different process with relative ease. The only real problems occurred at the NIL stage, as in the previous chapter, and it is expected that it is likely to be an etch-based artefact that delivered an unfavourable profile and could be righted by a small amount of optimisation. Elastomeric micropatterns were fabricated with success for all except 1 μm diameter pillars, but nanostructures proved to be more of a challenge. It was also the case that moulded parts had to be manually removed after every cycle and although this negates the possibility of a fully automated process, it is still relatively fast compared to other replication based microfabrication techniques.

A minimum feature size attainable with Estane X1393 TPU was established to be somewhere between 250 nm and 500 nm for linear structures with a 4:1 gap:width ratio and between 500 nm

and 1000 nm for a 1:1 gap:width ratio. A minimum size of between 1 μm and 2 μm was also just possible for circular pillars. Si_3N_4+TPFS was clearly the most effective inlay surface coating, delivering ~ 70% filling of 500 nm lines, even at $v_i = 20$ cm^{3}s^{-1}, although at lower speeds it did not seem to perform significantly better than TPFS-only. Below these limits it is not the case that no structure if formed, but they are badly defined, spread out and never more than 10s of nm in height. The feature size test was somewhat hindered by stamp/inlay failure at the smaller line widths and gap ratios, but the features that remained still provided conclusive evidence of the resolution limit.

Reduced injection speed was shown to improve filling of linear structures for fluorinated Si_3N_4 and TPFS-only inlay coatings, but SiO_2 may have been damaged during injection moulding and Ni coatings definitely were. It was shown that increased melt temperature can make it harder to fill 2 μm circular pillars, but it was not possible to investigate tool temperature although it is suspected that raising this could improve filling if practical limitations of equipment can be overcome.

5.3.2 Outlook

Having established the limitations with Estane X1393 under certain fixed conditions (T_m, T_w, equipment) it would next seem sensible to try to vary these in a systematic way to further push the boundaries of what is possible with this material. This might not be possible with the injection moulding machine used in this work, but one with a lower range of injection speeds and a tool designed specifically for elastomers may produce better results. It would also be interesting to perform the same minimum feature size test with one or more slightly harder TPUs to see if are able to form smaller structures.

The structures that were successfully fabricated, particularly the circular pillars, could be used in experiments to modulate the rigidity of substrates and measure the forces exerted by cells in place of PDMS pillars used previously.[126, 127] While a fully automated process was not achieved, the throughput of micropatterning the TPU Estane X1393 by injection moulding using coated Cirlex/SU-8 inlays is a promising method for fabricating large numbers of micropatterned elastomeric samples for whatever applications may require them.

Chapter 6 Conclusions

6.1 Success in achieving the aims of this thesis

Having presented the background, motivations, methods, work conducted, results obtained and the analysis of these, this chapter is devoted to drawing conclusions and summarising results. Below, the aims presented at the end of the introduction are reprinted (in bold type) followed by an evaluation of the extent to which that aim was achieved.

Develop enabling fabrication techniques to augment the existing selection of nanofabrication processes available for the nanopatterning of thermoplastic polymers. Achieve this through reliable, consistent and repeatable fabrication process, using standard nanofabrication materials and equipment (such as those found in the JWNC) wherever possible.

The methods developed in this project and reported in this thesis do indeed augment the existing toolbox of nanofabrication techniques. The foundational tooling solution developed in Chapter 3 is capable of closely replicating nanoscale pillars with the option of stretching them by simple adjustment of process parameters, with tool temperature providing the most clear control of this. This process is reliable, consistent and repeatable and although a build-up of polymer residue was observed (Figure 3.17, page 81) this can be accounted for by the occasional cleaning of inlays or addressed by the addition of non-adhesive surface coatings such as those tested in Chapter 4. Aside from Cirlex substrates, all the core materials used (quartz, PMMA, SU-8, TPFS) were standard micro/nanofabrication materials present in the JWNC before the inception of this project, and Cirlex itself is relatively cheap (~£140 for 1 m^2) and easy to obtain. The patterning of surfaces was realised by standard processes such as photolithography, EBL, metal deposition and dry etch with only the custom NIL/embossing tools and the injection moulding machine falling outside the bracket of standard fabrication tools. As such, the bulk of the inlay fabrication process could be conducted in any nanofabrication facility and any equipment related short comings could be readily outsourced.

Utilise injection moulding as a means to apply these enabling techniques to the high throughput mass replication of high quality nanopatterned samples.

Injection moulding was, with the exception of the elastomer (Chapter 5), utilised in the way it was conceived, as a high throughput fully automated replication process. With no attempt being made to optimise cycle time it is still possible to produce 1000 replicas in one day using the tooling solution developed in this project. The quality of nanopatterned samples was variable in some instances, particularly for high aspect ratios. The large systematic study of inlay coating performance in Chapter 4 revealed a great deal of variability which was the main subject of a lengthy discussion (pages 102-112). This was, however, balanced by some highly consistent

results for similar structures in smaller studies and, by comparing the two, variation in cooling time was identified as a likely cause and promising route of investigation to determine a solution to the problem.

Implement a solution to the problem of incomplete mould filling of raised nanostructures (i.e. pillars). This must be integrated with our injection moulding equipment with as few modifications as possible, therefore a heat retardation method (rather than a variothermal method) would be preferable.

The problem of mould filling was fully addressed by the hybrid Cirlex/SU-8 tooling. By exploiting the thermally insulating properties of these materials, injected polymer was able to fill and replicate nanostructures that were not possible with nickel tooling (Figure 3.5 and Figure 3.6, page 73). Hybrid Cirlex/SU-8 inlays required no alterations to be made to injection moulding equipment other than the machining of a simple steel back plate to ensure a snug fit for the inlay in the frame. Due to the success of this tooling solution a variothermal method did not need to be considered.

Develop methods which are versatile, adaptable and applicable to as many applications as possible. Potential adaptations may include the size, shape and aspect ratio of nanostructures, the materials used and different tool configurations. It is not feasible to address directly any and all potential applications, but a short list to keep in mind would be: non-reflective surfaces, non-wetting surfaces, dry adhesive surfaces and, in particular, nanostructured surfaces for cell-substrate interactions. The potential to expand this to nanopatterned implantable materials would also be beneficial.

The hybrid Cirlex/SU-8 tooling solution developed in Chapter 3 proved itself to be adaptable to the goals of the following two chapters. It was also shown to be flexible within the scope of that chapter by facilitating the patterning of inlays by both photolithography and UV-NIL, as well as lending itself to some basic multiscale patterning using thin patterned films on top of larger structures to superimpose nanopatterns onto an underlying topography. One of the core advantages of the Cirlex/SU-8 inlays is that they can be patterned in a variety or combination of ways with the utilisation of UV-NIL (SU-8 also offers the potential for hot embossing) as the primary means of inlay patterning. It allowed the translation from low to high aspect ratio structures in a relatively seamless way (Chapter 5), and is amenable to patterning by virtually any structure that can be fabricated with the physical profile requirements of a stamp with 10 nm resolution or below.[52, 54]

Although some problems were encountered in translating the tooling solution to high aspect ratio pillars (Chapter 4, page 90) and linear structures (Chapter 5, page 126), the cause of the former case was identified, characterised and solved, while the latter did not fully impede the gathering of

results and could likely be addressed in future work by similarly optimising the etch profile of the stamp.

In terms of the cited applications in the aims (non-reflective surfaces, non-wetting surfaces, dry adhesive surfaces, surfaces for cell-substrate interactions), the techniques developed in this work offer potential to facilitate all of these, particularly through the extension to high aspect ratio nanostructures. The only one that has been realised is the cell biology application, but this was the primary application in mind and has been realised in each of the three experimental chapters. The rather ambitious extension to implantable materials mentioned in the aim has not been attempted, but the experience gained in this project could certainly inform the development of means to meet that end.

Fabricate surfaces to be used by biologists tailored to their needs as closely as possible.

Surfaces for the study of cell-substrate interactions have been fabricated in all three experimental chapters. The samples are constructed of an appropriate size and shape for tissue culture labware and, with the exception of the TPU samples, are suitably flat for the purposes of optical microscopy. The low aspect ratio surfaces from the initial development in Chapter 3 have been in use by biologists within the university for around two years at the time of writing and the HAR pillars developed in Chapter 4 have been briefly demonstrated here and are currently being used by external partners. The elastomeric pillars from Chapter 5 could do with some refinement in terms of the reliability of the minimum attainable feature size, but if 2 µm diameter pillars with a height of 4 or 5 µm are suitable and they can be made to sit flat in a tissue culture dish, then they are ready to be used.

Attempt to fabricate demonstrators of non-reflective, non-wetting and dry adhesive surfaces.

This was not attempted although it is likely to be the case that many of the structures fabricated in this project (particularly HAR pillars) will exhibit superhydrophobic properties due to their low effective surface area. Hair-like structures similar to the tips of gecko toe pads were presented as a potential route to dry adhesive applications (Figure 4.22, page 115), but the complex hierarchical characteristics of these natural structures[20] mean that the realisation of this would require considerable development. Non-reflective surfaces should be relatively simple to implement if the stamps can be made, with the only anticipated problem at the injection moulding side being the stretching of structures away from their carefully designed intended shape.

Quantify results at all stages of process development to enable analysis and refinement of techniques.

Results were quantified wherever possible through the analysis of SEM, AFM, WCA and XPS data. This led to detailed analysis which shed light on the processes under investigation and enabled conclusions to be drawn and extensions to the work proposed. Inevitably, the drawing of some conclusions was left wanting for further evidence, but these could not have been so easily identified without the well structured scrutiny of others.

Document the successes and failures in the pursuit of these aims. Process details should be accurately recorded to enable the work to be built upon in future.

This thesis is intended to be a concise, clear and complete record of the work performed, analysis conducted and conclusions drawn. It details all relevant motivations, methods, results and analytical rationale and provides illustrations and references to further the clarity of these wherever possible.

6.2 Summary

A recent review[133] highlights three key areas amongst many in the field of nanostructured biomaterials that require attention: anti fouling materials, the cell-materials interface and high throughput processing. The processes developed in this project directly address the latter, are primarily motivated by the second and provide means to address the former amongst many others, making this work highly relevant to the current demands of today's biomaterials research.

This thesis has presented the development of an enabling technology which not only directly addresses the needs of cutting edge cell biology research, but also serves to expand the toolbox of nanofabrication techniques in general and has the potential to lend itself to the realisation of superhydrophobic, non-reflective, anti-fouling, dry adhesive surfaces and many other applications besides. As well as facilitating the current demand for nanostructured polymers, these techniques look forward to future applications and up-scaling through their intrinsically high throughput nature and are realised through well-established materials and industry standard equipment which will serve to further ease this transition.

Appendix: Production of a successful nanopatterned poly(carbonate) part by injection moulding - full process summary

	Process	Technical parameters	Remarks
1.0	**Stamp fabrication**		
1.1	Clean and dehydrate 25 x 25 mm piece of polished quartz	In ultrasonic bath immerse in acetone, methanol and IPA for 5 minutes each, then dry with N_2. Dehydration bake in oven: 1 hour 180 at 180°C	
1.2	Layer of PMMA 2010	Deposit with pipette to cover sample. Spin to desired thickness according to resist specification. Oven bake for 20 minutes at 120°C	Ensure layer is at least 50 nm thicker than metal layer to be deposited in step 1.8.
1.3	Layer of PMMA 20141	Deposit with pipette to cover sample. Spin to desired thickness according to resist specification. Oven bake for 20 minutes at 120°C	Ensure layer is roughly double the thickness of the metal layer to be deposited in step 1.8.
1.4	Charge conduction layer	Deposit 10 nm Al by electron beam evaporation.	
1.5	Pattern definition by EBL	Write pattern using electron beam lithography tool.	e.g for 100 nm dots with 500 nm pitch in approx. 300 nm total resist thickness: dose = 170 μCcm^{-2}. Patterns may also be defined by other lithographic processes using different resists etc. if desired.
1.6	Remove charge conduction layer	Immerse in 49:1 RO water:TMAH for 2 minutes. Rinse in RO water for 30 s and dry with N_2.	
1.7	Development	Immerse in 2.5:1 MIBK:IPA for time (minutes) = 0.3 x total resist thickness (nm). Rinse in IPA for 30 s and dry with N_2.	
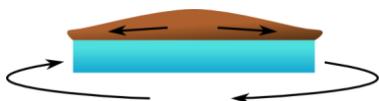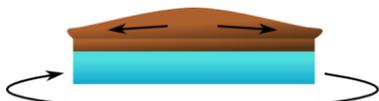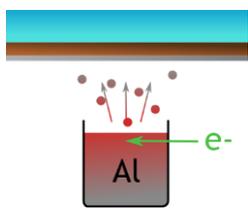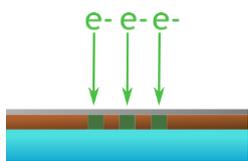
1.8	Metal deposition	Deposit NiCr by electron beam evaporation. Thickness (nm) = 0.1 x desired etch depth (nm).	
1.9	Metal lift-off	Immerse in acetone at 50°C for 30 minutes. Spray with fresh acetone for 10 s. Rinse in IPA for 15 s and dry with N_2.	Ultrasonic bath may help to remove stubbornly adhered NiCr, but may also cause features to become detached.
1.10	Dry etch	Etch to desired depth with RIE tool. Suggested recipe (etches 37-40 nm/min): gasses = CHF_3/Ar, flow rate = 25/18 sccm, pressure = 30 bar, temperature = 20°C, RF power = 200 W.	Etch profile must not be undercut. Ideal profile for NIL (steps 2.5-2.7) is ~5° from vertical.
1.11	Hard mask removal	Immerse in Cr etch for 3 minutes. Rinse in RO water and dry with N_2.	
1.12	Deposition of non-adhesive layer	Expose to O_2 plasma for 1 minute at 200 W. Place sample in petri dish on hotplate at 150-200°C beside a small drop (approx. 50 μl) of TPFS solution for 15 minutes. Rinse in RO water, acetone and IPA, then dry with N_2.	
	End of process.	Stamp fabrication complete	
2.0	**Inlay patterning**		
2.1	Obtain Cirlex substrate	Cut out a piece of 740 μm thick Cirlex from sheet so that it will fit into the injection moulder frame (see step 3.5). In this project sample dimensions were 24 x 24 mm with a corner radius of 3 mm.	Scissors or automated machining tool may be used.
2.2	Clean Cirlex substrate	In ultrasonic bath immerse in acetone, methanol and IPA for 5 minutes each, then dry with N_2.	
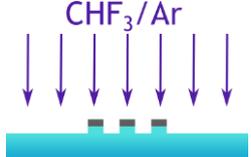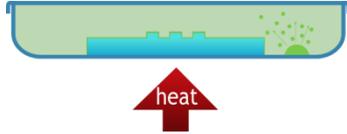
2.3	Apply SU-8	Expose sample to O_2 plasma for 1 minute at 200 W to improve adhesion. Pour blob (~5 mm diameter) of SU-8 3050 directly from bottle onto sample.	
2.4	 Softbake	Place sample on hotplate at 105°C for 2-3 hours to allow for solvent evaporation.	
2.5	NIL – stamp placement	Place sample in frame to constrain lateral movement. Place frame on hotplate at 105°C and leave for 4 minutes. Slowly lower quartz stamp face down onto sample as carefully as possible. Start at one edge and apply at an angle to minimise the formation of air bubbles and give any that do form a route to escape.	NIL steps (2.5-2.7) are specific to equipment in this project, but the general process can be performed with other equipment. Inlays may also be patterned by other processes such as photolithography.
2.6	NIL – exposure	Place pocket imprinter version 3.1 onto back of stamp and leave for 4 minutes. Turn on UV LED. Switch off after 3 minutes.	Longer exposures may be required for different UV light sources or less transparent stamps.
2.7	NIL – stamp separation	Remove pocket imprinter device and carefully separate stamp from substrate with razor blade on hotplate at 105°C.	Separation performed at imprint temperature to minimise stress caused by differential thermal expansion of the two materials.
2.8	Develop edges	Immerse newly patterned inlay in EC solvent for 5 minutes to remove unexposed SU-8 from the edges.	
2.9	Oven bake	Bake in oven at 180°C for 1-3 hours to fully cure SU-8.	
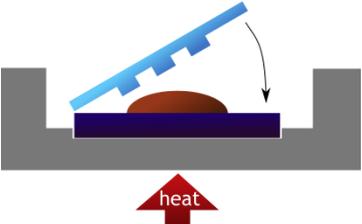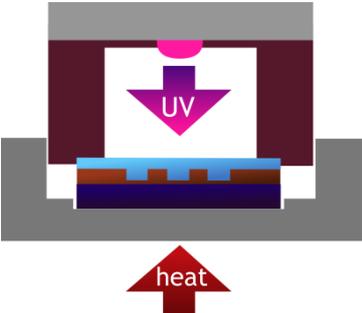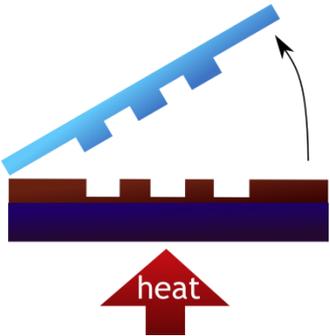
2.10	Non-adhesive coating (optional) 	Deposit 10 nm SiO_2 by PECVD. Apply TPFS coating as described in step 1.12.	Si_3N_4 may be used instead of SiO_2 or TPFS may be applied directly to SU-8. Alternative deposition methods to PECVD may also be considered.
	End of process 	Inlay patterning complete.	
3.0	**Injection moulding**		
3.1	Polymer preparation	Dry PC beads in vacuum oven at 110°C for 2 hours.	
3.2	Machine preparation 	Turn on injection moulding machine and cooling unit. Set melt (nozzle) temperature to 250°C with the other barrel heating rings set at 10°C intervals from hopper to nozzle. Allow 30-60 minutes for the hydraulics and barrel to warm up.	To save time it may also be prudent to heat up the tool at this time (80°C).
3.3	Prime barrel	Pour 750 g of un-dried PC into hopper and plasticise through the barrel.	
3.4	Set moulding conditions 	$T_m = 280°C$ $T_w = 80°C$ $v_i = 50$ cm^3s^{-1} $P_{hold} = 1000$ bar $t_c = 15$ s	Consult manufacturer's guidelines for processing conditions for other polymers.
3.5	Insert inlay 	Insert inlay into frame and activate mould height determination in software.	
3.6	Prepare process polymer	Pour dried PC into hopper and plasticise until melt runs clear.	
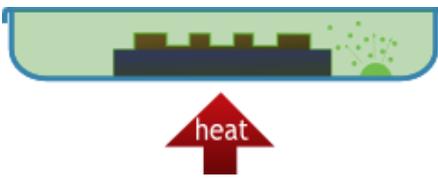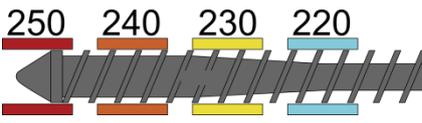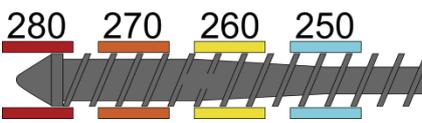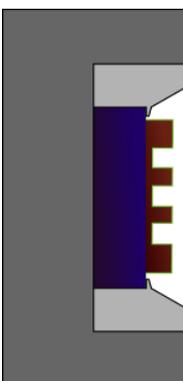
		Halt plasticising and wipe nozzle.	
3.7	Run manual cycle	Close mould under pressure. Advance injection unit until pressure build-up is achieved. Activate automatic plasticising which will stop when the mould is filled. Open mould and eject part.	
3.8	Semi-automatic verification	Run several cycles in semi-automatic mode, adjusting parameters until happy with part quality.	
3.9	Automatic production	Set required number of parts and run automatically until this number is reached.	
3.10	Shutdown procedure	Retract injection unit and purge remaining material from barrel. Purge barrel by plasticising with PP while cooling from 260ºC to 240ºC. Remove inlay and close tool without pressure. Turn off injection moulding machine and cooling unit.	
3.11	Package and remove sprues	Manually break sprues from moulded parts and package as desired.	
	End of process.	Injection moulding complete.	
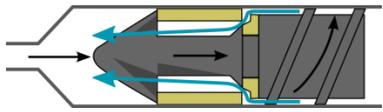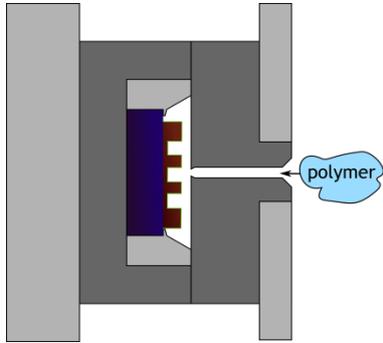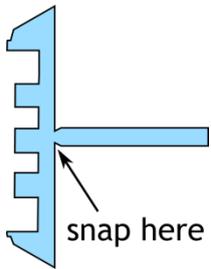
Glossary of abbreviations

Equipment/process

AFM	atomic force microscope
CAH	contact angle hysteresis
CD	compact disk
CVD	chemical vapour deposition
EBL	electron beam lithography
FFT	fast Fourier transform
HAR	high aspect ratio
ICP	induction coupled plasma
JWNC	James Watt Nanofabrication Centre
LIGA	lithographie, galvanik und abformung (lithography, electroplating and moulding)
NIL	nanoimprint lithography
PEB	post exposure bake
PECVD	plasma enhanced chemical vapour deposition
R2R	roll to roll (embossing)
RIE	reactive ion etching
SEM	scanning electron microscope
SF-NIL	step and flash nanoimprint lithography
SPM	scanning probe microscope
SR-NIL	step and repeat nanoimprint lithography
T-NIL	thermal nanoimprint lithography
TUV-NIL	thermal ultra-violet nanoimprint lithography
UV	ultra-violet

UV-NIL	ultra-violet nanoimprint lithography
WCA	water contact angle
XPS	x-ray photon spectroscopy

Materials

COC	cyclic olefin copolymer
IPA	isopropyl alcohol
MIBK	methyl isobutyl ketone
PC	poly(carbonate)
PDMS	poly(dimethyl siloxane)
PET	poly(ethylene terephthalate)
PI	poly(imide)
PMMA	poly(methyl methacrylate)
PP	poly(propylene)
PS	poly(styrene)
PUA	poly(urethane acrylate)
RO	reverse osmosis
TMAH	tetramethylammonium hydroxide
TPE	thermoplastic elastomer
TPFS	Trichloro(1H,1H,2H,2H-perfluorooctyl)silane
TPU	thermoplastic poly(urethane)

Parameters

P_{hold}	holding pressure

t_c cooling time

T_m melt temperature (process) or melting temperature (material)

T_w tool (mould) temperature

v_i injection speed

References

1.	Schuelke, T. and T. A. Grotjohn, *Diamond polishing.* Diamond and Related Materials, 2013. **32**: p. 17.

2.	Brunner, R., O. Sandfuchs, C. Pacholski, C. Morhard, and J. Spatz, *Lessons from nature: biomimetic subwavelength structures for high-performance optics.* Laser & Photonics Reviews, 2012. **6**(5): p. 641.

3.	Geim, A. K., S. V. Dubonos, I. V. Grigorieva, K. S. Novoselov, A. A. Zhukov, and S. Y. Shapoval, *Microfabricated adhesive mimicking gecko foot-hair.* Nat Mater, 2003. **2**(7): p. 461.

4.	Engler, A. J., P. O. Humbert, B. Wehrle-Haller, and V. M. Weaver, *Multiscale Modeling of Form and Function.* Science, 2009. **324**(5924): p. 208.

5.	Luong-Van, E., I. Rodriguez, H. Y. Low, N. Elmouelhi, B. Lowenhaupt, S. Natarajan, C. T. Lim, R. Prajapati, M. Vyakarnam, and K. Cooper, *Review: Micro- and nanostructured surface engineering for biomedical applications.* Journal of Materials Research, 2013. **28**(2): p. 165.

6.	Kawata, S., *Plasmonics: Future Outlook.* Japanese Journal of Applied Physics, 2013. **52**(1).

7.	Weickert, J., R. B. Dunbar, H. C. Hesse, W. Wiedemann, and L. Schmidt-Mende, *Nanostructured Organic and Hybrid Solar Cells.* Advanced Materials, 2011: p. n/a.

8.	Yamada, N., T. Ijiro, E. Okamoto, K. Hayashi, and H. Masuda, *Characterization of antireflection moth-eye film on crystalline silicon photovoltaic module.* Opt. Express, 2011. **19**(S2): p. A118.

9.	Lee, S. G., D. Y. Lee, H. S. Lim, D. H. Lee, S. Lee, and K. Cho, *Switchable Transparency and Wetting of Elastomeric Smart Windows.* Advanced Materials, 2010. **22**(44): p. 5013.

10.	Oh, S. S., C.-G. Choi, and Y.-S. Kim, *Fabrication of micro-lens arrays with moth-eye antireflective nanostructures using thermal imprinting process.* Microelectronic Engineering, 2010. **87**(11): p. 2328.

11.	Päivänranta, B., T. Saastamoinen, and M. Kuittinen, *A wide-angle antireflection surface for the visible spectrum.* Nanotechnology, 2009. **20**(37): p. 375301.

12.	Bernhard, C. G., *Structural and Functional Adaptation in a Visual System.* Endeavour, 1967. **26**(98): p. 79.

13.	Nishimoto, S. and B. Bhushan, *Bioinspired self-cleaning surfaces with superhydrophobicity, superoleophobicity, and superhydrophilicity.* Rsc Advances, 2013. **3**(3): p. 671.

14.	Wang, J. D., H. S. Chen, T. Sui, A. Li, and D. R. Chen, *Investigation on hydrophobicity of lotus leaf: Experiment and theory.* Plant Science, 2009. **176**(5): p. 687.

15.	Yan, Y. Y., N. Gao, and W. Barthlott, *Mimicking natural superhydrophobic surfaces and grasping the wetting process: a review on recent progress in preparing superhydrophobic surfaces.* Advances in colloid and interface science, 2011. **169**(2): p. 80.

16.	Milne, A. J. B. and A. Amirfazli, *The Cassie equation: how it is meant to be used.* Advances in colloid and interface science, 2012. **170**(1-2): p. 48.

17.	Sullivan, T. and F. Regan, *The characterization, replication and testing of dermal denticles of Scyliorhinus canicula for physical mechanisms of biofouling prevention.* Bioinspiration & Biomimetics, 2011. **6**(4): p. 11pp.

18.	Liu, Y. H. and G. J. Li, *A new method for producing "Lotus Effect" on a biomimetic shark skin.* Journal of Colloid and Interface Science, 2012. **388**: p. 235.

19.	Kwak, M. K., H. E. Jeong, T. I. Kim, H. Yoon, and K. Y. Suh, *Bio-inspired slanted polymer nanohairs for anisotropic wetting and directional dry adhesion.* Soft Matter, 2010. **6**(9): p. 1849.

20.	Jeong, H. E. and K. Y. Suh, *Nanohairs and nanotubes: Efficient structural elements for gecko-inspired artificial dry adhesives.* Nano Today, 2009. **4**(4): p. 335.

21.	Curtis, A. S. G. and M. Varde, *Control of Cell Behaviour - Topological Factors.* Journal of the National Cancer Institute, 1964. **33**(1): p. 15.

22.	Weiss, P., *Cell Contact*, G.H. Bourne and J.F. Danielli, Editors. 1958, Academic Press. p. 391.

23.	Guilak, F., D. M. Cohen, B. T. Estes, J. M. Gimble, W. Liedtke, and C. S. Chen, *Control of stem cell fate by physical interactions with the extracellular matrix.* Cell Stem Cell, 2009. **5**(1): p. 17.

24.   Ferreira, L., J. M. Karp, L. Nobre, and R. Langer, *New opportunities: The use of Nanotechnologies to manipulate and track stem cells.* Cell Stem Cell, 2008. **3**(2): p. 136.

25.   Borenstein, J. T., C. J. Bettinger, and Ieee, *Engineered Nanotopographic Structures for Applications in Tissue Engineering and Regenerative Medicine*. 2009. 21.

26.   Califano, J. and C. Reinhart-King, *Substrate Stiffness and Cell Area Predict Cellular Traction Stresses in Single Cells and Cells in Contact.* Cellular and Molecular Bioengineering, 2010. **3**(1): p. 68.

27.   Engler, A. J., S. Sen, H. L. Sweeney, and D. E. Discher, *Matrix elasticity directs stem cell lineage specification.* Cell, 2006. **126**(4): p. 677.

28.   Holle, A. W. and A. J. Engler, *Cell rheology: Stressed-out stem cells.* Nat Mater, 2010. **9**(1): p. 4.

29.   Chowdhury, F., S. Na, D. Li, Y.-C. Poh, T. S. Tanaka, F. Wang, and N. Wang, *Material properties of the cell dictate stress-induced spreading and differentiation in embryonic stem cells.* Nature materials, 2010. **9**(1): p. 82.

30.   Mata, A., C. Boehm, A. J. Fleischman, G. Muschler, and S. Roy, *Analysis of connective tissue progenitor cell behavior on polydimethylsiloxane smooth and channel micro-textures.* Biomedical Microdevices, 2002. **4**(4): p. 267.

31.   Markert, L. D. A., J. Lovmand, M. Foss, R. H. Lauridsen, M. Lovmand, E.-M. Füchtbauer, A. Füchtbauer, K. Wertz, F. Besenbacher, F. S. Pedersen, and M. Duch, *Identification of distinct topographical surface microstructures favoring either undifferentiated expansion or differentiation of murine embryonic stem cells.* Stem cells and development, 2009. **18**(9): p. 1331.

32.   Kantawong, F., K. E. V. Burgess, K. Jayawardena, A. Hart, R. J. Burchmore, N. Gadegaard, R. O. C. Oreffo, and M. J. Dalby, *Whole proteome analysis of osteoprogenitor differentiation induced by disordered nanotopography and mediated by ERK signalling.* Biomaterials, 2009. **30**(27): p. 4723.

33.   Dalby, M. J., M. O. Riehle, D. S. Sutherland, H. Agheli, and A. S. G. Curtis, *Use of nanotopography to study mechanotransduction in fibroblasts - methods and perspectives.* European Journal of Cell Biology, 2004. **83**(4): p. 159.

34.   Martinez, E., E. Engel, J. A. Planell, and J. Samitier, *Effects of artificial micro- and nano-structured surfaces on cell behaviour.* Annals of Anatomy-Anatomischer Anzeiger, 2009. **191**(1): p. 126.

35.   Kulangara, K. and K. W. Leong, *Substrate topography shapes cell function.* Soft Matter, 2009. **5**(21): p. 4072.

36.   Dalby, M. J., N. Gadegaard, R. Tare, A. Andar, M. O. Riehle, P. Herzyk, C. D. W. Wilkinson, and R. O. C. Oreffo, *The control of human mesenchymal cell differentiation using nanoscale symmetry and disorder.* Nature materials, 2007. **6**(12): p. 997.

37.   Gadegaard, N., K. Seunarine, D. J. A. Smith, D. O. Meredith, C. D. W. Wilkinson, and M. O. Riehle, *A hybrid three-dimensional nanofabrication method for producing vascular tissue engineering scaffold.* Japanese Journal of Applied Physics, 2008. **47**(9, Part 1): p. 7415.

38.   Dawson, E., G. Mapili, K. Erickson, S. Taqvi, and K. Roy, *Biomaterials for stem cell differentiation.* Advanced Drug Delivery Reviews, 2008. **60**(2): p. 215.

39.   Bettinger, C. J., *Synthesis and microfabrication of biomaterials for soft-tissue engineering.* Pure and Applied Chemistry, 2009. **81**(12): p. 2183.

40.   Meng, D., M. Erol, and A. R. Boccaccini, *Processing Technologies for 3D Nanostructured Tissue Engineering Scaffolds.* Advanced Engineering Materials, 2010. **12**(9): p. B467.

41.   Kubo, K., N. Tsukimura, F. Iwasa, T. Ueno, L. Saruwatari, H. Aita, W. A. Chiou, and T. Ogawa, *Cellular behavior on TiO2 nanonodular structures in a micro-to-nanoscale hierarchy model.* Biomaterials, 2009. **30**(29): p. 5319.

42.   Mata, A., C. Boehm, A. J. Fleischman, G. Muschler, and S. Roy, *Growth of connective tissue progenitor cells on microtextured polydimethylsiloxane surfaces.* Journal of Biomedical Materials Research, 2002. **62**(4): p. 499.

43.   Ferreira, L. S., S. Gerecht, J. Fuller, H. F. Shieh, G. Vunjak-Novakovic, and R. Langer, *Bioactive hydrogel scaffolds for controllable vascular differentiation of human embryonic stem cells.* Biomaterials, 2007. **28**(17): p. 2706.

44.   Gittens, R. A., R. Olivares-Navarrete, A. Cheng, D. M. Anderson, T. McLachlan, I. Stephan, J. Geis-Gerstorfer, K. H. Sandhage, A. G. Fedorov, F. Rupp, B. D. Boyan, R. Tannenbaum, and Z. Schwartz, *The roles of titanium surface micro/nanotopography and*

wettability on the differential response of human osteoblast lineage cells. Acta Biomaterialia, 2013. **9**(4): p. 6268.

45.   Luthen, F., R. Lange, P. Becker, J. Rychly, U. Beck, and J. G. B. Nebe, *The influence of surface roughness of titanium on beta 1-and beta 3-integrin adhesion and the organization of fibronectin in human osteoblastic cells.* Biomaterials, 2005. **26**(15): p. 2423.

46.   Shadpour, H. and N. L. Allbritton, *In situ Roughening of Polymeric Microstructures.* ACS Applied Materials & Interfaces, 2010.

47.   Acikgoz, C., M. A. Hempenius, J. Huskens, and G. J. Vancso, *Polymers in conventional and alternative lithography for the fabrication of nanostructures.* European Polymer Journal, 2011. **47**(11): p. 2033.

48.   Dalby, M. J., M. O. Riehle, D. S. Sutherland, H. Agheli, and A. S. G. Curtis, *Changes in fibroblast morphology in response to nano-columns produced by colloidal lithography.* Biomaterials, 2004. **25**(23): p. 5415.

49.   Li, Y., J. Zhang, S. Zhu, H. Dong, Z. Wang, Z. Sun, J. Guo, and B. Yang, *Bioinspired silicon hollow-tip arrays for high performance broadband anti-reflective and water-repellent coatings.* J. Mater. Chem., 2009. **19**(13): p. 1806.

50.   Lee, J.-S., *Progress in non-volatile memory devices based on nanostructured materials and nanofabrication.* Journal of Materials Chemistry, 2011. **21**(37): p. 14097.

51.   Schift, H., *Nanoimprint lithography: An old story in modern times? A review.* Journal of Vacuum Science & Technology B, 2008. **26**(2): p. 458.

52.   Guo, L. J., *Nanoimprint Lithography: Methods and Material Requirements.* Advanced Materials, 2007. **19**(4): p. 495.

53.   Chou, S. Y., P. R. Krauss, and P. J. Renstrom, *Imprint of Sub-25 nm Vias and Trenches in Polymers.* Applied Physics Letters, 1995. **67**(21): p. 3114.

54.   Hua, F., Y. Sun, A. Gaur, M. A. Meitl, L. Bilhaut, L. Rotkina, J. Wang, P. Geil, M. Shim, J. A. Rogers, and A. Shim, *Polymer Imprint Lithography with Molecular-Scale Resolution.* Nano Letters, 2004. **4**(12): p. 2467.

55.   Heilig, M., S. Giselbrecht, A. Guber, and M. Worgull, *Microthermoforming of nanostructured polymer films: a new bonding method for the integration of nanostructures in 3-dimensional cavities.* Microsystem Technologies-Micro-and Nanosystems-Information Storage and Processing Systems, 2010. **16**(7): p. 1221.

56.   Heilig, M., M. Schneider, H. Dinglreiter, and M. Worgull, *Technology of microthermoforming of complex three-dimensional parts with multiscale features.* Microsystem Technologies-Micro-and Nanosystems-Information Storage and Processing Systems, 2011. **17**(4): p. 593.

57.   Zaouk, R., B. Y. Park, and M. J. Madou, *Fabrication of polydimethylsiloxane microfluidics using SU-8 molds.* Methods Mol Biol, 2006. **321**: p. 17.

58.   Lee, L. H., R. Peerani, M. Ungrin, C. Joshi, E. Kumacheva, and P. W. Zandstra, *Micropatterning of human embryonic stem cells dissects the mesoderm and endoderm lineages.* Stem cell research, 2009. **2**(2): p. 155.

59.   Tee, S.-Y., J. Fu, C. S. Chen, and P. A. Janmey, *Cell Shape and Substrate Rigidity Both Regulate Cell Stiffness.* Biophysical Journal, 2011. **100**(5).

60.   Gadegaard, N., S. Thoms, D. S. Macintyre, K. McGhee, J. Gallagher, B. Casey, and C. D. W. Wilkinson, *Arrays of nano-dots for cellular engineering.* Microelectronic Engineering, 2003. **67-68**: p. 162.

61.   Ahn, S. H. and L. J. Guo, *Large-Area Roll-to-Roll and Roll-to-Plate Nanoimprint Lithography: A Step toward High-Throughput Application of Continuous Nanoimprinting.* ACS Nano, 2009. **3**(8): p. 2304.

62.   Vig, A. L., T. Makela, P. Majander, V. Lambertini, J. Ahopelto, and A. Kristensen, *Roll-to-roll fabricated lab-on-a-chip devices.* Journal of Micromechanics and Microengineering, 2011. **21**(3).

63.   Moonen, P. F., I. Yakimets, and J. Huskens, *Fabrication of Transistors on Flexible Substrates: from Mass-Printing to High-Resolution Alternative Lithography Strategies.* Advanced Materials, 2012. **24**(41): p. 5526.

64.   Kumar, P. and S. Chand, *Recent progress and future aspects of organic solar cells.* Progress in Photovoltaics: Research and Applications, 2012. **20**(4): p. 377.

65.   Ruchhoeft, P., M. Colburn, B. Choi, H. Nounu, S. Johnson, T. Bailey, S. Damle, M. Stewart, J. Ekerdt, S. V. Sreenivasan, J. C. Wolfe, and C. G. Willson. *Patterning curved surfaces:*

Template generation by ion beam proximity lithography and relief transfer by step and flash imprint lithography. 1999. Marco Island, Florida (USA): AVS.

66.   Moonen, P. F., B. Vratzov, W. T. T. Smaal, B. K. C. Kjellander, G. H. Gelinck, E. R. Meinders, and J. Huskens, *Flexible thin-film transistors using multistep UV nanoimprint lithography*. Organic Electronics, 2012. **13**(12): p. 3004.

67.   Pranov, H., H. K. Rasmussen, N. B. Larsen, and N. Gadegaard, *On the injection molding of nanostructured polymer surfaces*. Polymer Engineering & Science, 2006. **46**(2): p. 160.

68.   Macintyre, D. and S. Thoms, *The fabrication of high resolution features by mould injection*. Microelectronic Engineering, 1998. **42**: p. 211.

69.   Schift, H., C. David, M. Gabriel, J. Gobrecht, L. J. Heyderman, W. Kaiser, S. Köppel, and L. Scandella, *Nanoreplication in polymers using hot embossing and injection molding*. Microelectronic Engineering, 2000. **53**(1-4): p. 171.

70.   Gadegaard, N., S. Mosler, and N. B. Larsen, *Biomimetic Polymer Nanostructures by Injection Molding*. Macromolecular Materials and Engineering, 2003. **288**(1): p. 76.

71.   Giboz, J., T. Copponnex, and P. Mélé, *Microinjection molding of thermoplastic polymers: a review*. Journal of Micromechanics and Microengineering, 2007. **17**(6): p. R96.

72.   Yoon, S.-h., C. Srirojpinyo, J. S. Lee, J. L. Mead, S. Matsui, and C. M. F. Barry. *Evaluation of novel tooling for nanoscale injection molding*. in *Proc. SPIE*. 2005.

73.   Zhao, J., R. Ong, G. Chen, Y. K. Juay, F. L. Ng, M. W. Lee, and C. H. Kua. *Development of Rapid Manufacturing Technology of Polymer Microfluidic Devices by Micro Moulding Using Silicon Mould Inserts*. in *Proceedings of the 6th International Conference on Nanochannels, Microchannels, and Minichannels, Pts a and B*. 2008. New York: Amer Soc Mechanical Engineers.

74.   Viana, J., *Development of the skin layer in injection moulding: phenomenological model*. Polymer, 2004. **45**(3): p. 993.

75.   Yao, D. and B. Kim, *Development of rapid heating and cooling systems for injection molding applications*. Polymer Engineering & Science, 2002. **42**(12): p. 2471.

76.   Chang, P.-C. and S.-J. Hwang, *Experimental investigation of infrared rapid surface heating for injection molding*. Journal of Applied Polymer Science, 2006. **102**(4): p. 3704.

77.   Kim, Y., Y. Choi, and S. Kang, *Replication of high density optical disc using injection mold with MEMS heater*. Microsystem Technologies, 2005. **11**(7): p. 464.

78.   Michaeli, W. and F. Klaiber, *Development of a system for laser-assisted molding of micro- and nanostructures*. Journal of Vacuum Science & Technology B, 2009. **27**(3): p. 1323.

79.   Bekesi, J., J. J. J. Kaakkunen, W. Michaeli, F. Klaiber, M. Schoengart, J. Ihlemann, and P. Simon, *Fast fabrication of super-hydrophobic surfaces on polypropylene by replication of short-pulse laser structured molds*. Applied Physics a-Materials Science & Processing, 2010. **99**(4): p. 691.

80.   Keun, P. and L. Sang-Ik, *Localized mold heating with the aid of selective induction for injection molding of high aspect ratio micro-features*. Journal of Micromechanics and Microengineering, 2010. **20**(3): p. 035002.

81.   Kim, S., C.-S. Shiau, B. H. Kim, and D. Yao, *Injection Molding Nanoscale Features with the Aid of Induction Heating*. Polymer-Plastics Technology and Engineering, 2007. **46**(11): p. 1031.

82.   Yoo, Y. E., T. H. Kim, D. S. Choi, S. M. Hyun, H. J. Lee, K. H. Lee, S. K. Kim, B. H. Kim, Y. H. Seo, H. G. Lee, and J. S. Lee, *Injection molding of a nanostructured plate and measurement of its surface properties*. Current Applied Physics, 2009. **9**(2, Supplement 1): p. e12.

83.   Wang, G., G. Zhao, H. Li, and Y. Guan, *Research on a New Variotherm Injection Molding Technology and its Application on the Molding of a Large LCD Panel*. Polymer-Plastics Technology and Engineering, 2009. **48**(7): p. 671.

84.   Liu, J., G. Zhao, G. Wang, and Y. Guan, *Fully Coupled Transient Heat Transfer and Melt Filling Simulations in Rapid Heat Cycle Molding with Steam Heating*. Polymer-Plastics Technology and Engineering, 2011. **50**(4): p. 423.

85.   Lin, H. Y., C. H. Chang, and W. B. Young, *Experimental Study on the Filling of Nano Structures with Infrared Mold Surface Heating*. International Polymer Processing, 2011. **26**(1): p. 73.

86.   Yoon, S.-H., P. Palanisamy, P. Padmanabha, J. L. Mead, and C. M. F. Barry, *Comparison of Tooling Materials in Injection Molding of Microscale Features*. ASME Conference Proceedings, 2009. **2009**(43857): p. 545.

87.   Kim, Y., S.-H. Yoon, J. S. Lee, S. Johnston, J. L. Mead, and C. M. F. Barry. *Performance of Hybrid Tooling in Micro Injection Molding*. in *Proc. Ann. Tech. Conf. Soc. Plast. Eng.* 2010.

88.   Yoon, S.-h., J. Lee, K. Park, J. L. Mead, S. Matsui, and C. M. F. Barry. *Critical factors for nanoscale injection molding*. 2006: SPIE.

89.   Yoon, S.-H., P. Padmanabha, J. S. Lee, J. L. Mead, C. M. F. Barry, N.-G. Cha, A. A. Busnaina, and K. Park. *Evaluation of Metal-Polymer Hybrid Tooling for Micro-Injection Moulding*. in *Proc. Ann. Tech. Conf. Soc. Plast. Eng.* 2008. Milwaukee, WI.

90.   Yoon, S.-H., C. M. F. Barry, J. L. Mead, N.-G. Cha, and A. A. Busnaina, *Methods for Forming Metal-Polymer Hybrid Tooling for Forming Parts Having Micro Features*. 2011, University of Massachusetts Lowel, Northeastern University: USA.

91.   Hansen, T. S., D. Selmeczi, and N. B. Larsen, *Fast prototyping of injection molded polymer microfluidic chips*. Journal of Micromechanics and Microengineering, 2010. **20**(1): p. 8.

92.   Park, S. H., W. I. Lee, S. N. Moon, Y. E. Yoo, and Y. H. Cho, *Injection molding micro patterns with high aspect ratio using a polymeric flexible stamper*. Express Polymer Letters, 2011. **5**(11): p. 950.

93.   Kim, S. H., J. H. Jeong, and J. R. Youn, *Nanopattern insert molding*. Nanotechnology, 2010. **21**(20): p. 205302.

94.   Zhang, N., C. J. Byrne, D. J. Browne, and M. D. Gilchrist, *Towards nano-injection molding*. Materials Today, 2012. **15**(5): p. 216.

95.   Park, S., H. Schift, C. Padeste, B. Schnyder, R. Kotz, and J. Gobrecht, *Anti-adhesive layers on nickel stamps for nanoimprint lithography*. Microelectronic Engineering, 2004. **73-4**: p. 196.

96.   Schift, H., S. Saxer, S. Park, C. Padeste, U. Pieles, and J. Gobrecht, *Controlled co-evaporation of silanes for nanoimprint stamps*. Nanotechnology, 2005. **16**(5): p. S171.

97.   Schulz, H., F. Osenberg, J. Engemann, and H. C. Scheer, *Mask fabrication by nanoimprint lithography using anti-sticking layers*, in *16th European Conference on Mask Technology for Integrated Circuits and Microcomponents*, U.F.W. Behringer, Editor. 2000, Spie-Int Soc Optical Engineering: Bellingham. p. 244.

98.   Guo, Y. H., G. Liu, X. L. Zhu, and Y. C. Tian, *Analysis of the demolding forces during hot embossing*. Microsystem Technologies-Micro-and Nanosystems-Information Storage and Processing Systems, 2007. **13**(5-6): p. 411.

99.   Matschuk, M., H. Bruus, and N. B. Larsen, *Nanostructures for all-polymer microfluidic systems*. Microelectronic Engineering, 2010. **87**(5-8): p. 1379.

100.   Beck, M., M. Graczyk, I. Maximov, E. L. Sarwe, T. G. I. Ling, M. Keil, and L. Montelius, *Improving stamps for 10 nm level wafer scale nanoimprint lithography*. Microelectronic Engineering, 2002. **61-2**: p. 441.

101.   Park, S., C. Padeste, H. Schift, and J. Gobrecht, *Nanostructuring of anti-adhesive layers by hot embossing lithography*. Microelectronic Engineering, 2003. **67–68**(0): p. 252.

102.   Wu, C. C., S. L. C. Hsu, and I. L. Lo, *Fabrication and Application of Polyimide Plastic Molds for Nanoimprint Lithography*. Journal of Nanoscience and Nanotechnology, 2010. **10**(10): p. 6446.

103.   Park, S., H. Schift, C. Padeste, B. Schnyder, and J. Gobrecht, *Improved anti-adhesive coating for nanoimprint lithography by co-evaporation of fluorinated mono- and trichlorosilanes*. Nontraditional Approaches to Patterning, ed. S.X.y.L.J.L.C.D.E. Yang. 2004. 37.

104.   Moresco, J., C. H. Clausen, and W. Svendsen, *Improved anti-stiction coating of SU-8 molds*. Sensors and Actuators B-Chemical, 2010. **145**(2): p. 698.

105.   Kim, H. H., S. G. Park, E. H. Lee, S. G. Lee, and B. H. O, *Durability of nitrided fluorocarbon polymer films for nanoimprint lithography*. Thin Solid Films, 2011. **519**(16): p. 5490.

106.   Kumar, G., H. X. Tang, and J. Schroers, *Nanomoulding with amorphous metals*. Nature, 2009. **457**(7231): p. 868.

107.   Yoon, S.-H., N.-G. Cha, J. S. Lee, J.-G. Park, D. J. Carter, J. L. Mead, and C. M. F. Barry, *Effect of processing parameters, antistiction coatings, and polymer type when injection molding microfeatures*. Polymer Engineering & Science, 2010. **50**(2): p. 411.

108.   Matschuk, M. and N. B. Larsen, *Injection molding of high aspect ratio sub-100 nm nanostructures*. Journal of Micromechanics and Microengineering, 2013. **23**(2): p. 025003.

109.   Miikkulainen, V., M. Suvanto, T. A. Pakkanen, S. Siitonen, P. Karvinen, M. Kuittinen, and H. Kisonen, *Thin films of MoN, WN, and perfluorinated silane deposited from dimethylamido precursors as contamination resistant coatings on micro-injection mold inserts*. Surface and Coatings Technology, 2008. **202**(21): p. 5103.

110. Cunha, L., M. Andritschky, K. Pischow, Z. Wang, A. Zarychta, A. S. Miranda, and A. M. Cunha, *Performance of chromium nitride and titanium nitride coatings during plastic injection moulding.* Surface and Coatings Technology, 2002. **153**(2–3): p. 160.

111. Houle, F. A., S. Raoux, D. C. Miller, C. Jahnes, and S. Rossnagel, *Metal-containing release layers for use with UV-cure nanoimprint lithographic template materials.* Journal of Vacuum Science & Technology B, 2008. **26**(4): p. 1301.

112. Khokhar, A. Z., A. Gaston, I. Obieta, and N. Gadegaard, *Compact LED based nanoimprinter for UV-NIL.* Microelectronic Engineering, 2011. **88**(11): p. 3347.

113. Zhang, W., M. Wahlgren, and B. Sivik, *Membrane Characterization by the Contact Angle Technique: II. Characterization of UF-Membranes and Comparison between the Captive Bubble and Sessile Drop as Methods to obtain Water Contact Angles.* Desalination, 1989. **72**(3): p. 263.

114. Gadegaard, N., E. Martines, M. O. Riehle, K. Seunarine, and C. D. W. Wilkinson, *Applications of nano-patterning to tissue engineering.* Microelectronic Engineering, 2006. **83**(4-9): p. 1577.

115. Labianca, N. and J. D. Gelorme, *High aspect ratio resist for thick film applications.* Advances in Resist Technology and Processing Xii, ed. R.D. Allen. Vol. 2438. 1995, Bellingham: Spie - Int Soc Optical Engineering. 846.

116. *SU-8: Thick Photo-Resist for MEMS.* Editor: F. Chollet, 2 March 2013 http://memscyclopedia.org/su8.html, accessed: 23 June 2013.

117. Stormonth-Darling, J. M. and N. Gadegaard, *Injection Moulding Difficult Nanopatterns with Hybrid Polymer Inlays.* Macromolecular Materials and Engineering, 2012. **297**(11): p. 1075.

118. Hu, W., A. S. Crouch, D. Miller, M. Aryal, and K. J. Luebke, *Inhibited cell spreading on polystyrene nanopillars fabricated by nanoimprinting and in situ elongation.* Nanotechnology, 2010. **21**(38): p. 385301.

119. Michaeli, W., C. Hopmann, and M. Schoengart. *One-step Production of Superhydrophobic Surfaces Using Laser-based Variothermal Injection Moulding.* in *European Society for Precision Engineering and Nanotechnology International Conference.* 2011. Como.

120. Jeong, H. E., S. H. Lee, P. Kim, and K. Y. Suh, *Stretched Polymer Nanohairs by Nanodrawing.* Nano Letters, 2006. **6**(7): p. 1508.

121. Pranov, H., *Processes for Nanostructuring of Plastic Parts for Biological and Optical Applications.* 2006, Technical University of Denmark: Kgs. Lyngby, Denmark.

122. Seunarine, K., A. S. G. Curtis, D. O. Meredith, C. D. W. Wilkinson, M. O. Riehle, and N. Gadegaard, *A Hierarchical Response of Cells to Perpendicular Micro- and Nanometric Textural Cues.* Ieee Transactions on Nanobioscience, 2009. **8**(3): p. 219.

123. Chen, Y. and A. Pepin, *Nanofabrication: Conventional and nonconventional methods.* Electrophoresis, 2001. **22**(2): p. 187.

124. Campo, A. d. and C. Greiner, *SU-8: a photoresist for high-aspect-ratio and 3D submicron lithography.* Journal of Micromechanics and Microengineering, 2007. **17**(6): p. R81.

125. Padeste, C., H. Özçelik, J. Ziegler, A. Schleunitz, M. Bednarzik, D. Yücel, and V. Hasırcı, *Replication of high aspect ratio pillar array structures in biocompatible polymers for tissue engineering applications.* Microelectronic Engineering, 2011. **88**(8): p. 1836.

126. Ghassemi, S., N. Biais, K. Maniura, S. J. Wind, M. P. Sheetz, and J. Hone, *Fabrication of elastomer Pillar Arrays with Modulated Stiffness for Cellular Force Measurements.* Journal of vacuum science & technology. B, Microelectronics and nanometer structures : processing, measurement, and phenomena : an official journal of the American Vacuum Society, 2008. **26**(6): p. 2549.

127. Fu, J., Y.-k. Wang, M. T. Yang, R. A. Desai, X. Yu, Z. Liu, and C. S. Chen, *Mechanical regulation of cell function with geometrically modulated elastomeric substrates.* Nature Methods, 2010. **7**(9): p. 733.

128. *Circularity.* [cited 2013 17 April]; Available from: http://rsbweb.nih.gov/ij/plugins/circularity.html.

129. Reynolds, P. M., R. H. Pedersen, J. Stormonth-Darling, M. J. Dalby, M. O. Riehle, and N. Gadegaard, *Label-Free Segmentation of Co-cultured Cells on a Nanotopographical Gradient.* Nano Letters, 2012. **13**(2): p. 570.

130. Izadi, H., B. Zhao, Y. Han, N. McManus, and A. Penlidis, *Teflon hierarchical nanopillars with dry and wet adhesive properties.* Journal of Polymer Science Part B: Polymer Physics, 2012. **50**(12): p. 846.

131.   Fisher, O. Z., A. Khademhosseini, R. Langer, and N. A. Peppas, *Bioinspired Materials for Controlling Stem Cell Fate.* Accounts of Chemical Research, 2010. **43**(3): p. 419.

132.   Gent, A. N., *On the relation between indentation hardness and Young's modulus.* Institution of the Rubber Industry - Transactions and Proceedings, 1957. **34**: p. 46.

133.   Engel, Y., J. D. Schiffman, J. M. Goddard, and V. M. Rotello, *Nanomanufacturing of biomaterials.* Materials Today, 2012. **15**(11): p. 478.